



Full Scale Servo-Actuated Morphing Aileron for Wind Tunnel Tests

A thesis submitted to
The PhD school of Aerospace, Naval and Quality Engineering
of
Università degli Studi di Napoli Federico II

by
Gianluca Amendola

*In partial fulfilment of the requirements
for
the degree of Doctor of Philosophy
in
Aerospace Engineering*

Tutor: Chiar.mo Prof. Leonardo Lecce

Supervisors: Ph.D Ignazio Dimino, Prof. Rosario Pecora, Prof. Francesco Amoroso

“Mi raccomando, stia lontano dall’aerospazio”

Cit.

Contents

ABSTRACT	10
1. MORPHING STRUCTURES STATE OF ART	13
1.1 The intelligent wing	13
1.2 Actuation system for morphing application	25
2. CRIAQ PROJECT AND THE ADAPTIVE AILERON	36
3. MORPHING AILERON DESIGN	39
3.1 Description of the model	39
3.2 Design Loads	48
3.3 Structural Kinematic Concept	50
3.4 Actuation System Design	58
3.5 FE model and stress results at LL and UL	69
3.6 Aeroelastic Stability Analysis	86
3.7 Aileron Manufacturing	96
4. EXPERIMENTAL TESTS AND CORRELATIONS	103
4.1 Control Logic implementation	104
4.1.2 Selected actuator modelling	105
4.1.3 Morphing Aileron Controller strategy	106
4.2 GVT and numerical Correlations	109
4.3 Functionality Tests	110
4.4 Experimental shape	112
5. WIND TUNNEL TESTS	113
6. CONCLUSIONS	125
ACKNOWLEDGMENTS	130

List of Figure

Figure 1 – The Adaptive aileron – CAD	11
Figure 2 – A sequence of change in wing planform that characterize perching [1].	13
Figure 3 – Bird morphing wing adaptation to the new flight phases [2].....	14
Figure 4 – <i>Aulae</i> on bird wings (courtesy of Ron Dudley) (a) [3] and Slat on real aircraft (b)	14
Figure 5 - Interdependence of the major subsystems involved in the design of bio-inspired morphing concepts [4].....	15
Figure 6 – Mechanism sketch for lateral control of the Wright brothers glider (a), representation of the warped airfoil (b).....	16
Figure 7 - Variation of drag polar as a function of trailing-edge deflection [10].....	17
Figure 8 - Possible modifications on wing design [11].	17
Figure 9 - Flap and tab settings [11]	18
Figure 10 - <i>LD</i> for basic and modified wing [11]	18
Figure 11 - Estimated benefit of a morphing device on the a real aircraft [12].....	18
Figure 12 - Drag polar envelop in cruise for different flap angles [10].	19
Figure 13 - Aerodynamic efficiency increment at several flap deflections (a) and maximum increment of <i>E</i> (b) [10]	19
Figure 14 - Optimal TE angles [10]	20
Figure 15 – Pie chart of the percentage of emission by sector and by transport mode [13].	20
Figure 16 - CFD Mesh of the JTI multifunctional flap (a) ([15]) and the comparison of maximum lift coefficient increment (b); baseline green and morphed red (courtesy of CIRA).	21
Figure 17 - Schematic representation of the flap tip for load control.	21
Figure 18 - Schematic representation of the flap rib [16].....	22
Figure 19 - Morphing mode (a) and tip deflection (b) of the Clean Sky multifunctional flap (Courtesy of Unina).	22
Figure 20 - Flap rib with detail on the two actuation system and kinematic chain (Courtesy of Unina).....	23
Figure 21 – Assembly of the SARISTU morphing wing consisting of different morphing devices [18].....	23
Figure 22 - SARISTU ATED with detail on the rib kinematic [19].....	24
Figure 23 - SARISTU adaptive trailing edge containing morphing skins at upper and lower sides [18].	24
Figure 24 - Schematic representation of the FlexSys flap [22]	25
Figure 25 - Evolutionary trend in high lift systems [24].....	26
Figure 26 – Simplification of the high lift actuation systems over the last few decades	26
Figure 27 - Global scheme of the inboard and outboard A340 flap actuation system [23] ..	27
Figure 28 – A340 flap mechanism based on the link/track architecture [25].....	27

Figure 29 – Boeing 767 flap system: cruise position (a) and landing configuration (b) ([25])	27
Figure 30 – A350 XWB flap in cruise condition [26]	28
Figure 31 – A350 XWB with A/B and Tab deflection for roll control manoeuvre [26]	28
Figure 32 – Distributed concept versus concentrated actuation concept [28]	29
Figure 33 – Representative scheme of an Iron Bird Tool suitable for testing morphing devices	30
Figure 34 – Smart Wing program: (a) Wing twist by SMA torsional tube, (b) TE deflection actuated with SMA wires [29]-[31]	31
Figure 35 – Detail on the trailing edge SMA based mechanism [29]-[31]	31
Figure 36 – UCAV concept developed in Smart Wing project [29]-[31]	31
Figure 37 – Integration among the SMA concept on a flap prototype [32]	32
Figure 38 – PMA in uninflated and inflated configuration [33]	32
Figure 39 – Wind Tunnel prototype of a flap equipped with PMA: (a) inner view, (b) with flap deflected [33]	32
Figure 40 – Morphing Wing adaptation to the various flight condition: high lift, cruise, loiter and manoeuvres [34]-[36].	33
Figure 41 – NextGen wing design [35]	33
Figure 42 – EBEAM concept (a) and its implementation on an aircraft control surface (b) [37].	33
Figure 43 – Distributed concept of the Eccentric Beam based actuation concept	34
Figure 44 – Actuation system based in quick-return mechanism [19]	34
Figure 45 – Artistic Concept of the NASA idea of a morphing aircraft [38]	35
Figure 46 - Partners involved in the CRIAQ MDO505 project	37
Figure 47 – Wing box - Aileron demonstrator	37
Figure 48 – T/A isometric view	39
Figure 49 – T/A isometric view with detail on the internal wing box	39
Figure 50 – T/A assembly	40
Figure 51 – Schematic representation of the morphing aileron on a real wing [41]	41
Figure 52 – Airfoil target shapes	42
Figure 53 – “Iso-alpha” aileron shapes	43
Figure 54 – “Iso-mach” aileron shapes	43
Figure 55 – Zooming of the different shape for different AOA	44
Figure 56 – Aileron shapes for null tip deflection	44
Figure 57 - Final selected aileron morphed shapes	45
Figure 58 - Morphing rib architecture with blocks and links and hinges	46
Figure 59 - Morphing aileron structure: multi-box arrangement	46
Figure 60 – Dimetric view of the aileron morphed shapes	46
Figure 61 – Aileron digital mock-up: (a) transparent skin and (b) covered skin	48
Figure 62 – Aerodynamic grid (a) and loads distributed on the aileron	49

Figure 63 – Actuated and passive zones of the aileron	50
Figure 64 – Quick-return mechanism scheme	51
Figure 65 - Circular trajectories of sample points (E, F and G) during morphing (left) and position of hinges A, V and B (right).....	52
Figure 66 – Oscillating glyph mechanism with internal actuator shaft (O)	52
Figure 67 – MA of the mechanism for different geometrical parameters.....	53
Figure 68 – Rib rotation versus actuator shaft rotation (inner actuator).....	54
Figure 69 – Oscillating glyph mechanism with external actuator shaft (O).....	54
Figure 70 - MA of the mechanism for different geometrical parameters	55
Figure 71 - Rib rotation vs actuator shaft rotation (external actuator).....	55
Figure 72 – Conceptual scheme of the linear guide based on recirculating balls.....	56
Figure 73 – Conceptual scheme of the cam follower.	57
Figure 74 – Example of linear guides and cam followers	57
Figure 75 – Aileron inner structure with coloured segmented rib	59
Figure 76 – CAD of the linear guide with rollers.	59
Figure 77 – Schematic CAD model of the actuation mechanism concept based on the rollers.	59
Figure 78 – Precision linear slide with recirculating (left) and non-recirculating (right) ball carriages.....	60
Figure 79 - CAD of the actuation system concept using a precision linear slide mechanism	60
Figure 80 – Cam Follower components	60
Figure 81 - Cam follower-based actuation system	61
Figure 82 - Main components of the ball bearing guide mechanism	61
Figure 83 – Analytical scheme of the cylindrical bushing.....	62
Figure 84 - Ball bearing guide-based actuation system	62
Figure 85 - Comparison of MA and actuator shaft rotation achieved by the investigated actuation concepts.....	63
Figure 86 – Comparison between linear, analytic and multi-body simulation.	64
Figure 87 – Sketch of the concentrated load evaluation (hidden skin)	64
Figure 88 – Complete FE model of the aileron rib.....	65
Figure 89 - Beam displacement contour (left); guide reaction loads of 371 N (right)	66
Figure 90 - Beam displacement contour (left); guide reaction loads of 366 N (right)	66
Figure 91 - Beam displacement contour (left); guide reaction loads of 355 N (right)	66
Figure 92 – Stress contour on linear guide	67
Figure 93 - Stress peak in the contact region between slider and rail	67
Figure 94 - Comparison between analytical and numerical trend of Actuation torque and Mechanical Advantage versus Morphing Angle (ϕ).....	67
Figure 95 – Multi-body simulation with allowable design region for actuator torque (a) and linear guide vertical force (b)	68

Figure 96 - Reference system S1	69
Figure 97 - Aileron FE model	71
Figure 98 - (a) Aileron Rib solid mesh (CTETRA), (b) Spar solid mesh (CTETRA)	71
Figure 99 - FE model, materials contour plot (light grey: Al2024-T351, black: steel)	72
Figure 100 - FE model, materials contour plot, skin hidden, (light grey: Al2024-T351, black: steel)	72
Figure 101 – Mesh of the actuation transmission chain.....	73
Figure 102 - Detail of the linear guides mesh.....	73
Figure 103 - Connection pins between linear guides components	73
Figure 104 - Detail of the connection among the actuation transmission components	74
Figure 105 - Modelling approach for the hinged connection	74
Figure 106 - Fasteners modelling approach for rib-spar connection	75
Figure 107 - Fasteners modelling approach for rib-skin and spar-skin connection	75
Figure 108 – Pressure distribution along the aileron	76
Figure 109 – Vector representation of the distributed pressure applied to the structure	76
Figure 110 - Constraints along the linear guide.....	77
Figure 111 - Constraints on the crank	77
Figure 112 - Global aileron displacement distribution at LL condition	78
Figure 113 - Global aileron displacement distribution LL condition (skin hidden).....	78
Figure 114 – Global VM stress distribution on ribs at LL condition.....	79
Figure 115 – Element Stress Distribution above the threshold of 150 MPa.....	79
Figure 116 – Global VM stress distribution on links at LL condition.....	80
Figure 117 – Global VM stress distribution on spars at LL condition.....	80
Figure 118 – Global VM stress distribution on skin at LL condition.....	81
Figure 119 – Global VM stress distribution on Actuation Beam at LL condition.....	81
Figure 120 – Beam element stress distribution above threshold values of 320 MPa.....	81
Figure 121 – Von Mises Stress distribution around the most solicited linear guide.	82
Figure 122 - FE model used for the evaluation of reaction loads at wing box interface.....	83
Figure 123 - First buckling mode (instability of rib links, eigenvalue: -10.4, ref. loads: LL)	86
Figure 124 – Mode 1: freq = 0.0026 Hz.	87
Figure 125 – Mode 2: freq=41.379 Hz	87
Figure 126 – Mode 3: freq = 58.774 Hz	88
Figure 127 – Mode 4: freq = 120.27 Hz	88
Figure 128 – Wing box mesh: (a) complete model, (b) upper skin and support hidden, (c) wireframe view, (d) Jacobian ratio	89
Figure 129 – Actuator model	90
Figure 130 – T/A aerodynamic lattice.....	91
Figure 131 – Interpolation grid on aerodynamic model.....	91
Figure 132 – Aileron Harmonic: modal displacement on structural model (left), interpolation on aerodynamic grid (right)	92

Figure 133 - Vg plot for case 1	93
Figure 134 – Vg plot for case 2	93
Figure 135 – Vg plot for case 3	94
Figure 136 – Vg plot for case 4	94
Figure 137 – Mode 1: Aileron harmonic (left); Mode 2: T/A bending (centre); Mode 3: Aileron tab mode (right).....	95
Figure 138 – Flutter Speed versus aileron actuator stiffness.....	95
Figure 139 – Aeroelastic scheme for flutter validation	96
Figure 140 – Aileron assembly during manufacturing process	96
Figure 141 – Aileron segmented Rib with rotational hinges	97
Figure 142 – Enlargement on the Hinge 1 (a) and Hinge 2 (b) with internal bushing.....	97
Figure 143 – Connection link between non-consecutive rib plate 1 and plate 3.....	97
Figure 144 – Focus on the link pin of the rib plate 1 (a) and rib plate 3 (b)	97
Figure 145 – Actuation system components: Beam, plates and crank	98
Figure 146 – Linear guides (a) and double sided configuration partially integrated into the aileron (b)	98
Figure 147 – Full integration of the actuation kinematics and the rotary actuator into the aileron	99
Figure 148 – Actuation kinematic contained into the aileron structure	100
Figure 149 – Aileron cabling layout	101
Figure 150 – Cabling hole.....	101
Figure 151 – Synthetic representation of the aileron set-up inside the wind tunnel.....	101
Figure 152 – Actuator cabling.....	102
Figure 153 – Aileron leading edge with cabling hole	102
Figure 154 – Photo of the Actual Aileron Prototype.....	103
Figure 155 – Setup for aileron experimental campaign.....	104
Figure 156 - Block Diagram of an Electric Motor ([48])	104
Figure 157 - Block Diagram of Built-in Controller ([48])	105
Figure 158 - Bental RSA-6, Maximal Torque vs. Maximal Rotation Speed	105
Figure 159 - Frequency Response of the Servo-Actuator	106
Figure 160 - Controller Design Work-flow diagram ([49]).....	107
Figure 161 – dSPACE graphic interface unit during actuators bench test.....	108
Figure 162 - Actuator encoder signal: step function	108
Figure 163 - Actuator encoder signal: sine function	108
Figure 164 – Aileron GVT experimental setup	109
Figure 165 - Aileron Measurement Points.....	109
Figure 166 – Numerical and experimental normal modes comparison.....	110
Figure 167 – Normal modes correlation	110
Figure 168 - Morphing Aileron at various deflections.....	111

Figure 169 - Correlation between numerical and experimental: actuator rotation versus morphing deflection	111
Figure 170 - Dimetric view of the aileron morphed shapes respectively +5° and -2°	112
Figure 171 – Comparison between numerical and experimental aileron shapes	112
Figure 172 – Photo of the morphing aileron with leading edge holes numbering.....	113
Figure 173 – Procedure of removing the leading edge first screw	114
Figure 174 – Aileron tie rod	114
Figure 175 – Aileron shaft housing.....	115
Figure 176 – Nomenclature of the pressure taps	115
Figure 177 – Pressure taps position on the upper and lower side of the aileron.....	115
Figure 178 – Wing box prototype in the wind tunnel (a) and during aileron installation (b)	116
Figure 179 - Inner part of the wing (a) with detail on the actuator (b).....	117
Figure 180 – Morphing wing equipped with morphing aileron in a downward view (a) and upper view (b)	117
Figure 181 – Front view of the Morphing wing with wake-rake on the background.....	118
Figure 182 – Complete morphing wing in the wind tunnel at NRC (Ottawa)	118
Figure 183 – Rear view of the morphing wing.	119
Figure 184 – Morphing aileron with detail on morphed up and down deflection	119
Figure 185 - Pressure distribution around the morphing wing at increasing AOA and aileron morphing angle (a), (b) and (c).....	122
Figure 186 – Smoker tests with tip vortex in morphed down, baseline and morphed up .	122
Figure 187 - Lift coefficient versus angle of attack curve	123
Figure 188 - Drag coefficient versus angle of attack curve	123
Figure 189 - Drag polars with the envelope curve	124

List of Tables

Table 1 – CRIAQ project WP tiles	38
Table 2 – Work-packages, tasks and sub-task of the CRIAQ project.	38
Table 3 – T/A geometrical parameters	40
Table 4 – Wing box adopted materials.....	40
Table 5 – Optimized airfoil shape settings	42
Table 6 – Aerodynamic cases.....	49
Table 7 - Comparison of investigated actuation concepts.....	63
Table 8 – Actuator torque values	65
Table 9 - Aileron FEM, general data.....	70
Table 10 - Mechanical properties of adopted materials.....	71
Table 11 – Load resultant	76
Table 12 - MoS with respect to local plasticization at LL condition	82
Table 13 - MoS with respect to failure at UL condition	83
Table 14 - Reaction loads at wing box interface (limit condition).....	83
Table 15 - Actuator torque evaluation.....	84
Table 16 - Table of MoS for connections	85
Table 17 – Morphing aileron modal analysis: freq. and generalized masses	87
Table 18 – Wing box FEM elements summary	89
Table 19 – Actuator Stiffness	90
Table 20 – Flutter analysis results	92
Table 21 – Actuator characteristics	100
Table 22 – Wind tunnel test matrix.....	121

List of Acronym

MTOW	Maximum Take Off Weight
L/D	Lift over Drag
A/C	Aircraft
AOA	Angle of Attack
LE	Leading Edge
DOF	Degree of Freedom
T/A	Test Article
Cp	Pressure Coefficient
LL	Limit Loads
WTT	Wind Tunnel Tests
HL	High Lift
FO	Fiber Optic
ACTE	Adaptive Compliant Trailing Edge
MEA	More Electric Aircraft
HDL	High Lift Device
SMA	Shape Memory Alloy
PMA	Pneumatic Muscle Actuator
PAM	Pneumatic Artificial Muscle
UCAV	Unmanned Combat Air Vehicle
UL	Ultimate Loads
VM	Von Mises
MPa	Mega Pascal
MoS	Margin of Safety
SDOF	Single Degree of Freedom
GAF	Generalized Aerodynamic Forces
AIC	Aerodynamic Influence Coefficient
DLM	Doublet Lattice Method
CNC	Computer Numerical Control
PD	Proportional Derivate
EMF	Electro Motive Force

Abstract

Typically, aircraft roll control is accomplished by simultaneously moving ailerons together and in opposite angular direction. Nevertheless, throughout the flying range, more particularly in cruise conditions, it is highly desirable to increase aircraft aerodynamic performance by a differential control of the lift distribution over the wing span. Recent European design studies concerning morphing devices, such as the Clean Sky multifunctional flap or the SARISTU trailing edge device, have largely proved the potential of novel aircraft structural systems, aiming at adaptively modify the wing structural shape to reduce the induced drag penalty associated with off-design flight conditions. In particular, wing camber variation was achieved through adaptive wing trailing edges because of the highly associated L/D ratio enhancements. Such projects proved also the aileron region to be the one where higher cruise benefits could be achieved by local camber variations. Following the enthusiastic results, achieved with the Adaptive trailing edge device, a new challenge has been faced up. The former configuration did in fact refer to the standard position of the flap, leaving apart the aileron region. There are several reasons to leave that part unchanged. The most relevant may be associated to the fact that the aileron has a critical function in the aircraft flight and its collapse could lead to dramatic failures. The investigated configuration would have lied over an extended region of the aileron instead than a limited part, as in the case of a flap, characterised by a large chord. As a direct consequence, the available volumes are reduced and the installation of integrated actuators could have been a problem. Finally, the aeroelastic response of the device is critical as well and its strong modification should have been deeply studied. On the other hand, the studies on the ATED showed as the region, farer from the root, gave a more significant contribution to the aerodynamic behaviour. So, it was really interesting to investigate the possibility to extend the adaptive trailing edge technology to the aileron region. The occasion was given by a joint Italian/Canadian research activity fostered by the Consortium de Recherche et d'Innovation en Aerospaciale au Quebec (CRIAQ). The activity aimed at realising a full-scale demonstrator of a wing section in the tip region for investigating the capability of wing box and trailing edge morphing device, to ensure a certain level of flow control and aerodynamic performance variations, respectively. The first issue was in charge of the Canadian team (ETS, NRC, Thales Aerospace, Bombardier AS), while the Italian group (University of Naples and CIRA) aimed at realising a device for the aileron camber control. The enlisted problems were all evident at the very first approach. Volume limitation forced the designers to follow a different strategy. Instead of having a couple of actuators acting on each rib, the architectural layout was specialised per each single bay. At the aileron root this possibility was maintained, while the more external two bays were commanded by a single actuator. In other words, the last two segments were made of two slave and a master ribs, driven by a single actuator. Calculation showed as this configuration was able to maintain the specified loads. Aeroelastic studies confirmed the reliability of the device, in

sense that the selected architecture was demonstrated to be safe in the design flight conditions. The adaptive aileron finally maintained the original capability while ensuring morphing characteristic. This target was accomplished by realising a device with two separate motor system. The first, acting on the main aileron shaft, to preserve its characteristic dynamic response for flight control. The second, acting on the rib, implemented the searched camber variations to follow the aerodynamic necessities related to fuel consumption. Another relevant point concerns the skin. In order to check the possibility of skipping the need of implementing a compliant solution, a heavy and sophisticated element, the single hinged blocks were properly shaped to slide one into the other like a meniscus. This solution was however strongly correlated to manufacture tolerances and the assembly precision, because small deviation could have had a significant impact on the kinematic performance. As usual, vantages and disadvantages try to compensate each other. A schematic view of the morphing aileron is reported in Figure 1.



Figure 1 – The Adaptive aileron – CAD

The innovative device can be considered as a system with augmented capabilities aimed at working in cruise, by means of symmetric deflection, to obtain a near optimum wing geometry enabling optimal aerodynamic performance. The approach, including underlying concepts and analytical formulations, combines design methodologies and tools required to develop such an innovative control surface. A major difficulty in the development of morphing devices is to reach an adequate compromise between high load-carrying capacity to withstand aerodynamic loads and sufficient flexibility to achieve the target shapes. These targets necessitate the use of innovative structural and actuation solutions. When dealing with adaptive structures for lifting surfaces, the level of complexity naturally increases as a consequence of the augmented functionality of the designed system. In specific, an adaptive structure ensures a controlled and fully reversible transition from a baseline shape to a set of different configurations, each one capable of withstanding the associated external loads. To this aim, a dedicated actuation system shall be designed. In addition, the adopted morphing structural kinematics shall demonstrate complete functionality under operative loads. Such a morphing device wants to augment the former device by adapting local wing camber shape and lift distribution through a quasi-static deflection, its excursion ranging

into few unit of degrees, positive and negative. In a morphing aircraft design concept, the actuated system stiffness, load capacity and integral volumetric requirements drive flutter, strength and aerodynamic performance. Design studies concerning aircraft flight speed, manoeuvre load factor and actuator response provide sensitivities in structural weight, aeroelastic performance and actuator flight load distributions. Based on these considerations, actuation mechanism constitutes a very fundamental aspect for adaptive structures design because the main prerequisite is to accomplish variable shapes within the physical constraints established by the appropriate actuation arrangement.

This thesis addresses the design of a morphing aileron with a specific focus on the structural actuation system sizing and integration while the structural sizing was under Unina responsibility. Particular focus is given to the numerical validation of the entire aileron integrated with the actuation leverage by means of FE model and experimental tests campaign. The aileron actuation system is driven by load bearing servo-electromechanic rotary actuator in a distributed and un-shafted arrangement which combine load carrying and actuation capacities. The use of electro-mechanical actuators is coherent with a “more electric approach” for next-generation aircraft design. Such an actuation architecture allows the control of the morphing structure by using a reduced mass, volume, force and consumed power with respect to conventional solutions. Benefits are obvious. No hydraulic supply buses (easier to maintain and store without hydraulics leaks), improved torque control, more efficiency without fluid losses and elimination of flammable fluids. In addition, it is potentially possible to move individual ribs either synchronously or independently to different angles (twist) in order to enhance aerodynamic benefits during flight. On the other side, actuators susceptibility to jamming may represent the most important drawback that can be tested and prevented by means of an *iron bird* facility.

Finally, the realised system was assembled onto a wing model and tested in a wind tunnel at the National Research Council (NRC) facilities in Ottawa (CAN). On the same model, the adaptive wing box was also installed. The adaptive aileron device proved its functionality in real flow conditions and the main aerodynamic results are herein presented and widely described.

The developed device has a lot of further potentialities, that will be object of further works and publications and that are currently explored by the authors: for instance, by giving it a large bandwidth, it could be used as an additional load alleviation device for the outer wing in order to reduce peak loads for gusts. Moreover it can be tailored for active load control distribution in order to modify spanwise lift distribution obtaining a reduced wing root bending moment; in such a manner a lightweight design can be assessed.

1. Morphing Structures State of Art

1.1 *The intelligent wing*

Men desired to flight since very ancient times being inspired by bird's capability to dominate sky. Nature offers a rich seam of inspiration for a new generation of morphing wing design across a wide range of scales of interest to engineers going from the biggest birds to the smallest insect. For example, birds achieve their wing morphing capability by using flexible lifting surfaces, stiffened by hollow bones attached to strong muscle. All the flying creatures of the world show an inherent capacity to adapt, in a fraction of a second, their wing shape as the flight condition changes. A very interesting example is represented in Figure 2 that show perching sequence of an eagle. As reported in [1], birds accomplish changes in wingspan and area by firstly flexing their wings, and then adopting a characteristic M-shape planform with the inner wing section sweeps forward, and the outer section sweeps backwards.

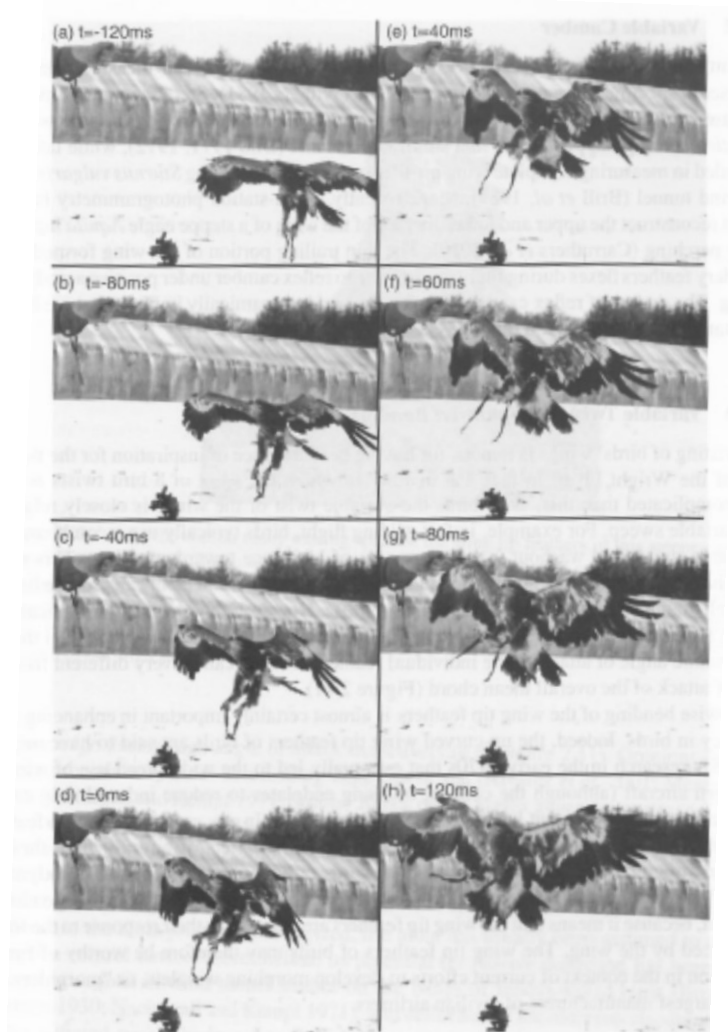


Figure 2 – A sequence of change in wing planform that characterize perching [1].

This characteristic wing shape causes a drastic reduction in area and brings the centre of pressure forward, initiating then a rapid pitching manoeuvre. At the end of the pitching procedure, the wings are held at high angle of attack in order to enter deep stall producing

thereby very high drag forces that are required for aerodynamic braking. This is a very fast movement which occur in almost 0.2 second and it is an important example for understanding how morphing can be used to control unsteady flight manoeuvres. It is noteworthy that “inspiration from nature” is the keywords that lies behind any morphing idea. Many researchers and engineers around the world have been inspired by the multi-tasking flight capabilities of birds, which tend to cover a broad range of mission phases ranging from slow, near-hover flight to aggressive dives, in order to develop innovative methodologies involved to resolve many technological problems. Just only observing birds and other flying creature wings it is possible to appreciate the complexity of such systems showing intrinsic capacities to adapt instinctively and immediately to the environment. In particular, birds are able to articulate their wings in a craning motion to vary the dihedral or sweep angles (Figure 3), wing area, wing planform, wingspan, and other parameters. These changes allow the bird to quickly adapt between soaring, cruising, and descending flight [2].

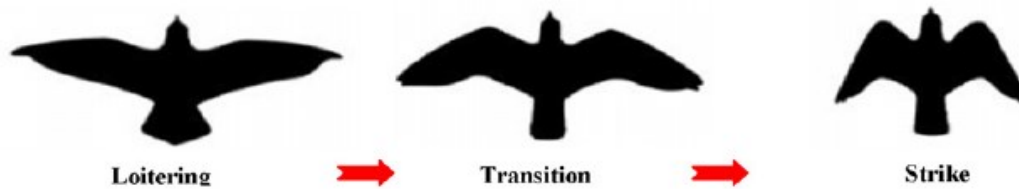


Figure 3 – Bird morphing wing adaptation to the new flight phases [2]

It's clearly visible the presence of the so-called *Aulae* (Figure 4 (a)) on the bird wing leading edge which allow to an exhaustive comprehension of the correlation between bird's flight dynamics and a flying human machine.

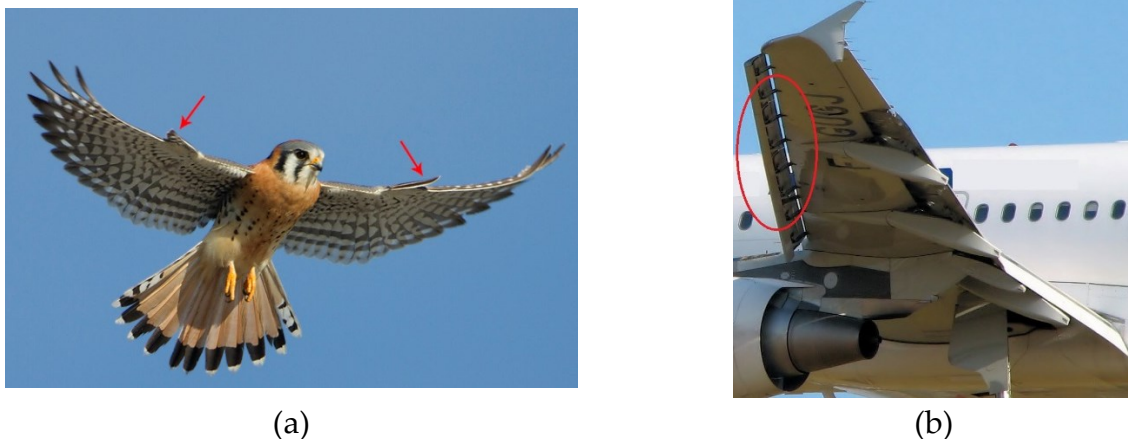


Figure 4 – *Aulae* on bird wings (courtesy of Ron Dudley) (a) [3] and Slat on real aircraft (b)

Such an appendix is free to move on the leading edge. It allows the bird to flight at very low speed increasing locally the angle of attack in order to prevent stall. In aircraft, this device is usually referred to as LE slat (Figure 4 (b)) and it has the same functionality. Despite the past century of innovation in aircraft technology, the versatility of modern aircraft remains far worse than airborne biological counterparts. The shape modification accomplished by birds stands as one of the few examples of true morphing. As such, the aircraft engineers worldwide are devoting extensive effort to integrate these concepts in advanced mechanical systems in order to bring morphing technology to the readiness level of a flight vehicle. The

key purpose is to realize an innovative device capable to adapt itself to the external environment conditions. Morphing structures exhibit then an intrinsic multidisciplinary attitude that can be summarized in Figure 5. It becomes clear the need for a multidisciplinary approach involving structures, actuation, sensing and control.

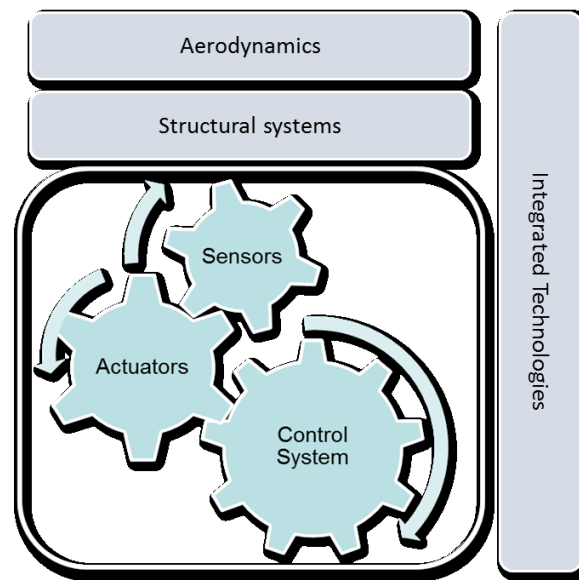


Figure 5 - Interdependence of the major subsystems involved in the design of bio-inspired morphing concepts [4]

As reported in [5], any smart structure shall fulfil a paradox which relates two conflicting goals. Firstly, a morphing structure shall exhibit large strains, to modify its shape in order to meet specific targets. On the other hand, it shall be adequate stiff to withstand external loads. Then its architecture and design shall result into a compromise between load-bearing capability and structural flexibility. Compliant and rigid-body mechanisms are two classes of mechanical systems capable to accomplish such targets within the limits imposed by a typical aircraft mission. A rigid-body structure works out the morphing paradox by means of a segmented multi-box arrangement employing standard hinges driven by an internal actuation system composed of load-bearing actuators. The actuation mechanism is totally integrated into the structure and its authority drives the morphing capability. This configuration brings the main advantage of being more similar to an aeronautical configuration but it is characterized by high stresses concentration located around the hinges and actuator mechanism while the other structural elements are not excessively involved. On the other hand, compliant structures allow large deformations by exploiting the elastic properties of their components leading to a more uniform energy distribution among its parts. It is monolithic joint-less mechanism properly optimized to distribute small strain and to avoid high stress concentration. In addition, it is noteworthy that morphing devices as well as flying creatures must be able to detect or sense the condition of the atmosphere around them, as well as their own position and structural configuration, in order to react accordingly. Therefore, to create adaptive intelligent structures, it becomes crucial to provide the system with a constant awareness of its own condition and the environment where it is in. This may be achieved by integrating a proper sensor network into the structure. Information from the sensors, such as air speed, altitude, air pressure, position relative to other objects, is then used by the global control system. The main functionalities of an intelligent system can be summarized, as described in [1], into three tasks: when to adapt, how to adapt and learning to adapt. The first one is driven by mission

purposes, which define the optimal configuration on the base of specific system requirements. *How to adapt* is a problem regarding sensing, actuation and control laws, which are very critical. Hence, although an animal's wings may be able to change shape in a complex manner, the total number of independently controlled degrees of freedom may not be high. This indicates that a smart structure is built upon relatively simple principles. It will be actuated in one point and, by means of movable structural elements with limited DOF; the movement is transmitted to the whole structure so that the wing will be built to adapt at loading rather than to resist it.

The morphing idea was well known by the engineering since the begin of aviation such as the Wright brothers which built the first heavier than air aircraft with engine with twisted wing for roll control. In fact, the wings of the first aircraft where essentially of fixed geometry with limited capability for flight control and manoeuvres. However, since the realization of the first glider, it was soon discovered that a camber variation guarantee an improved manoeuvrability. Lateral control was realized by twisting the wing by means of a system made of cables. The mechanism is depicted in Figure 6 (a) and (b). It can be viewed as the first practical application of varying camber. However, wing warping did not remain practicable very long because the airplane structural stiffness increased with the need of a higher flight speed (resulting in onerous aerodynamic loads) and best performance which require airplanes more heavy and greater.

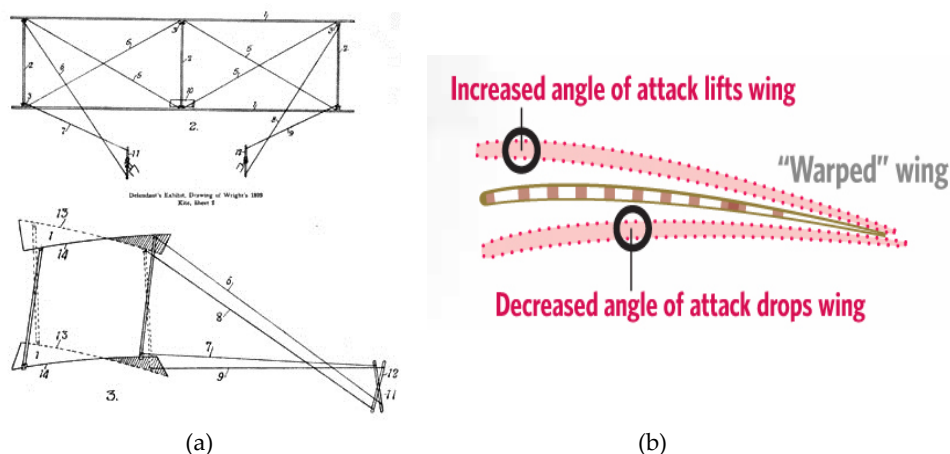


Figure 6 – Mechanism sketch for lateral control of the Wright brothers glider (a), representation of the warped airfoil (b)

Nowadays, aircraft wings are optimized for a single design point. Such a compromise geometry allows aircraft to fly at a range of flight conditions but outside the design point the performance are far from being optimal. So better performance at design point leads to worse off design performance ([6]&[7]). Except for the variable sweep, the first build morphing concepts were applied to lightly loaded, relatively low-speed airplane designs. It is reasonable to ask why we should invest more efforts in morphing wings when this concept was tried in the past and has had so little impact. The answer to this question is related with the technology that exists today, compared to that which existed several decades ago. First of all, many new, novel smart materials, material systems and actuation devices have been developed over the last few years. These developments allow designers to distribute actuation forces and power optimally and more efficiently. Design topology optimization allows for an optimal distribution of skin thickness and system compliancy. Furthermore, missions today are more flexible. Aircraft versatility is growingly becoming an added value, especially for unmanned vehicles and long range aircraft. To date, aircraft

is provided by numerous control systems which enable a sort of “adaptation”. In fact, lifting devices such as flaps, slats, aileron and spoilers, are necessary to increase wing chord, camber and therefore the lift distribution during the entire mission envelope. Flap and slat can be advantageous for certain flight conditions such as take-off and landing while due to gaps with the wing box, at high speed they produce un-wanted aerodynamic penalty. These are few examples that indicates how geometry changes represent a first concept of morphing but their benefits are limited if compared with those that could be obtained from a no-gap continuously deformable wing. What is immediately evident is the aerodynamic efficiency (L/D) enhancement by implementing a chord-wise camber variation on the trailing edge because from aerodynamic, as well as structural points of view, small modification could bring positive impact on performance ([8]). Throughout aircraft flying range, more particularly in off-design flight segments such as take-off, landing, climbing, descent, loiter, but also cruise, it is highly desirable to keep aircraft aerodynamic efficiency at the optimal level. Modifying wing shape during cruise, for instance, an optimum C_L vs C_D curve can be obtained, as an envelope of the different morphed conditions enabled to compensate the aircraft weight reduction due to the fuel consumption (>30% for long distance flight [9]). Such a gain is even more dramatic in climb or descent due to the higher aerodynamic margins with respect to the passive counterpart. The overall benefit can thus be estimated by considering all the operative drag polars obtained for all the flight conditions (Figure 7). [4]

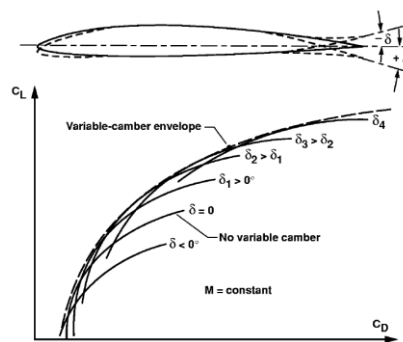


Figure 7 - Variation of drag polar as a function of trailing-edge deflection [10]

In [11], lift-to-drag ratio improvements were estimated with the purpose to formulate a new wing concept. Several possible modifications to the wing geometry are assessed, as reported in Figure 8.

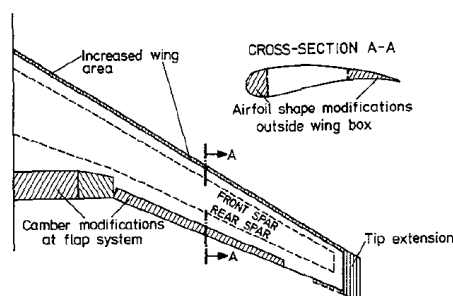


Figure 8 - Possible modifications on wing design [11].

Each modification hides drawbacks and benefits which lead to the conclusion that, excluding changes in the wing box, only the airfoil LE and TE shape variation can be implemented without neither additional structural weight (except the one introduced by

the device itself) nor large effort in redesign wing. Different camber modifications across the wing span trailing edge were designed. It consist of using flap and tab deflections both independently and combined as shown in Figure 9.

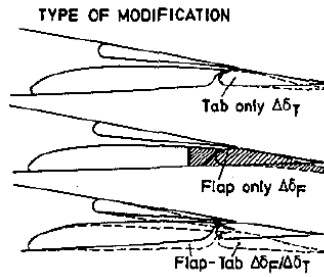


Figure 9 - Flap and tab settings [11]

The main results obtained from the analyses and from wind tunnel tests, show that when compared to the basic research aircraft, the optimum lift-to-drag ratio is increased by about 2% and is shifted to higher lift coefficient (Figure 10).

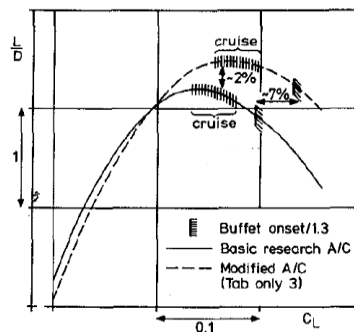


Figure 10 - L/D for basic and modified wing [11]

Related to the previous target, variable camber wing can be also investigated to control the spanwise load distribution as depicted in Figure 11. It was demonstrated in [11][10] and [12] that replacing the conventional hinged flap with a flexible morphing device can save up to 5% in fuel use across the flight envelop (Figure 11 (b)) and furthermore improving control authority and alleviate wing root bending moment.

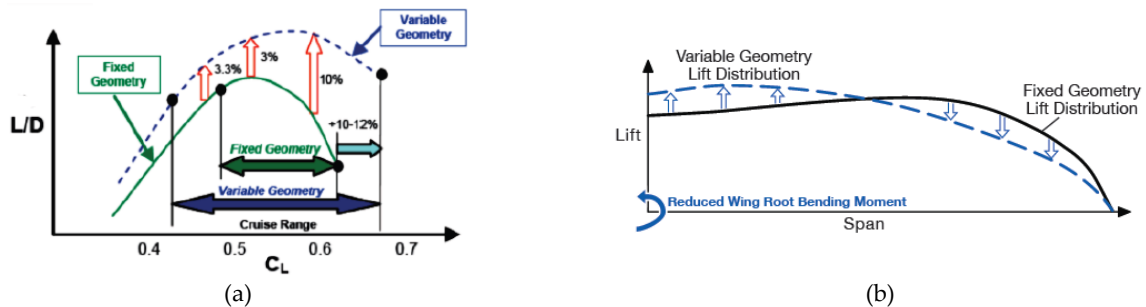


Figure 11 - Estimated benefit of a morphing device on the a real aircraft [12]

Wing camber variation may have the effect to either redistribute the wing lift in order to achieve an elliptical lift distribution ensuring the lowest induced drag or to move the lift resultant inboard, thus reducing the wing root bending moment with positive effect of the structural stress. The two targets seem to be contradictory although multi-objective optimization tasks may be performed. This indicates another important application of the morphing structures that is finding more interest: load control and gust load alleviation

respectively in static and dynamic regime. It is clear that morphing structures technology can be tailored on the base of a specific application such as improve aerodynamic performance (increase E_{max}) or increase fatigue life by reducing bending stress.

Other more recent studies can be found in literature in order to analytically prove the benefit of a variable camber wing for a transportation aircraft such as the one reported in [10]. It shows the influence of camber variation, which has been simulated as an aileron-type trailing edge deflections, in the performance of a generic wing profile merging theoretical concept and wind-tunnel data with the objective to maximize the L/D in high speed conditions. Starting from the complete drag polar equation for a reference vehicle (Lockheed L-1011), all the terms are computed from flight results at Mach equal to 0.83 and reported in the diagram in Figure 12 and Figure 13 for different flap deflections.

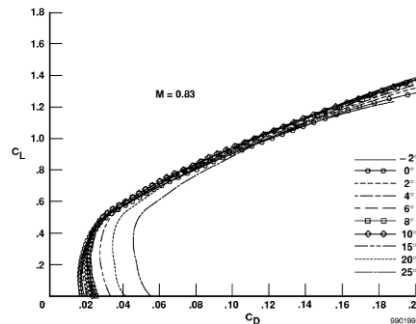


Figure 12 - Drag polar envelop in cruise for different flap angles [10].

The aerodynamic trend represented above, shows that when deflection occurs, all the drag polars cross around a pivot point for relatively high lift coefficients while shift on the left for low C_L . Figure 13 (a) shows the percent of change in L/D as a function of C_L respect to the un-cambered configuration. The main result is that for $C_L \sim 0.35$ no benefit occur as it is clearly visible in the Figure 13 (b).

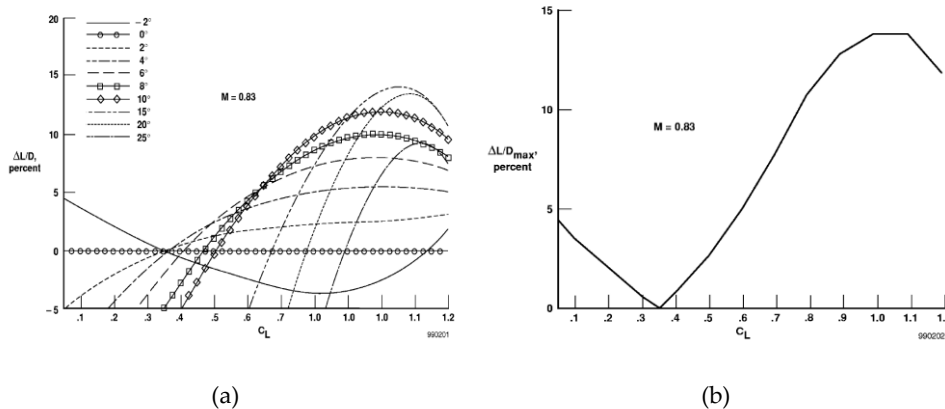


Figure 13 - Aerodynamic efficiency increment at several flap deflections (a) and maximum increment of E (b) [10]

It is also important to see the flap deflection required to obtain the maximal L/D at a given C_L (Figure 14).

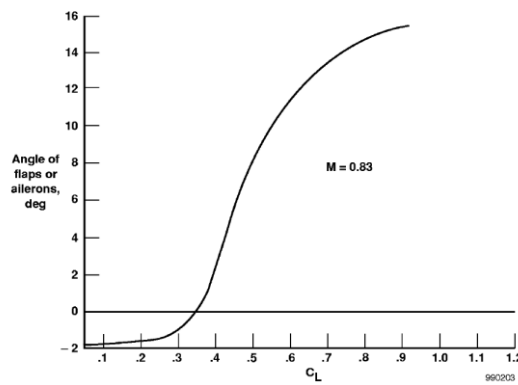


Figure 14 - Optimal TE angles [10]

The variation shows that for low lift coefficients it is required to deflect the trailing edge up (negative sense) in order to attain efficiency improvements otherwise increased down deflections (positive sense) are required for C_L greater than 0.35. Cruise condition occur at C_L in the range from 0.4 to 0.5 where it is evident that the improvements produced by variable camber wing are in the range of 1-3 percent which is related to the percent of fuel consumption. In this way, using a simple approach, the morphing benefits were demonstrated.

The growing attention of the aircraft industries for the morphing technologies is related primarily to the prediction of an increasing number of passengers in the next 20 years. It is estimated that the equivalent of 1300 new international airports will be required by 2050 with a doubling in the commercial aircraft fleet. The challenge facing aviation is to meet the predicted growth in demand for air travel (increasing 4-5% per annum over the next 20 years) but to do so in a way that the environment is protected. The EU has put a range of policies in place aiming to lower emission from the transport sector including aviation. As visible in the diagram in the transport sector has the second biggest greenhouse gas emissions in the EU. More than two thirds of transport-related greenhouse gas emissions are from road transport (Figure 15). However, there are also significant emissions from the aviation and maritime sectors and these sectors are experiencing the fastest growth in emissions, meaning that policies to reduce greenhouse gas emissions are required for a range of transport modes.

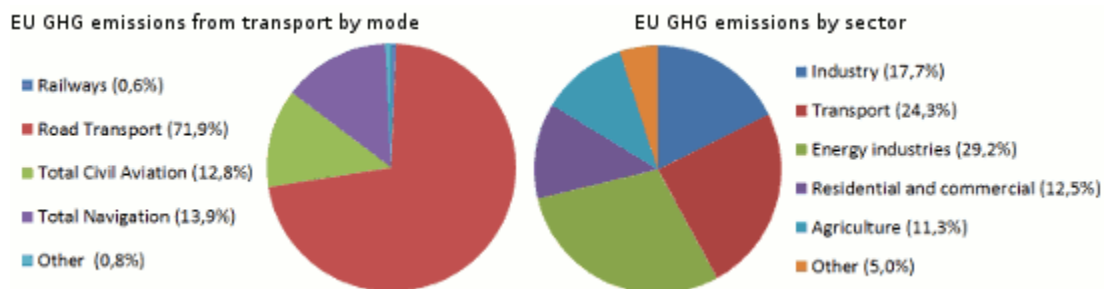


Figure 15 – Pie chart of the percentage of emission by sector and by transport mode [13]

The aviation industry in Europe has long recognized this challenge and in 2001 the Advisory Council for Aeronautical Research in Europe (ACARE [13]) established the following targets for 2020 (compared to 2000):

- reduce fuel consumption and CO₂ emissions by 50% per passenger kilometer
- reduce NO_x emissions by 80%
- reduce perceived noise by 50%

make substantial progress in reducing the environmental impact of the manufacture, maintenance and disposal of aircraft and related products. ACARE has identified the main contributors to achieving the above targets. The predicted contributions to the 50% CO₂ emissions reduction target are:

- Efficient aircraft: 20-25%
- Efficient engines: 15-20%
- Improved air traffic management: 5-10%

In recent years, European community funded many research program involved to improve the morphing structures technology readiness level. Clean Sky [14] is the most ambitious aeronautical research program ever launched in Europe. It aims is to develop breakthrough technologies to significantly increase the environmental performances of airplanes and air transport, resulting in less noisy and more fuel efficient aircraft. In this context, an innovative flap morphing full-scale prototype has been realized for application on next generation green regional aircraft (CS-25 category). The first studies were limited to a portion of the flap element. An innovative structural concept was then assessed in order to ensure the reversible transition from the nominal to the target shape of the flap segment, carefully validated through advanced finite element model and experimental tests on a full-scale test article. The main target was to implement a multifunctional flap addressing camber modifications during take-off and landing improving thus high lift performance (Figure 16 (b)) and also load control during cruise (high speed, flap in stowed configuration, (Figure 17) through the controlled deflection of the tip segment ($\pm 8^\circ$ of the 10% of the local chord).

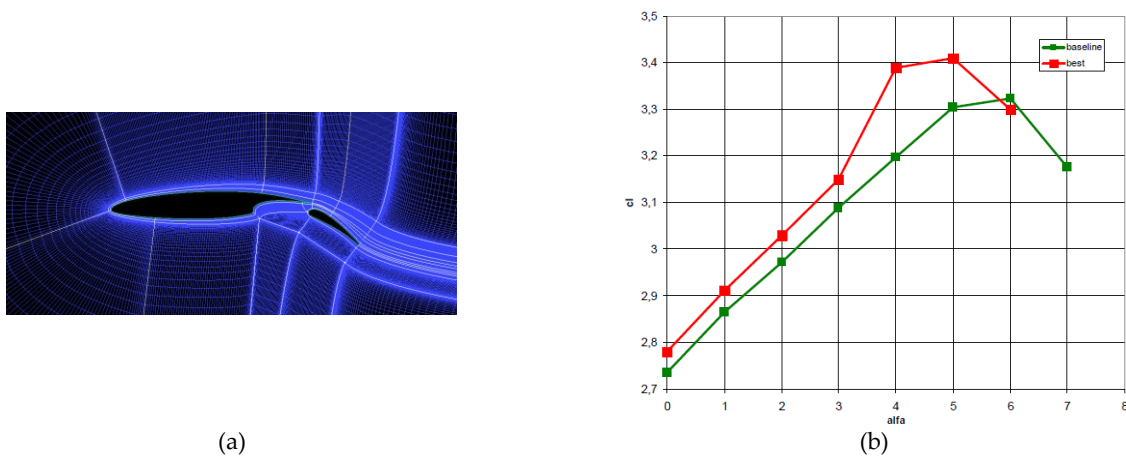


Figure 16 - CFD Mesh of the JTI multifunctional flap (a) ([15]) and the comparison of maximum lift coefficient increment (b); baseline green and morphed red (courtesy of CIRA).

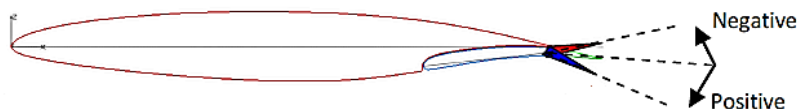


Figure 17 - Schematic representation of the flap tip for load control.

In [16], the complete design and validation phases of the Clean Sky flap architecture are described. The flap rib is segmented in several blocks as reported in Figure 18 and the architecture is called SACM, acronym of Smart Actuated Compliant Mechanism.

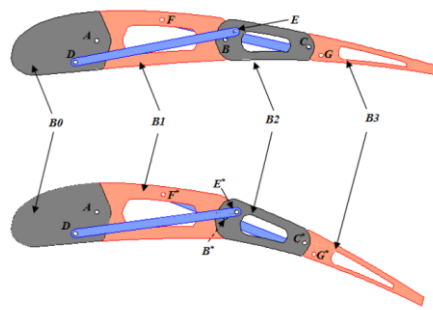


Figure 18 - Schematic representation of the flap rib [16]

Referring to the unmorphed and morphed airfoils of the flap element, the conceptual layout of an articulated (*finger-like*) rib structure was assessed in order to physically realize the transition from the baseline airfoil configuration to the target one. The rib structural concept is characterized by four main plates: B0, B1, B2 and B3. B0 and B2 have the same middle plane; B1 and B3 are staggered respect to them sharing always a common middle plane. Each plate is connected to the adjacent one by a hinge located on rib camber line (points A, B and C, respectively at 20%, 50% and 70% of rib chord). Plate B0 is linked to plate B2 by means of a rod element hinged at points D and E, hinges D and E being respectively located on B0 and B2. Plate B1 is linked to plate B3 through a second rod hinged at points F and G. Crossed links (DE and FG) positions have been conceived in order to assure specific rotation ratios between adjacent plates and an overall plates movement useful to match the target morphed shape. More in detail, considering plate B0 fixed on flap strut, a downward rotation of B1 around A makes all the other plate to move so that the final positions of hinges B and C (marked with a * in Figure 18) are on the camber line of the morphed airfoil. As a result, the rib architecture represents a single degree-of-freedom system; if a single plate is moved by a unique actuator, all the other plates are driven to move in compliance with the final shape to be achieved. From a low TRL device representative of the first two bays of the flap, the entire 3.60 meters flap was designed and manufactured. The final flap prototype structural layout, based on the aforementioned mechanism, are depicted in Figure 19 where the morphing mode and the tip deflection are shown respectively in (a) and (b).

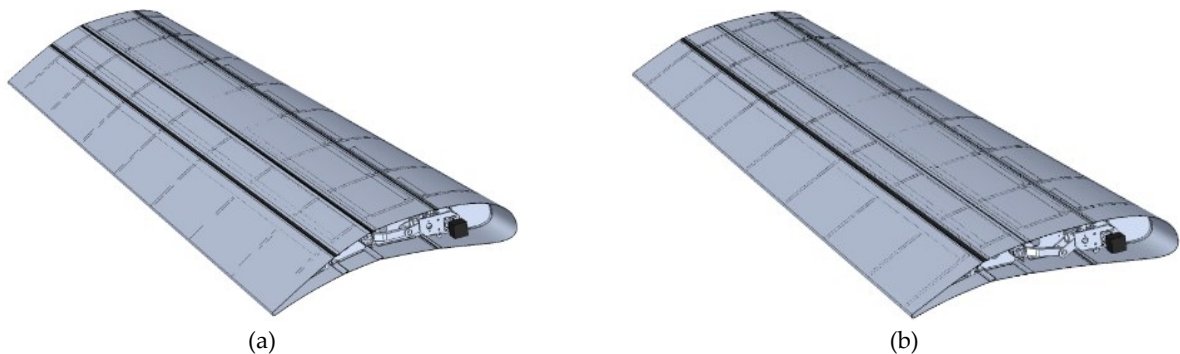


Figure 19 - Morphing mode (a) and tip deflection (b) of the Clean Sky multifunctional flap (Courtesy of Unina).

The high complexity of the system involved a detailed design. The entire flap is moved by two independent kinematic chain driven by rotary stepper actuators (Figure 20). One actuator is involved to assess the first morphing mode transmitting the shaft rotation to the rib hinge B by means of a leverage, furthermore, the other one is directly connected to the link L2 which varies its length assuring the tip deflection.

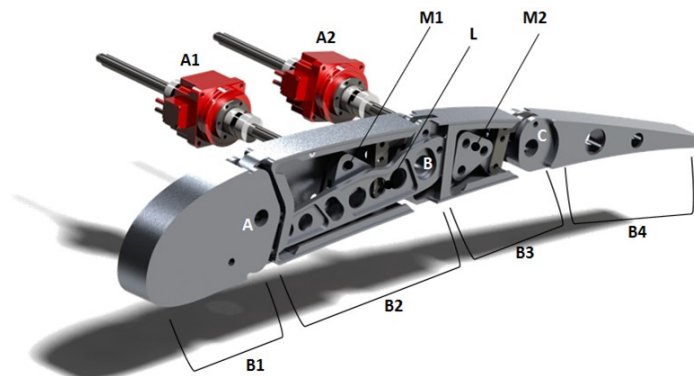


Figure 20 - Flap rib with detail on the two actuation system and kinematic chain (Courtesy of Unina).

At the same time, SARISTU [17] (acronym of Smart Intelligent Aircraft Structures) is a large-scale integrating project, coordinated by Airbus, which aims at achieving reductions in aircraft weight and operational costs, as well as an improvement in the flight profile specifically related to aerodynamic performance. It consists of a joint integration of different conformal morphing concepts in a laminar wing with the aim to improve aircraft performance through a 6% drag reduction inside the lift coefficient range usually devoted to cruise, with a positive effect on fuel consumption. The final product of the project was the first full-scale completely morphing wing tip prototype, ever assembled in Europe, at Finmeccanica Headquarters (Pomigliano, Italy), Figure 21. The innovative seamless morphing wing incorporates a gapless morphing leading edge, a morphing trailing edge and an adaptive winglet.



Figure 21 – Assembly of the SARISTU morphing wing consisting of different morphing devices [18].

The adaptive trailing edge (ATED) device is depicted in Figure 22, showing the entire trailing edge in morphed up and morphed down configuration with a detail in correspondence of the root rib in order to better visualize its structural layout. The actual prototype and the morphed positions are shown in Figure 24.

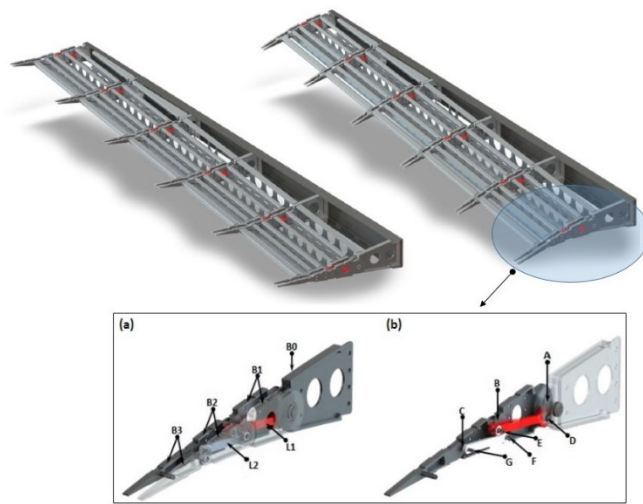


Figure 22 - SARISTU ATED with detail on the rib kinematic [19]



Figure 23 - SARISTU adaptive trailing edge containing morphing skins at upper and lower sides [18].

Also in this case, the rib was designed as a rigid-body mechanism. In fact, each rib block is composed of two plates and the link (L1 and L2) are positioned in the rib middle plane in a symmetric configuration in order to avoid torsional solicitations when loaded. Additionally, the entire ATED is moved by a dedicated actuation system and controlled by an appropriate feedback logic using shapes measurement from strain data coming from a distributed fiber optic (FO) sensor network.

Morphing technology is now approaching the high maturity practices for integration on real aircraft. This ambitious objective of testing morphing in flight has been recently achieved by FlexSys Inc. in US. FlexSys has concluded the first flight test of an Adaptive Compliant trailing Edge (ACTE) mounted on the experimental NASA Gulfstream vehicle. It is a compliant lightweight seamless shape-adaptive control surfaces able to produce large camber changes (-9 to +40 degrees), span-wise twist and high response rates (50 degrees/sec) throughout the flight regime. The multi-element hinged flap was replaced with a compliant control surface including inboard and outboard compliant fairings ([20]&[21]). The main ACTE characteristics are shown in Figure 24.

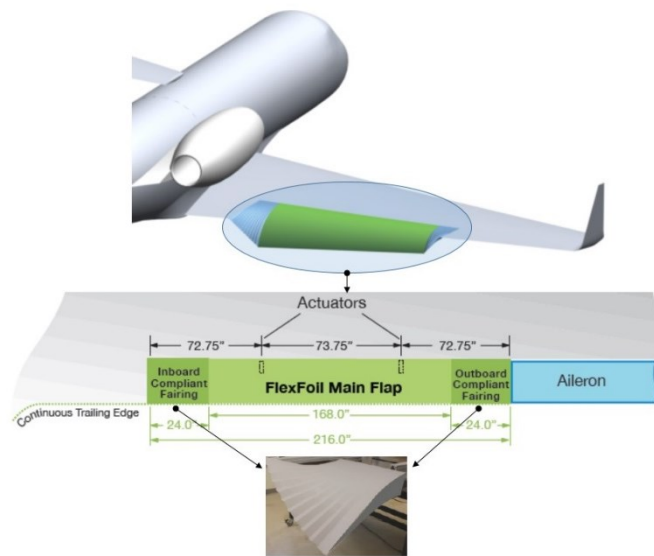


Figure 24 - Schematic representation of the FlexSys flap [22]

It must be said that perhaps, that FlexSys conducted the first experimental flight with a truly innovative technology, approaching to the engineering dream of design an optimized full-adaptive wing reaching in this way what the nature performed on birds. Clearly, Europe moves in the same direction with focus on a 100 seats transportation aircraft. The project Airgreen 2 (Clean Sky 2) aims at achieving the objective to conduct, in 2020, the first flight test on a morphing winglet on board of an experimental regional turboprop aircraft. Only after this important experimental event, the road for future implementation and commercializing of the morphing devices will be crossable and downhill.

1.2 Actuation system for morphing application

The state-of-the-art of high lift actuation systems of aircraft control surfaces predominantly consists of mechanical transmission shafts moved by rotary or linear hydraulic actuators with common control valves. These architectures assure a synchronous, safe and reliable deployment of all HLD but with limited flexibility [23]. The main functionality of the high lift devices is to provide lift increment at low speed condition (take/off and landing) so that the clean wing is optimized for the cruise speed regime. There are a lot of HLD on wing aircraft such as plain flaps to Fowler flaps with single, double, and even the most complex triple slots (Boeing 747). The design and optimization of high lift systems is one of the most complex task in aircraft design. It involves a close coupling of aerodynamics, structures and kinematics. The evolutionary trend of the HLD has been strongly driven by the dramatic improvement in aerodynamic tools optimization and in computational systems for complex structure simulations (multi-body kinematics). At the early stage, the research of aerodynamics high lift performance (C_{Lmax}) was achieved by means of multi-slotted experimentally validated two dimensional flap design. These systems allowed to achieve satisfactory performance with penalties in structural complexity and weight and therefore in costs that were not sustainable in the current applications. Later on, the improvement in computation fluid dynamics has permitted to carefully optimize flap systems in two dimensional flow with a clear advantage for fowler mechanism that allowed to reach higher values of maximum lift due to the effect of an increased lifting surface. Such fowler mechanism, on the other side, required even more complex kinematic actuation system due

to a combination of two movement: one translation plus a rotation. The fowler flap deployment mechanisms were designed by using linear or curved tracks in conjunction with revolute joint for the rotation, but unfortunately, the high lift values achieved were compensated by the relatively high weight penalties introduced by such systems. The reason for such high weight drawbacks were due to very intensive loads to be withstood by track bearings with also subsequent high maintenance costs. More recently, the research for aerodynamic efficiency and reduced weight penalties and complexity has been fostered by large utilization of multi-body system optimization that permitted the development of lighter and more efficient kinematic mechanism such as multi-link system. Such devices permits to match even very complex aerodynamic requirements with relatively structurally efficient system. As a matter of fact, today it seems very difficult to further improve in terms of an optimum balance among aerodynamic, structural weight and complexity the current system namely A350 or Boeing 767, this appear evident by the flattening of the curve in Figure 25.

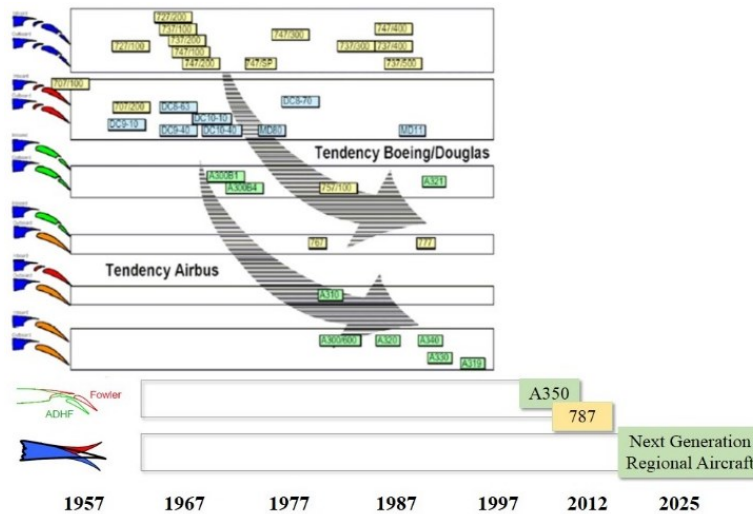


Figure 25 - Evolutionary trend in high lift systems [24]

From the previous graph, it is evident that today's high lift system are moving toward the development of innovative mechanisms with continuous curvatures, leading to the removal of gaps in order to obtain the same performance with the less deflections. In other words, this means implementing morphing concepts, as highlighted in the graph reported in Figure 26.

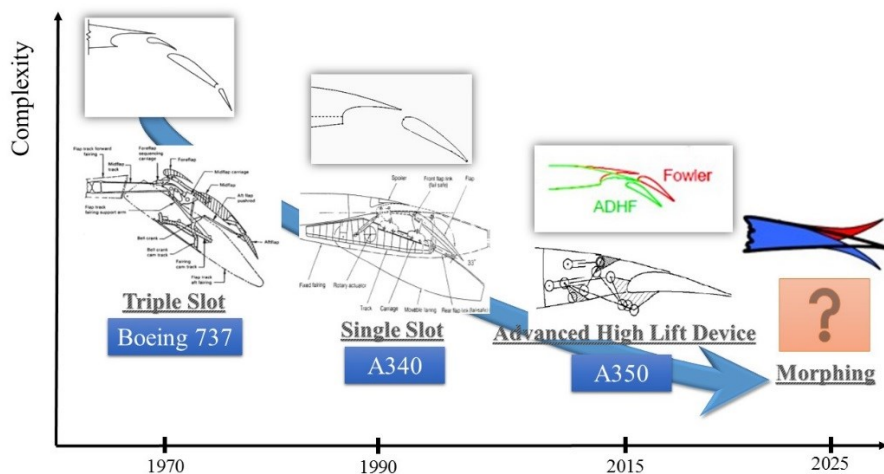


Figure 26 – Simplification of the high lift actuation systems over the last few decades

Additionally, flap mechanisms must be reliable and fail-safe. In order to not violate safety needs, the driving idea is to elude a multitude of links and joints in series, where high load concentrations are located; because the failure of any one of which could either lock up the flap, make it collapse. There are many type of flap mechanism that are largely investigated in [25]. The actuation scheme of the Airbus A340 and its extraction device are depicted in Figure 27 and Figure 28. The central hydraulic power control unit (PCU) supplies the power necessary to deflect the flap panels on each wing. A mechanical transmission shaft transmits the mechanical power to the rotary actuators, which move the flaps on the tracks. This shaft system consists of gearboxes necessary for larger direction changes as well as system torque limiters, wing tip brakes, universal joints, plunging joints and spline joints to accommodate wing bending and temperature effects. The high lift system is controlled and monitored by two slat-flap control computers (SFCC) using sensor information from several analogue and discrete sensors. This type of mechanical transmission shaft system consists of a high number of components with different part numbers and requires high design-engineering and installation effort.

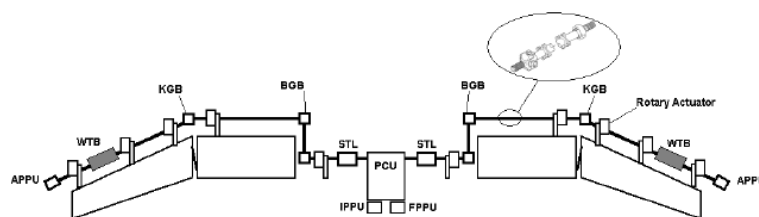


Figure 27 - Global scheme of the inboard and outboard A340 flap actuation system [23]

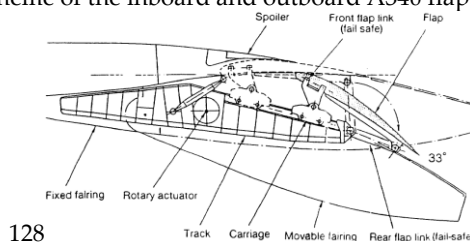


Figure 28 – A340 flap mechanism based on the link/track architecture [25]

In contrast to the previous mechanism, the flap deployment system of the Boeing 767, (Figure 29) is based on a limited number of links in order to create an articulated quadrilateral or more complex hexagonal chain.

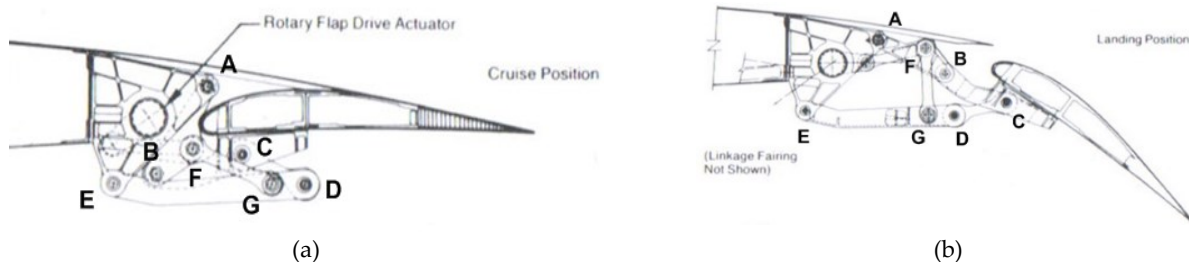


Figure 29 – Boeing 767 flap system: cruise position (a) and landing configuration (b) ([25])

Recent development programs at Airbus and Boeing extend the functional capabilities of the flap systems. The A350 XWB as well as the B787 high lift systems design will incorporate additional functionalities that provide aircraft performance optimization. Additional functionality is achieved with an evolution of the traditional mechanical transmission shaft system and additional active components [26]. The A350's flaps are a very simple "drop-hinge" design with a single slot between the trailing edge of the spoiler and the leading edge of the flap. As the flap extends, the spoilers deflect downwards to control the gap and

optimize the high lift performance of flap. It constitutes a multi-purposes high lift system with augmented functionalities and furthermore it is a lightweight structures thanks to its low complexity link-based kinematic. This can be summarized in the next Figure 30 and Figure 32.

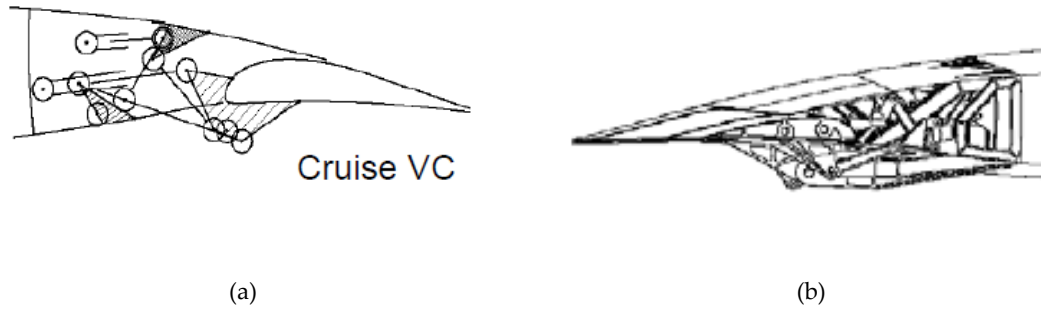


Figure 30 – A350 XWB flap in cruise condition [26]

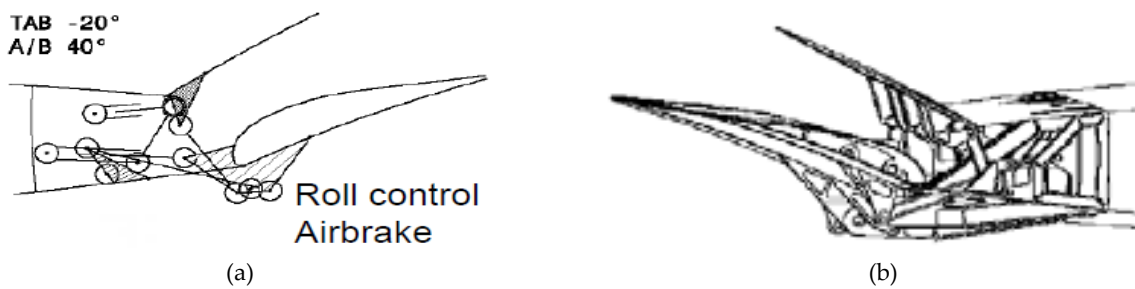


Figure 31 – A350 XWB with A/B and Tab deflection for roll control manoeuvre [26]

Moreover, for the first time, the flap system will have the both the capability for differential inner and outer settings as well as a variable camber function. The design is composed of a gearbox with a motor installed between the outer and inner flap that enables a differential control of the relative angle in order to shift inboard the resultant lift for a less bending moment. Furthermore, both inner and outer flaps can be moved together during the cruise to optimise the wing's camber for each phase of the flight and use the polar of drag to its most efficient configuration [26].

It remains to discuss if, as the complexity level of the actuation mechanism seems to reduce, the promise of morphing aircraft will become feasible within the next few years. If so, how morphing devices will be actuated?

The next technological challenge, envisaged in the context of more or all-electric aircraft, will be to replace the heavy conventional hydraulic actuators with a distributed spanwise arrangement of smaller electromechanical actuators (EMAs). This will bring several benefit at the aircraft level: firstly, fuel savings. Additionally, a full electrical system reduces classical drawbacks of hydraulic systems and overall complexity, yielding also weight (-15% [27]) and maintenance benefits. Lack of supply buses, improved torque control, enhanced efficiency, removal of fluid losses and flammable fluids are only some of the benefits that can be achieved. On the other hand, a general limit of electro-mechanic actuators is the possibility of jamming failures that can lead to critical aircraft failure conditions. Figure 33 shows a practical comparison between the aircraft torque shaft configuration and a distributed actuation arrangement suitable for a morphing trailing edge device.

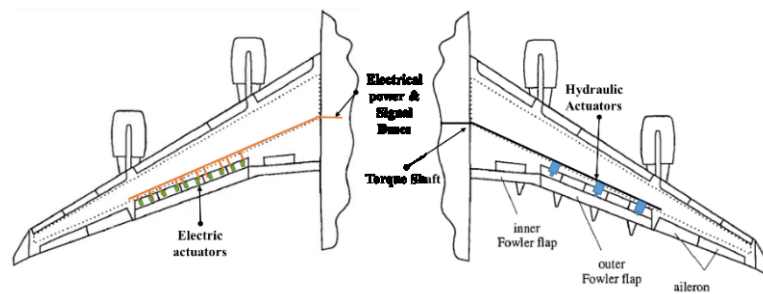


Figure 32 – Distributed concept versus concentrated actuation concept [28]

In the shafted configuration, all actuators are mechanically linked by the torque shaft controlled by the power distribution unit whereas in a distributed arrangement, no more torque shaft is needed. However, the implementation of an electrical system implies many challenges related to the integration at aircraft system level. In particular it must be demonstrated their reliability in harsh environment, moreover their safety and types of failures with an aim to reconfiguration enhancement.

The simultaneous need for monitoring target morphed shapes, actuation forces and flight controls along with the counter-effects of aerodynamic loads under aircraft operating conditions, suggest the use of a ground-based engineering tool for the physical integration of systems. The most suitable to optimize and validate such systems including electromechanical component such as actuators and flight controls is the “Iron Bird”. The basic scheme of an Iron Bird suitable for the integration of different morphing systems is depicted in Figure 33. It includes different morphing devices installed on an aero-elastically reasonable aircraft wing box as well as the basic equipment needed to carry out “hardware in the loop simulations”. Such a concept may be used to demonstrate advanced control technologies in a modular multi-level design that provides the robustness and the flexibility of a real aircraft integration. Manufacturing, assembly and integration issues including electrical and flight control may be extensively addressed in relation to the actual configuration of the aircraft. It is the perfect tool to confirm the characteristics of all system components or to discover an incompatibility that may require modifications during early development stages and thereby it accelerates the transition to test in a relevant environment. Additionally, failures and mitigation actions introduced in the systems can be studied in full detail and recorded for analysis by using such a dedicated testbed.

The morphing wing can be developed and tested in different ways, depending on the time-scale of the integrated concepts. If morphing devices operate in less than a second, they can be reasonably assist in manoeuvring the aircraft. As a result, the control system architecture and related simulations would require considering the A/C model as well as the related flight control actions. If morphing occurs on the order of a few seconds, the adaptive device can be suited for active lift distribution control to maximize L/D during different off-design mission segments, such as climbing and turning flights. If wing shape changes occur on the order of minutes, the aircraft can truly take advantage of the benefits of morphing only during long mission segments, such as cruise, by compensating, for instance, aircraft weight reduction due to the fuel consumption, thus enhancing aircraft aerodynamic performance and aerodynamic efficiency in such limited off-design conditions. In all these cases, a specific control architecture must be designed and physically implemented to facilitate these types of experimental investigations.

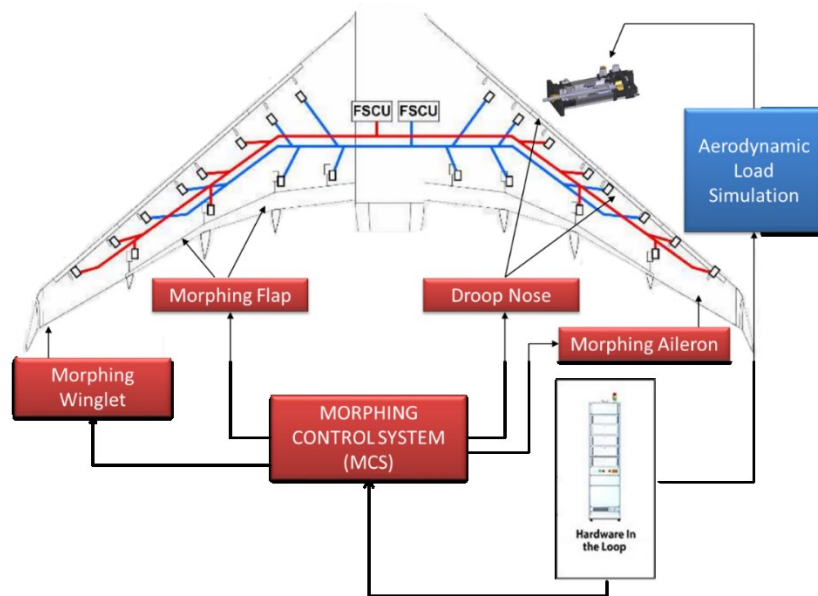


Figure 33 – Representative scheme of an Iron Bird Tool suitable for testing morphing devices

The “Iron Bird” for testing morphing wing architectures enables test engineers to evaluate the real-time capabilities of morphing devices with the purpose of:

- demonstrating maturity, reliability and integrated performance of morphing devices, that otherwise could only be achieved with more expensive costly and less safe methods such as wind tunnel tests or flight tests;
- optimizing morphing wing architecture by testing both compliant and rigid-body mechanism-based morphing concepts and their related actuation, sensor and control systems by monitoring aircraft weight and cost savings;
- investigating aircraft safety-related aspects by simulating system failures, such as jamming, runaways one engine loss, strong cross-wind, aeroelastic effects to validate fault tree analyses and hazard assessments;
- including operational loads that apply hinge moment forces to the aircraft morphing surfaces, representative of the aerodynamics forces applied during the simulated flight test and driven by the flight simulation model;
- detailing cable routing and pathways;
- validating the electrical consumption of each actuation system, in stationary and dynamic conditions, and the required command to A/C surface in each test case.

In the state of art of actuation mechanism for morphing application, can be found many design properly tailored to allow the structure to reach the target shape within imposed constraint such as available room and loads. SMA, PMA, kinematic and magneto-rheological fluid based system are example of smart device for morphing structures. Starting from SMA, it is noticeable that implementing this material within structural elements could bring benefit in terms of weight, compactness and reliability however they are still in a study phase regarding the implementation in a commercial context. The main limit of these innovative materials dwell to the limited applied force/applied rate ratio, thus circumscribing research to small aircraft model. Kudva & al ([29]-[31]) have worked on SMA actuation concept for morphing wing realizing the most interesting application. The developed architectures were implemented in the DARPA “Smart Wing” program with focus on wing torsion by SMA torsional tube and wing camber variation (both LE and TE) by means of SMA wires. As shown in Figure 34, the wing twist can be achieved using two

concentric SMA tubes subjected to a relative rotation. Moreover, SMA wires are used in an antagonistic manner in order to morph the trailing edge upwards and downwards, creating a hinge-less control surface.

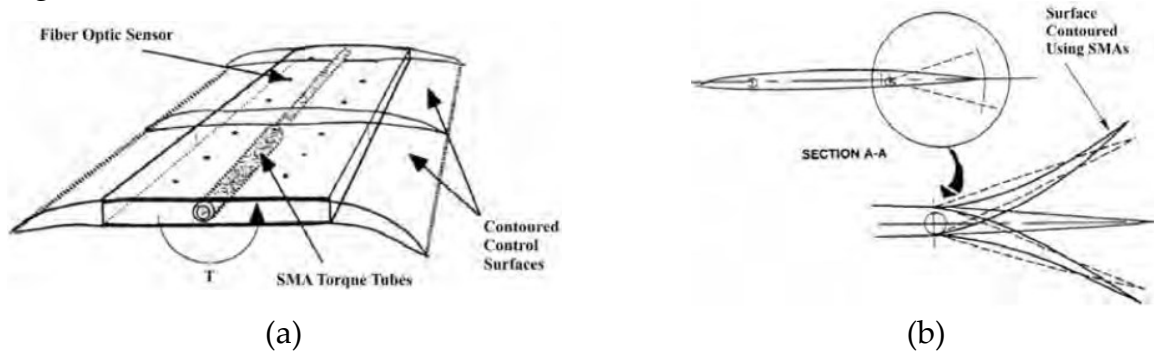


Figure 34 – Smart Wing program: (a) Wing twist by SMA torsional tube, (b) TE deflection actuated with SMA wires [29]-[31]

The detail of the trailing edge SMA wires is below reported (Figure 35), where it is shown that the SMA cables work in antagonistic configuration in order to have a better efficiency under static load.

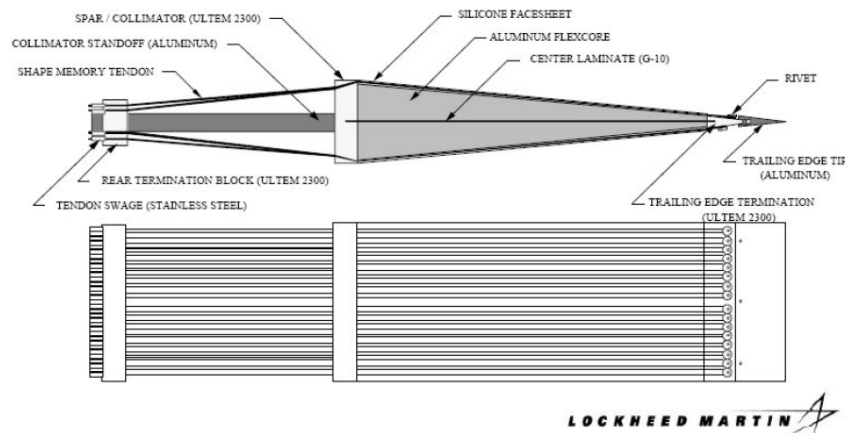


Figure 35 – Detail on the trailing edge SMA based mechanism [29]-[31]

The program is aimed at the realization of an UCAV experimentally studied with both described mechanism. The vehicle design are reported in Figure 46.



Figure 36 – UCAV concept developed in Smart Wing project [29]-[31]

Another, more recent, SMA application are described in the paper [32]. An actuator device based on Shape Memory Alloys is studied. It consists of a metallic arch, working as a spring, being driven by an SMA ribbon, contracting and relaxing. Upon thermal activation of the SMA element, the arch shrinks and its free end rotates, producing the desired structural deformation. This actuator is also able to sustain external loads and have cyclic actuation,

by means of the elastic recall, due to the arch itself. The arch with SMA is shown in moreover the actuation mechanism has been fully assembled on a flap portion for experimental tests and validation (Figure 37).

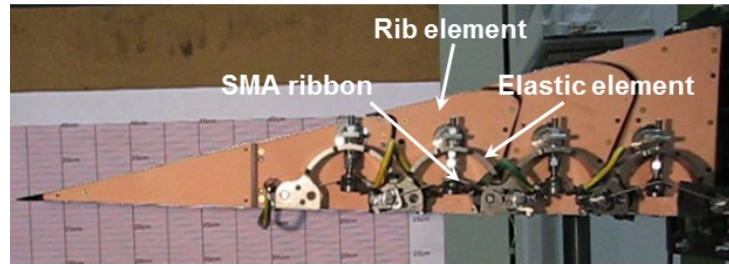


Figure 37 – Integration among the SMA concept on a flap prototype [32]

For morphing aerospace application, the authors in [33], demonstrated the feasibility of PMA from control authority and fatigue life point of view. In particular, PMA were used to deflect the trailing edge flap for a generic wing of a rotor blade. The system worked both in low frequency and up to 40 Hz and can provide more than 120 million of cycles under load. The pneumatic artificial muscle (Figure 38), works as an actuator that generate tensile force along their longitudinal axis when inflated with an high force-to-weight ratio.



Figure 38 – PMA in uninflated and inflated configuration [33]

The application described consist of deflecting (up to 40 Hz) of a flap trailing edge for flight and vibration control particularly suited for UAV application such as rotors or control surfaces (Figure 39).



Figure 39 – Wind Tunnel prototype of a flap equipped with PMA: (a) inner view, (b) with flap deflected [33]

The application of the PAM need further development in terms of control and certification. An important example that show the importance of actuation system in a distributed arrangement for morphing application is the NextGen aeronautic wing ([34]-[36]) capable

of being transformed from high-span configuration for low speed to a configuration with reduced span for flying at high speed (Figure 40).

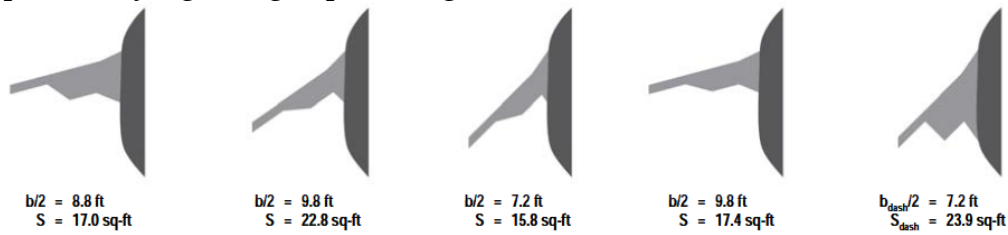


Figure 40 – Morphing Wing adaptation to the various flight condition: high lift, cruise, loiter and manoeuvres [34]-[36].

The wing can achieve large geometry modification including 200% change in aspect ratio, 40% in span and 70% in wing area. The entire project innovation include:

- independent control for wing sweep and wing area
- innovative flexible skin with low-in plane stiffness and high flexural stiffness for withstanding external loads;
- multiple and distributed internal actuators centrally controlled for achieve the target morphing geometry and,
- internally robust kinematic wing structures in a truss-like architectures (Figure 41).

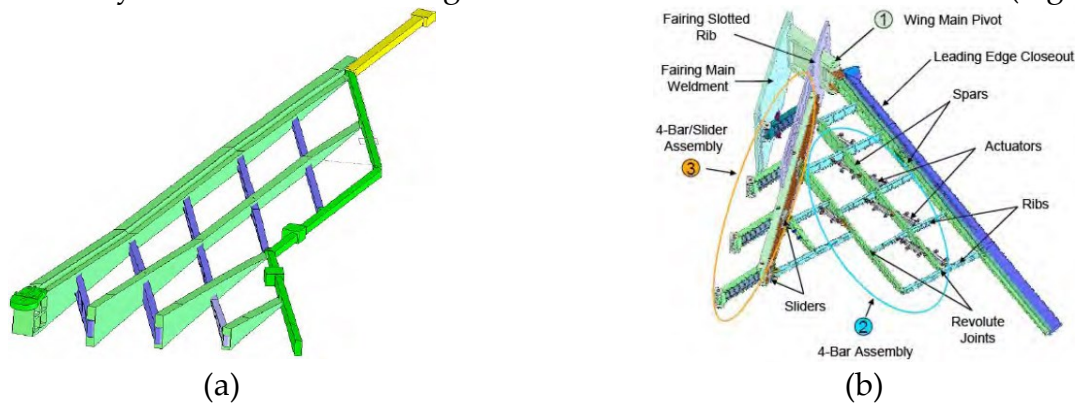


Figure 41 – NextGen wing design [35]

The distributed actuation concept herein presented is really suited for application with limited available space such as a thin wing or control surfaces such as aileron where the external load is sustained by smaller actuators rather than fewer but bigger. In fact the eccentric beam actuator (EBEAM), firstly developed in the DARPA project ([36]) constitute a promising solution for actuate morphing device with restricted volume as reported in Figure 52 ([37]). The main component is a bent beam connected to a rotary actuator shaft that push its extremity upwards or downwards. The movement is then transmitted to the structures by means of discs located in correspondence of skin stringer which provide a surface along with the disc can slide acting like a rail.

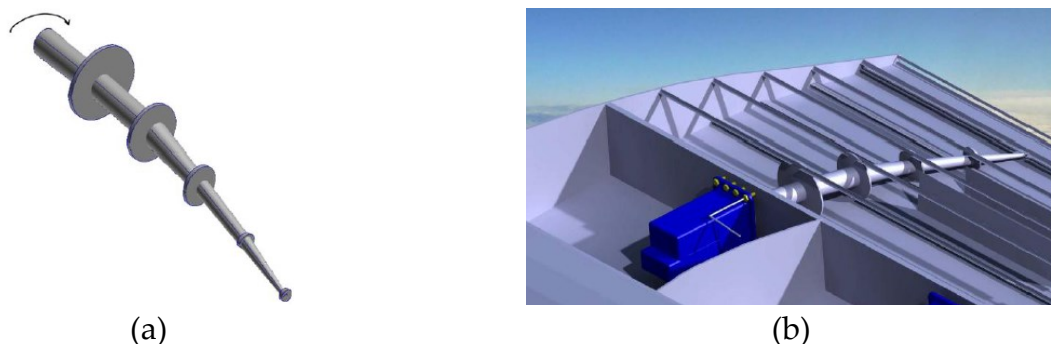


Figure 42 – EBEAM concept (a) and its implementation on an aircraft control surface (b) [37].

Moreover it is evident that the beam camber is defined on the base of the target morphed shapes to be achieved and its diameter decrease from the rear spar of the flap to its trailing edge in order to fit in smaller space. The authors in [37] propose to connect all the beams by means of an output shaft that transmit the torque of a unique actuator, moreover it is also possible to individually drive the beam by single actuators equally distributed (one per beam). In Figure 43 is shown the distributed arrangement of the actuation concept slightly adapted on the base of the investigated solution.

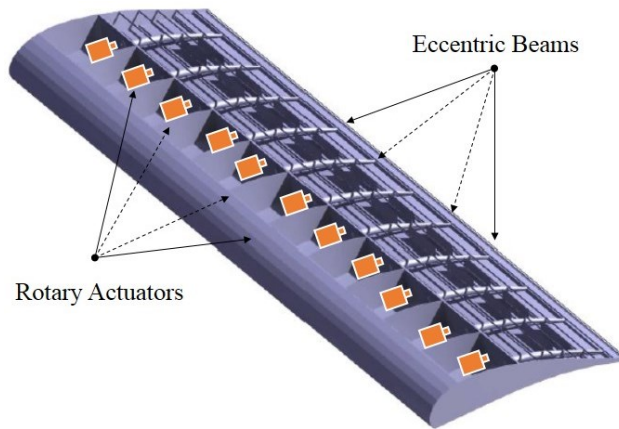


Figure 43 – Distributed concept of the Eccentric Beam based actuation concept

The morphing actuation system requires a deep knowledge on kinematic with the aim to design a mechanism able to withstand higher external loads with less power due to consistent mechanical advantage (MA). This objective can be reached by implementing a distributed configuration, as already mentioned, and with a dedicated kinematic chain. One promising architecture is based on the oscillating glyph mechanism that will be further carefully described in this thesis. This concept has been investigated in [19] and herein summarized. In order to achieve very high transmission ratio, it is crucial to optimize the geometric characteristic of the components since from the first design phase. The actuation mechanism is driven by a load-bearing actuator that transmit its rotation to a crank directly linked to a sliding element that generate a force along a rail. The system is connected to an actuation lever that in turn drives the segmented rib as shown in Figure 44.

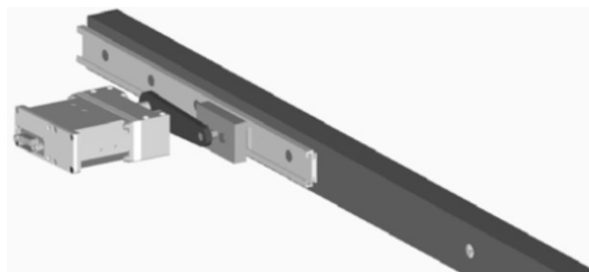


Figure 44 – Actuation system based in quick-return mechanism [19]

Shape-changing wing requires actuators attached to internal mechanisms, covered with flexible or a sliding aerodynamic surfaces - with load transfer attachments between skin and internal structures. This requires a distributed array of actuators, mechanisms and materials that slide relative to each other or skin materials that stretch. The main mechanism design requirements include the range of motion and concerns about binding and friction as well as the effects of wing structural deformability under load and the control of the actuator

stroke under loads. Morphing poses several unique challenges when the wing loading is high. Very flexible materials are the designer's first choice because they are easily reshaped. However, the wing structure must have high bending stiffness, with in-plane compliance to allow actuators to change area with low energy input. Actuator performance power and actuator force capability are essential to design success. The size, weight and volume of the actuators are an important metric, as is range of motion, bandwidth and fail safe behavior. Locking is important when the wing is under load since, without locking features, the actuators must withstand full operative load. Also the material selection and suitability become a particularly important challenges. Multi-functional skin stiffness, as already described, is important, but so too is joining and interface compatibility and the ability to seal openings as the wing transitions from one form to another. A fledging technology to this job may be shape memory polymers. These polymers have two phases, each with a different modulus. When heated, the polymer will assume one shape with low stiffness and can be easily deformed by actuators. At a lower temperature, a second component shape is appears with a larger elastic modulus. These skins must provide a seamless airfoil shape and keep structural integrity under compression, tension, bending and flight loads throughout morphing transitions, but they are ideal for filling gaps created by large motions of surface areas. Wing morphing remains a promising technology, because it allows to explore more aerodynamic performance of the aircraft by adapting to all the flight conditions encountered during a typical mission. New design criteria must be adopted for a wing morphing even if they are totally far from the conventional ones both for compliant or rigid mechanism in order to reach the objective addressed by NASA that it takes other 20-30 years for develop a flying full morphing aircraft with smooth continuous control surfaces Figure 45.



Figure 45 – Artistic Concept of the NASA idea of a morphing aircraft [38]

2. CRIAQ Project and the adaptive aileron

Following the enthusiastic results, achieved with the Adaptive Trailing Edge Device, the Italian team aimed at facing a new challenge. The former configuration did in fact refer to the standard position of the flap, leaving apart the aileron region. There are several reasons to leave that part unchanged. The most relevant may be associated to the fact that the aileron has a critical function in the aircraft flight and its collapse could lead to dramatic failures. The investigated configuration would have lied over an extended region of the aileron instead than a limited part, as in the case of a flap, characterised by a larger chord. As a direct consequence, the available volumes are reduced and the installation of integrated actuators could have been a problem. Finally, the aeroelastic response of the device is critical as well and its strong modification should have been deeply studied. On the other hand, the studies on the ATED showed as the regions, farer from the root, gave a more significant contribution to the aerodynamic behaviour. So, it was really interesting to investigate the possibility to extend the adaptive trailing edge technology to the aileron region. The occasion was given by a joint Italian/Canadian research activity fostered by the Consortium de Recherche et d'Innovation en Aérospatiale au Québec (CRIAQ). The activity aimed at realising a full-scale demonstrator of a wing section in the tip region for investigating the capability of wing box and trailing edge morphing devices, to ensure a certain level of flow control and aerodynamic performance variations, respectively. The first issue was in charge of the Canadian team (ETS, NRC, Thales Aerospace, Bombardier AS), while the Italian group (University of Napoli and CIRA), aimed at realising a device for the aileron camber control. The enlisted problems were all evident at the very first approach. Volume limitations forced the designers to follow a different strategy. Instead of having a couple of actuators acting on each rib, the architectural layout was specialised per each single bay. At the aileron root this possibility was maintained, while the more external two bays were commanded by a single actuator. In other words, the last two segments were made of two slave and a master ribs, driven by a single actuator. Calculation showed as this configuration was able to maintain the specified loads. Aeroelastic studies confirmed the reliability of the device, in sense that the selected architecture was demonstrated to be safe in the design flight conditions. The adaptive aileron finally maintained the original capability while ensuring morphing characteristics. This target was accomplished by realising a device with two separate motor systems. The first, acting on the main aileron shaft, to preserve its characteristic dynamic response for flight control. The second, acting on the rib, implemented the searched camber variations to follow the aerodynamic necessities related to fuel consumption. Another relevant point concerns the skin. In order to check the possibility of skipping the needs of implementing a compliant solution, a heavy and sophisticated element, the single hinged blocks were properly shaped to slide one into the other, like a meniscus. This solution was however strongly correlated to the manufacture tolerances and the assembly precision, because small deviations could have had a significant impact on the kinematic performance. As usual, vantages and disadvantages try to compensate each other. The partners involved are shown in Figure 46. The main objective of the teams working on the international project is to design and manufacture a morphing full-scale wing tip for a Bombardier-type aircraft controlled by electric actuators and pressure sensors. The complete title of the project is *Morphing Architectures and related Technologies to improve the Wings Efficiency*.



Figure 46 - Partners involved in the CRIAQ MDO505 project

The objectives of the desired morphing behavior are to delay the flow transition promoting large laminar flow run and prevent massive boundary layer separation by turbulent reattachment and to regain the aileron efficiency. The aerodynamic numerical results will be validated using wind tunnel tests in the NRC Subsonic Wind Tunnel. Main targets, defined by Bombardier, to improve regional aircraft performance, are:

- Development of suitable morphing technologies for the aileron region
- Implementation of the design strategies devoted to morphing philosophy
- Assessment of an integrated morphing control system for real-time control
- Verification of functionalities by targeted tests, both in lab and WT environment

The program addresses the fulfillment of combined smart structures specifically conceived to optimize the aerodynamic efficiency. The basic idea is to combine the effect of two morphing technologies devoted to aircraft wing; an adaptive-bump for the upper skin of the wing box to control the transition point from laminar to turbulent flow in conjunction with a variable camber aileron architecture in order to minimize drag coefficient & maximize lift coefficient in off-design conditions. In Figure 47 a schematic real-like wing model is depicted. The wing is equipped with a flexible composite skin on the upper surface of the dry area between front and rear spars, which is morphed by a set of actuators contained into the wing box and a morphing aileron.

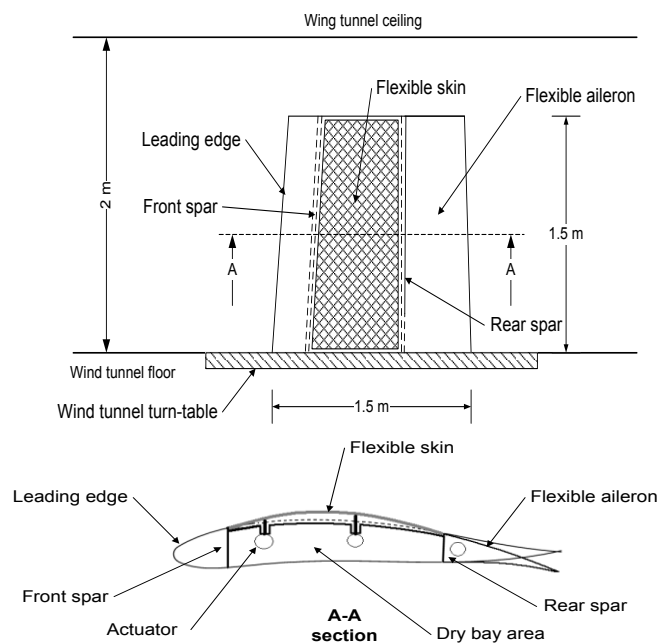


Figure 47 – Wing box - Aileron demonstrator

The CRIAQ project is articulated in three main Work-Packages (WP) each one divided in Tasks (T) and Subtasks (ST) in turn. The WP titles are reported in Table 1.

WP	TITLE
1	Definition of target shapes for wing morphing
2	Definition of morphable structures
3	Manufacturing and tests of technological demonstrators

Table 1 – CRIAQ project WP titles

Referring to the Table 2, University of Naples “Federico II” is responsible of WP-2 and CIRA was involved in the Task 2.2 regarding the design and validation of the aileron actuation system and control laws useful to enable the trailing edge morphing. In this project, Italian team are properly responsible only on the aileron part which has been designed on the base of accurate interface requirements imposed by the Canadian device. In such manner the aileron will perfectly match with the wing-box during installation in the wind test chamber.

WPP 1	T 1.1	Analysis of baseline A/C configuration and definition of design requirements	ST 1.1.1	Generation of A/C aerodynamic model
			ST 1.1.2	Evaluation of baseline wing efficiency in reference to a typical flight profile
	T 1.2	Morphing shapes for the skin of the wing box	ST 1.2.1	Sensitivity analysis of wing box skin shapes for wing efficiency optimization
			ST 1.2.2	Individuation of optimal target shape for each condition of flight profile
	T 1.3	Morphing shapes for wing trailing edge	ST 1.3.1	Sensitivity analysis of trailing edge shapes for wing efficiency optimization
ST 1.3.2			Individuation of optimal target shape for each condition of flight profile	
T 1.4	Analysis of morphing solutions combined effects on wing efficiency			
WPP 2	T 2.1	Definition of compliant architecture for wing box skin morphing	ST 2.1.1	Preliminary sizing of morphing structure for wing box skin morphing
			ST 2.1.2	Individuation of actuators and definition of control laws useful to enable wing box skin morphing
			ST 2.1.3	Design assesment of morphing architecture (structure+actuators) by means of advanced numerical simulations
			ST 2.1.4	Executive drawings emission
	T 2.2	Definition of compliant architecture for trailing edge morphing	ST 2.2.1	Preliminary sizing of morphing structure for trailing edge morphing
			ST 2.2.2	Individuation of actuators and definition of control laws useful to enable trailing edge morphing
			ST 2.2.3	Design assesment of morphing architecture (structure+actuators) by means of advanced numerical simulations
			ST 2.2.4	Executive drawings emission
WPP 3	T 3.1	Manufacturing and tests of morphing architectures for wing box skin morphing	ST 3.1.1	Manufacturing of two technological demonstrators for the architecture related to wing box skin morphing
			ST 3.1.2	Static tests
			ST 3.1.3	Wind tunnel tests
	T 3.2	Manufacturing and tests of morphing architectures for trailing edge morphing	ST 3.2.1	Manufacturing of two technological demonstrators for the architecture related to trailing edge morphing
			ST 3.2.2	Static tests
			ST 3.2.3	Wind tunnel tests
T 3.3	Test of coupled morphing architectures	ST 3.3.1	Integration of T3.1 and T3.2 architectures in a unique test article	
		ST 3.3.2	Wind tunnel tests on T3.1 and T3.2 architectures assembly	

Table 2 – Work-packages, tasks and sub-task of the CRIAQ project.

3. Morphing Aileron Design

3.1 Description of the model

3.1.1 Wing model characteristic

The wing model object of the present study is representative of a full-scale tip of a transport regional aircraft. The aim of the first work-package, for the Canadian team, was the preliminary sizing of the morphing wing-box skin, then the design assessment of morphing architecture. At the end of this task, the Canadian team developed a detailed digital mock-up of the morphing architecture that it will be analysed below. Detailed views of the wing box CAD assembly are reported in Figure 48 and Figure 49; it can be seen the internal structure and the bumps' actuators. The wing model, equipped with the ATR airfoil, has a chord 1.5m long and a span 1.5m long. It has an internal structure similar to the ATR-42 wing tip including the aileron. The structural architecture is made up of: four span-wise ribs, a front spar, a rear spar, an upper flexible skin, a lower skin with stringers, four actuators to control the adaptive bump configuration, and two hinge blocks to link the morphing aileron. The upper skin is made of composite, the internal leading edge of foam, and all the other items are made of aluminium Al 2024- T351.



Figure 48 – T/A isometric view

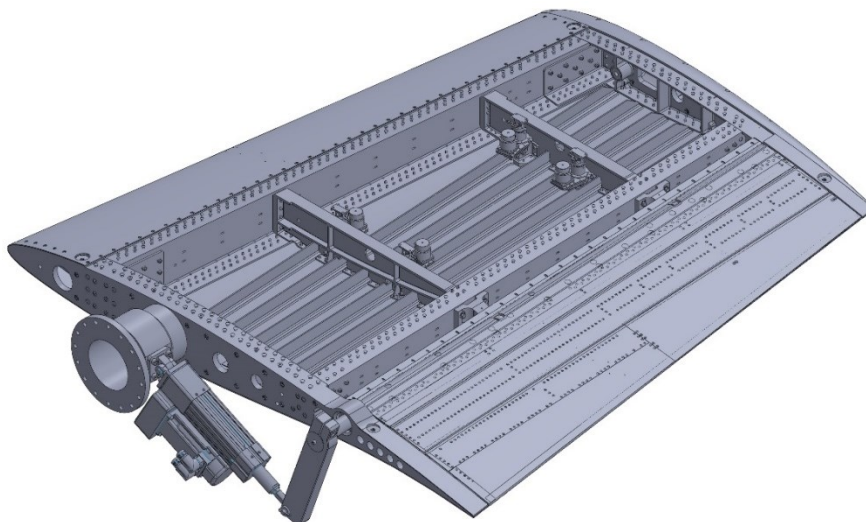


Figure 49 – T/A isometric view with detail on the internal wing box

Aileron rotation around its main hinge axis is assured by a linear actuator connected to a stiff cylindrical support holding the entire T/A and in turn constrained to the wind tunnel by means of bolts. The entire wing will be vertically mounted in the wind tunnel with the

actuator positioned under the tests chamber floor so it will be exposed to the flow (Figure 50). The complete test article geometrical characteristic are summarized in Table 3.

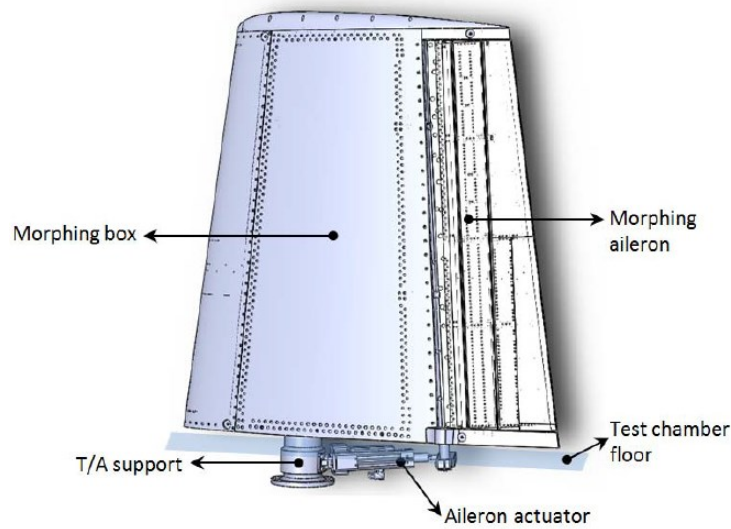


Figure 50 – T/A assembly

Geometrical Data	
Span	1.5 meters
Root Chord	1.5 meters
Tip Chord	1.075 meters
Taper-Ratio	0.717

Table 3 – T/A geometrical parameters

Moreover in the next Table 4, are reported the wing box materials.

MATERIAL (ISOTROPIC)	E [GPa]	ρ [Kg/m ³]	ν	REFERENCE ITEM		
Harmonic Steel	210	7850	0.30	T/A support, hinge block, lever arm of the external actuator		
Al2024-T351	70	2768	0.33	All wing box items (with the exception of the upper skin)		
Fiberglass Renshape 5020	9.40	160.18	0.22	Leading edge core		
MATERIAL (ORTHOTROPIC)	E1 [GPa]	E2 [GPa]	G12 [GPa]	ρ [Kg/m ³]	t [mm]	REFERECE ITEM
Ply type a	64.8	65.6	5.64	1600	0.074	Upper skin panel
Ply type b	133	9.65	5.51	1600	0.317	
Laminate*	63.7	49.9	16.5	1600	0.269	

*Layup ((0/+45/90/-45/0)₂+(0/+45₂/90₂/-45/0)+0)_s
 REMARK: ply type b used only in first and last position of the stacking sequence.

Table 4 – Wing box adopted materials

In the next Figure 51, it is reported a graphic representation of the morphing aileron during a deflection, installed on wing tip.

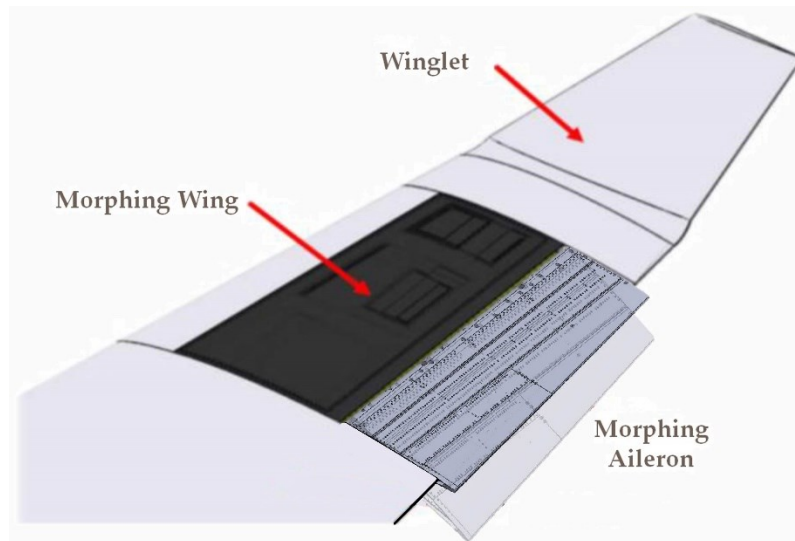


Figure 51 – Schematic representation of the morphing aileron on a real wing [41].

3.1.2 Aileron design

It is widely evident, by the studies described in the introduction, the impact that morphing structures could bring to the future aircraft that will become more important with the development of new technologies to be implemented into the design. The results obtained from Clean Sky multifunctional flap and from the SARISTU trailing edge, showed a mature technologies for industrial application which lead to the interest of demonstrating its feasibility also in the aileron region. This is a very delicate zone, where aeroelastic phenomena may be very important following the very reduced local structural stiffness and the complex aerodynamic, usually associate to the wingtip zone. In a morphing aircraft, the wing parameters such as the chord length, span and wing camber are modified to form the multiple optimal shapes. These large scale structural changes or morphing, in flight, have a significant impact on the dynamics and aeroelastic characteristics of the wing. On the other side, this zone showed as the one where the aforementioned device seemed to exhibit the higher performance. The general architecture resembles the same philosophy developed for the flap. A further device is added to an original aileron system. It is aimed at working in cruise, by means of symmetric deflection, to modify a limited chord segment of the aileron, so to accomplish the aircraft weight variations following fuel consumption and to reduce drag in off-design conditions. However, during classical manoeuvre, this morphing, no-gap part is rigid and the aileron works in the usual manner. The system is therefore made of two motor systems, one devoted to manoeuvre and other classical aileron employments, while the other is devoted to the implementation of morphing. Such a morphing device wants to augment the former device expanding the hosting wing region by adapting local wing camber shape and lift distribution through a quasi-static deflection its excursion ranging into few unit of degrees, positive and negative. However, its aerodynamic benefits are very sensitive to the actual wing shapes achieved during the aircraft mission. ETS (École de technologie supérieure du Montreal) provided text files containing z/c vs. x/c airfoil coordinates with reference to different airfoil settings. Each file has been named by ETS according to the airfoil setting it refers. Investigated settings resulted in combination of Mach numbers, wing AOA (α) and aileron deflection (δ). Each shapes comes from

aerodynamic studies aimed at identify the optimal airfoil configuration which delay transition from laminar to turbulent flow using in conjunction both thickness bump and trailing edge camber variation. In the following Table 5, the considered settings are shown:

Mach	α [°]	δ [°]
0.1; 0.3	-2; 0; 3	-7; 0; 7

Table 5 – Optimized airfoil shape settings

The input airfoil shapes provided by ETS have been plotted for each configuration reported in the previous Table 5.

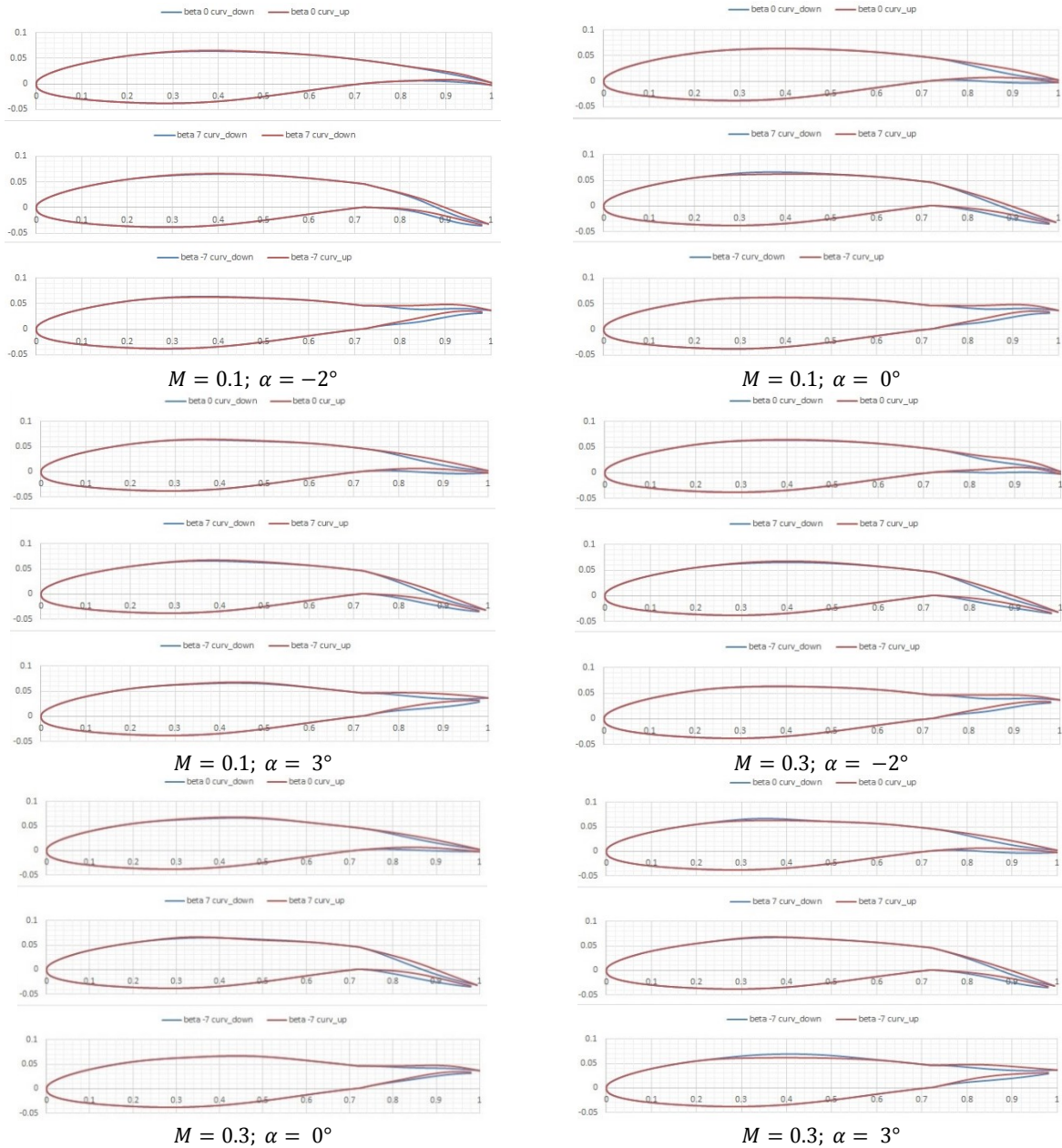


Figure 52 – Airfoil target shapes

Plotting the “iso-alpha” shapes (Figure 53) it is evident that for each value of AOA, the Mach number does not have much influence on the aileron region ($x/c \geq 0.72$).

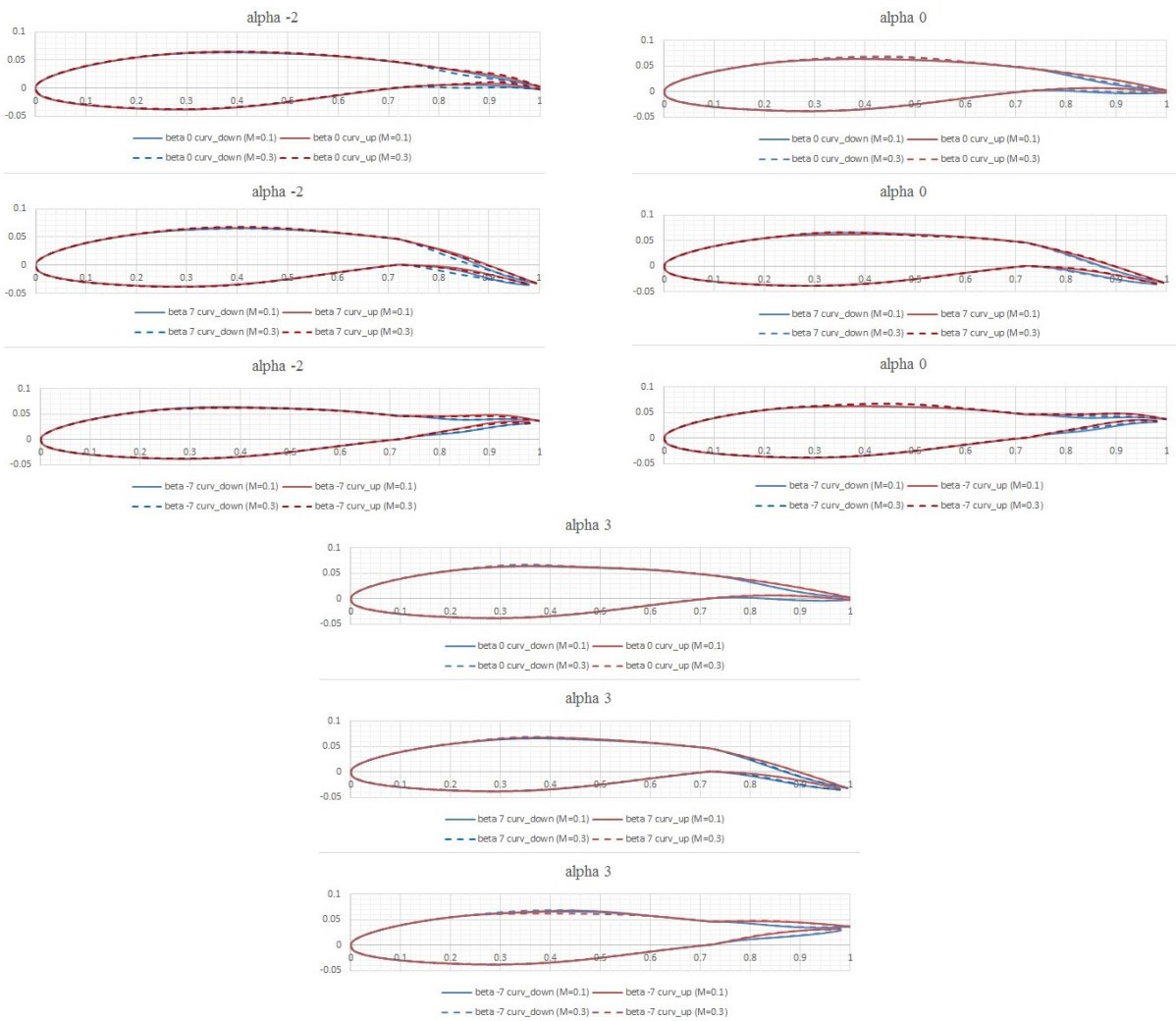
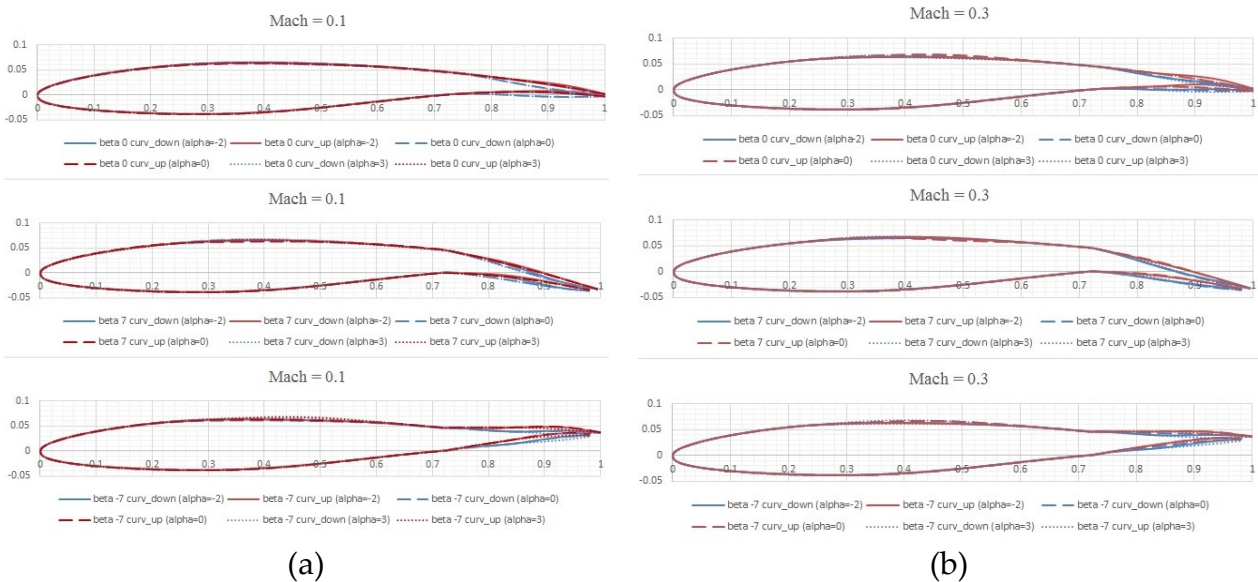


Figure 53 – “Iso-alpha” aileron shapes

Furthermore, from the comparison among the “iso-mach” curves (Figure 54), resulted that different values of AOA leads to different aileron shapes.



(a)

(b)

Figure 54 – “Iso-mach” aileron shapes

The difference are not negligible and they are reported in Figure 55 where a zooming of the airfoil geometry was carried out.

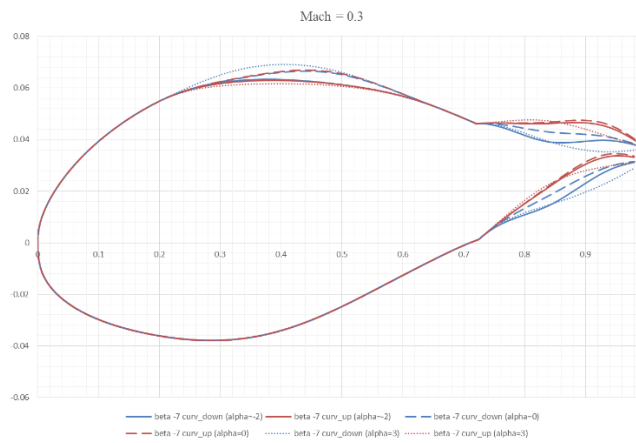


Figure 55 – Zooming of the different shape for different AOA

The aileron target shapes have to be feasible in compliance with aeronautical standards and the capability to withstand high loads. In light of such considerations, some set of the provided shapes have been discharged. In detail:

- All the morphed shapes leading to a change in the sign of the slope of the aileron camber. It is not possible to morph according to an S-shape camber.
- All the shapes leading to a null deflection at the aileron tip (all the ETS shapes for $\beta=0^\circ$ as reported in Figure 56). The morphing can be implemented only with a finite displacement of the aileron tip.
- All the morphed shapes at different angle of attack.

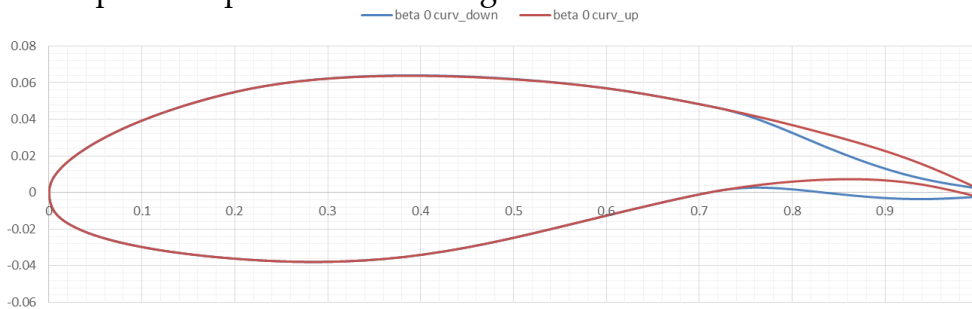


Figure 56 – Aileron shapes for null tip deflection

The final target shapes have been then selected and refined by Unina in order to avoid sharp airfoil boundary at the transition from the wing box and the aileron region furthermore; since no reference morphed shape was selected for the case of $\beta = -7^\circ$, they were generated by Unina in order to avoid further optimization loop for Canadian team. The final target shape are depicted below in Figure 57, in the range of aileron deflection $[-7^\circ/+7^\circ]$.

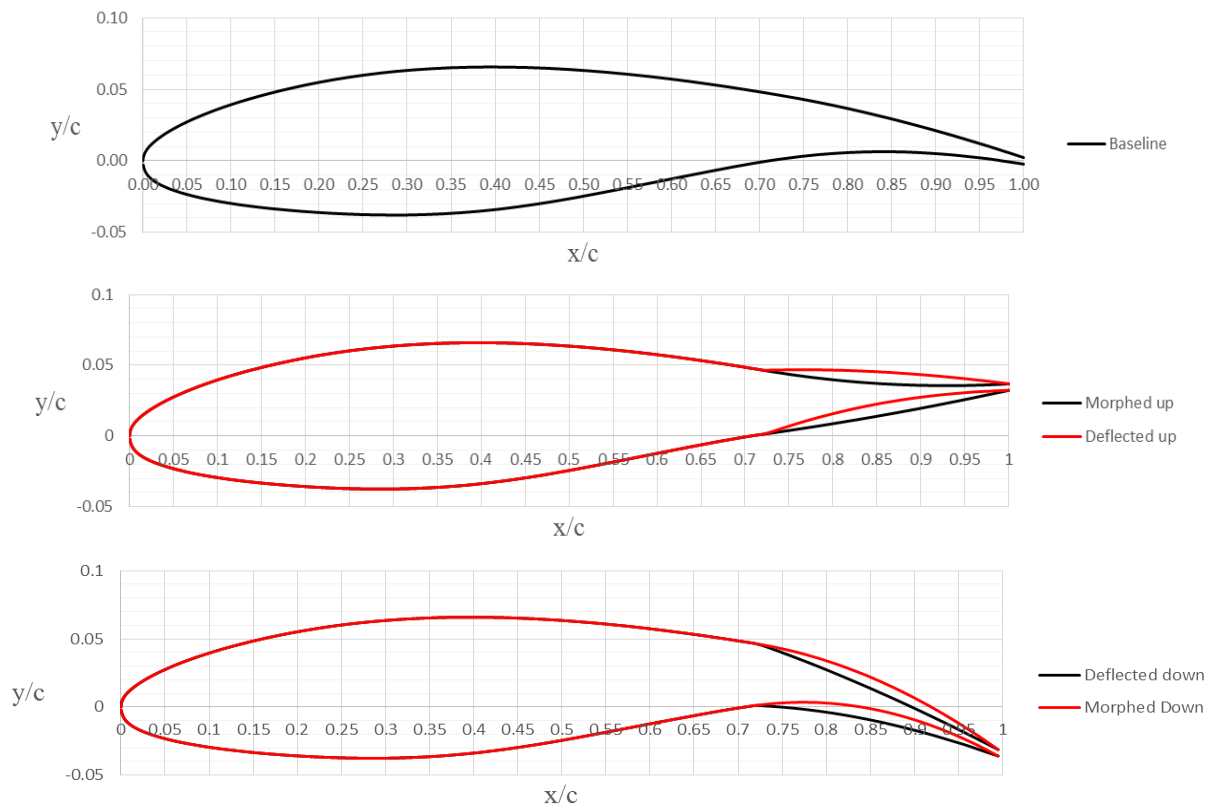


Figure 57 - Final selected aileron morphed shapes

In particular:

1. The target morphed shapes for the morphed down aileron will be the one refined by the Italian team on the base of selected Canadian shape
2. The target morphed shapes for the morphed up aileron will be the one defined by the Italian since all the ones coming from Canadian team are un-practicable from the structural point of view (on the base of our technology)
3. The C_p distribution to get the design load will be the one pertaining to the refined morphed shape of point 1. Such distribution has been evaluated by Italian team (through VLM) and envelopes all the C_p distributions provided by the Canadian team. It is natural, that our structure will allow for several tip deflections in the range of beta $[-7, 7]$; all these shapes will however preserve smooth camber variation (with no change in slope sign) for the aileron region.

The geometrical external contour of the aileron herein defined, constitute the first step for its ribs structural design; in fact to enable the transition from the aileron sections from the reference (baseline) to the target shapes, a morphing structural concept was developed by University of Naples. Each aileron articulated ribs was assumed to be segmented into four consecutive blocks (B0, B1 and B2) connected to each other by means of hinges displayed on the airfoil camber line (A and B) in a “finger-like” configuration. Moreover, non-consecutive rib plates are connected by mean of a link (L) that forces the camber line segments to rotate according to specific gear ratio. The geometric definition of the plates is designed such that the camber is a polynomial law.

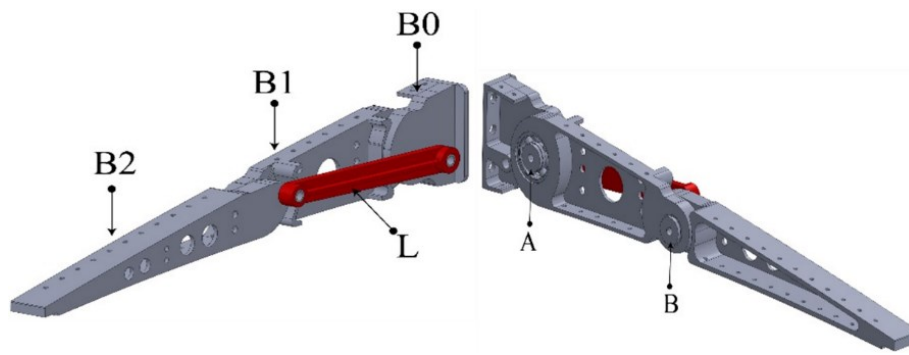


Figure 58 - Morphing rib architecture with blocks and links and hinges.

The linking element (L) makes each rib equivalent to a single-DOF mechanism: if the rotation of any of the blocks is prevented, no change in camber/shape can be obtained; on the other hand, if an actuator moves any of the blocks, all the other blocks follow the movement accordingly. The rib mechanism uses therefore a three segment polygonal line to approximate the camber of the airfoil and to morph it into the desired configuration while keeping approximately unchanged the airfoil thickness distribution. The ribs' kinematic was transferred to the overall aileron structure by means of a *multi-box* arrangement (Figure 59). In Figure 60, the aileron is depicted in both morphed up and morphed down configurations.

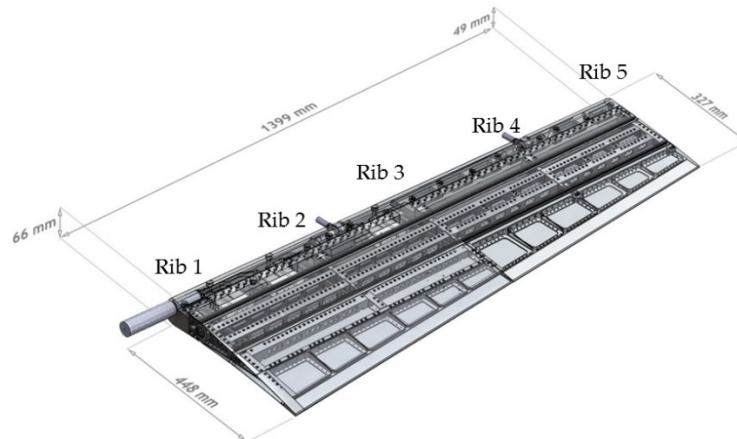


Figure 59 - Morphing aileron structure: multi-box arrangement

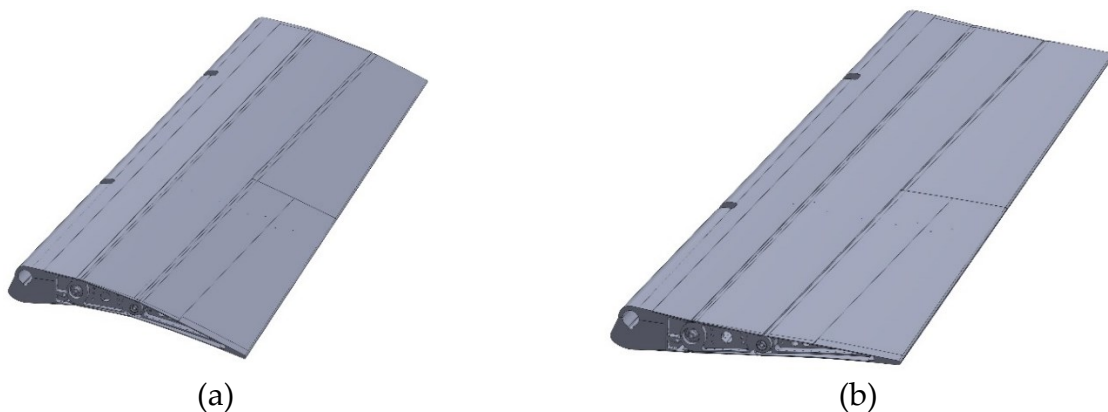


Figure 60 - Dimetric view of the aileron morphed shapes

Each box of the structural arrangement is characterized by a single-cell configuration delimited along the span by homologue blocks of consecutive ribs, and along the chord by longitudinal stiffening elements (spars and/or stringers). Upon the actuation of the ribs, all the boxes are put in movement thus changing the external shape of the aileron; if the shape change of each rib is prevented by locking the actuation chain, the multi-box structure is

elastically stable under the action of external aerodynamic loads. A four-bay (five-ribs) layout was considered for an overall (true-scale) span of 1.4 meters; AL2024-T351 alloy was used for spars, stringers and rib plates, while C50 steel was used for ribs' links. Off-the-shelf airworthy components were properly selected for the bearing and bushings at the hinges and coupled to torsional springs to recover any potential free-play. A multi-module skin was considered in conformity to the multi-box segmentation; three aluminium-alloy panels were then adopted, each panel sliding over the consecutive one in an armadillo-like configuration. Airflow leakage at the skin segments interfaces was prevented through low-friction silicone seals. As one might expect, the segmented skin architecture does not significantly impact the aileron torsional stiffness and resulted slightly higher (but on the same order) of a conventional aileron. The deployment kinematics use a "direct-drive" actuation based on actuation arm that is rigidly connected to the B2 block in Figure 58. This arm rotates the 1-DOF-based mechanical system and transmits the actuation torque from the actuator to the adaptive rib. The control actions aim at producing small camber variation in the adaptive aileron corresponding to a rigid rotation of a plain control surface comprised between -7° and $+7^\circ$ during flight. In specific, a self-contained morphing device, made of links, hinges and joints to alter the inner geometry, is developed with the purpose of providing a standard hinged control surface with an added functionality which may improve aircraft off-design points, such as cruise or climbing. However, similarly to any promising technology to be integrated in aircraft, an accurate estimation of its weight loss or weight gain becomes crucial with respect to the conventional configuration. To date, this benefit can be only grossly computed or preliminarily assessed. On the one hand, according to Breguet's formulas, aircraft range strictly depends on aircraft aerodynamic efficiency and the ratio between the maximum take-off weight and the burned fuel weight. On the other hand, it is evident that the benefits associated with morphing shall be high enough to compensate the drawbacks coming from possible weight penalties. Therefore, in order to gain competitive advantages through morphing devices, it is necessary that:

$$\Delta W_{fuel}^E > \Delta W_{fuel}^{M_{TOW}} \quad (1)$$

Where ΔW_{fuel}^E indicates the saved fuel weight percentage due to the incremented aerodynamic efficiency for the effect of the morphing device. In addition, $\Delta W_{fuel}^{M_{TOW}}$, represents the overall aircraft structural weight penalty due to the use of the morphing aileron. The weight of the morphing aileron designed for a 78-seat aircraft was about 25 kg. Being the aircraft maximum weight around 20 tons, it comes up that the morphing aileron is only 5‰ of the entire aircraft weight. It results than obvious that the weight penalty could be easily compensated by the fuel savings ensured by such a morphing technology (from 3% to 6% [39]). From the manufacturing standpoint, the developed concept consists of many standard pieces and requires careful assembly procedures to support operators. This may

affect its industrial applicability. Efforts are currently pursued to simplify the design using topology optimization methodologies reducing the number of parts.



Figure 61 – Aileron digital mock-up: (a) transparent skin and (b) covered skin

A multi-module skin was considered in conformity to the multi-box segmentation; three aluminium-alloy panels were then adopted, each panel sliding over the consecutive one in an “armadillo-like” configuration Figure 61. Airflow leakage at the skin segments interfaces was prevented through low-friction silicone seals.

3.2 Design Loads

VLM method was adopted to evaluate aerodynamic pressure distribution along the aileron in correspondence of each considered flight attitude (namely wing angle of attack, flight altitude and speed) and aileron geometrical configuration. 3D flat-panels mesh was generated in correspondence of the outer wing segment; the mesh was constituted by 6 macro-panels (Figure 62) respectively representative of the outer wing root and tip portions (panels P1 and P3), of the wing box including wing leading edge (panel P2) and of the three aileron’s segments (panels P4, P5 and P6). Each panel was further subdivided in a convenient number of boxes. For each flight attitude and aileron shape, the lifting pressure (P_i) acting along each box (b_i) was calculated according to the following equation:

$$P_i = q(P_{0,i} + \alpha P_{\alpha,i} + \gamma P_{\gamma,i}) \quad (2)$$

where:

- $q = 0.5\rho V_\infty^2$ is the dynamic pressure, ρ the air density at the flight altitude and V_∞ the airspeed;
- α is the wing angle of attack;
- $P_{0,i}$ is the pressure arising on b_i in correspondence of unitary dynamic pressure at α , γ equal to zero (airfoil baseline camber effect);
- $P_{\alpha,i}$ is the pressure on b_i due only to unitary α at unitary dynamic pressure (incidence effect);
- $P_{\gamma,i}$ is the pressure on b_i due only to unitary γ at unitary dynamic pressure (morphing effect).

Thanks to (eq.2), $P_{0,i}$, $P_{\alpha,i}$ and $P_{\gamma,i}$, where calculated only one time for all the boxes and then combined according to the flight attitude parameters (α , q) and aileron morphed shape (γ) to be investigated. The combination of α , q and γ leading to the most significant pressure levels along aileron segments was then determined and used as design operative condition for structural sizing purpose. All the examined cases are reported in Table 6 and the most critical spanwise pressure distributions (highlighted in red in the table) at the design operative condition occur at $\alpha=2^\circ$, $q=4425\text{N/m}^2$, $\gamma=7^\circ$. Furthermore the load trend has been plotted in Figure 62.

CASE ID	α [°]	δ [°]	γ [°]
0	0	0	0
1	0	-7	0
2	0	7	0
3	0	0	-7
4	0	0	7
20	2	0	0
21	2	-7	0
22	2	7	0
23	2	0	-7
24	2	0	7
30	-3	0	0
31	-3	-7	0
32	-3	7	0
33	-3	0	-7
34	-3	0	7

Table 6 – Aerodynamic cases

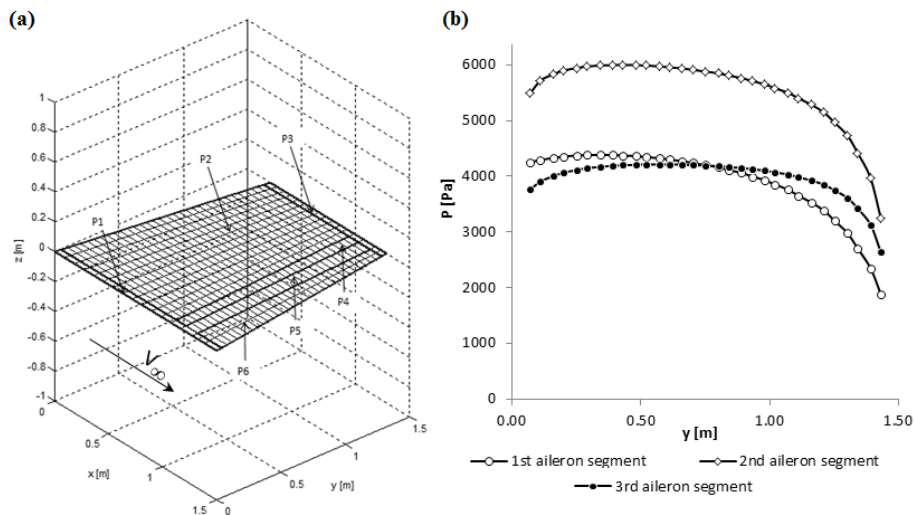


Figure 62 – Aerodynamic grid (a) and loads distributed on the aileron

The estimated loads have been obtained in a conservative approach for the wind tunnel tests. In fact they represent the LL condition for the structural sizing purposes. The true operative conditions expected during WTT have been evaluated accordingly to the

structural safety in order to perform the tests avoiding any kind of damage and they are perfectly enveloped by the most critical case 24.

3.3 Structural Kinematic Concept

When dealing with adaptive lifting surfaces such the aileron, the level of complexity for the structural design naturally increases as a consequence of the augmented functionality of the resulting system. In specific, an adaptive structure ensures the controlled and fully reversible transition from a baseline shape to a set of different configurations, each one characterized by different external load and transmission path of the internal stresses. In order to optimize the structural design of the morphing aileron, the choice of the actuation mechanism become really important. The system must match the design requirements so it has to be compact due to very restricted dimension, rigid in order to withstand external load exhibiting its authority on the morphing capability both during actuation and when blocked. Moreover the weight constraints must be satisfied in order to not annihilate the expected benefit coming from morphing itself. The actuation system peculiarity resided in the fact that it is an un-shafted distributed servo-electromechanical arrangement deployed to achieve the aileron shape transition from the baseline configuration to a set of design target shapes in operative conditions moreover it is self-contained within the structure assuring a smooth surfaces exposed to the flow without fairing. The only kinematic mechanism that satisfy the target specifications is the *oscillating glyph*. The internal structure room define the geometrical parameters which are directly related to the kinematic transmission ratio also defined as mechanical advantage (MA); furthermore it is necessary to identify the number of actuators required to morph the aileron in particular due to small sizes near the tip, the last two bay could not be equipped with the kinematic. In Figure 63, it is shown that the first three ribs are drive by three individual actuators while the passive segment are slaved to the actuated one.

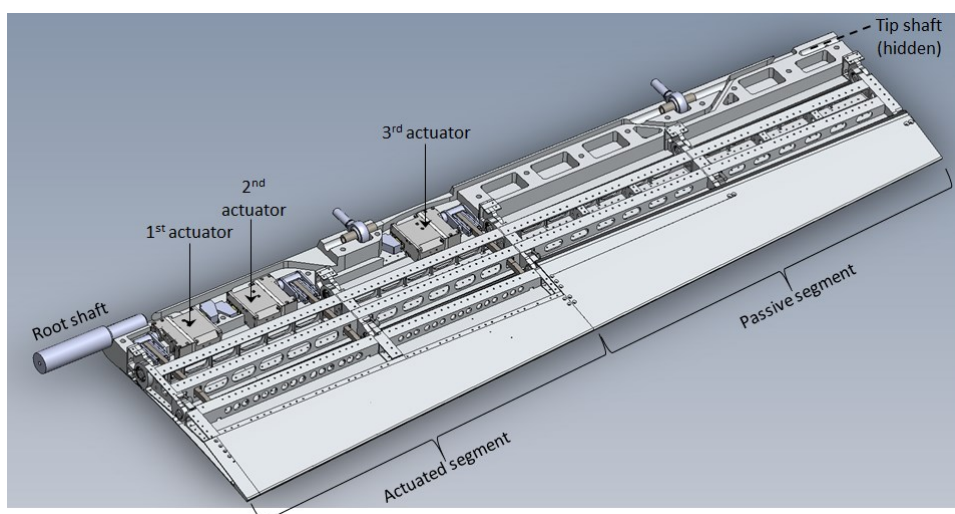


Figure 63 – Actuated and passive zones of the aileron

Each rib actuation kinematic is governed by a single actuators (rotary for this application) that can be also moved in differential manner producing twist but this will not be

performed. The mechanism is depicted in Figure 64. It is called *quick-return mechanism* or *Fairbairn guide*.

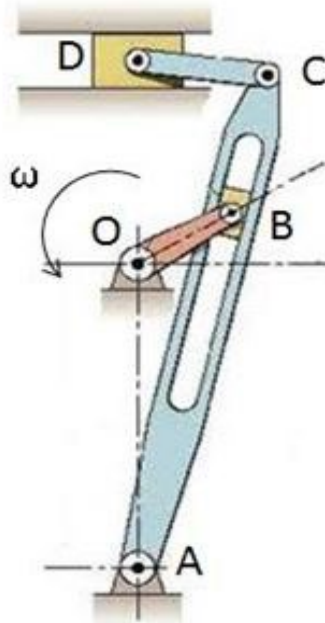


Figure 64 – Quick-return mechanism scheme

The main characteristic of this mechanism is that during the rotation with constant angular speed of the crank OB, the slider B impose to the beam AB a rotation among two extreme positions. There is a conversion of rotary motion of the crank in an alternate linear motion of a slider. The point B moves along two arches of circle of different length so at different speed between going and return path. For this reason it was defined by [42] as turning-block slider-crank chain. The actuation beams of the three actuated portion of the aileron are connected to plate B2 (Figure 58) transmits the actuation torque to the third segment of the rib thus making it to rotate with respect to its original position. In particular, during morphing, the block B2 rotates around an instantaneous rotation center. The instantaneous rotation center is here intended as the point in the moving plane around which all other points are rotating at a specific instant of time. As illustrated in Figure 65 (a), the trajectories of the points in the third block are all circles centered in this point as in the case of a pure rotation. The determination of point V coordinates allows for the estimation of the actuation torque needed to withstand the aerodynamic loads acting on the morphing rib structure.

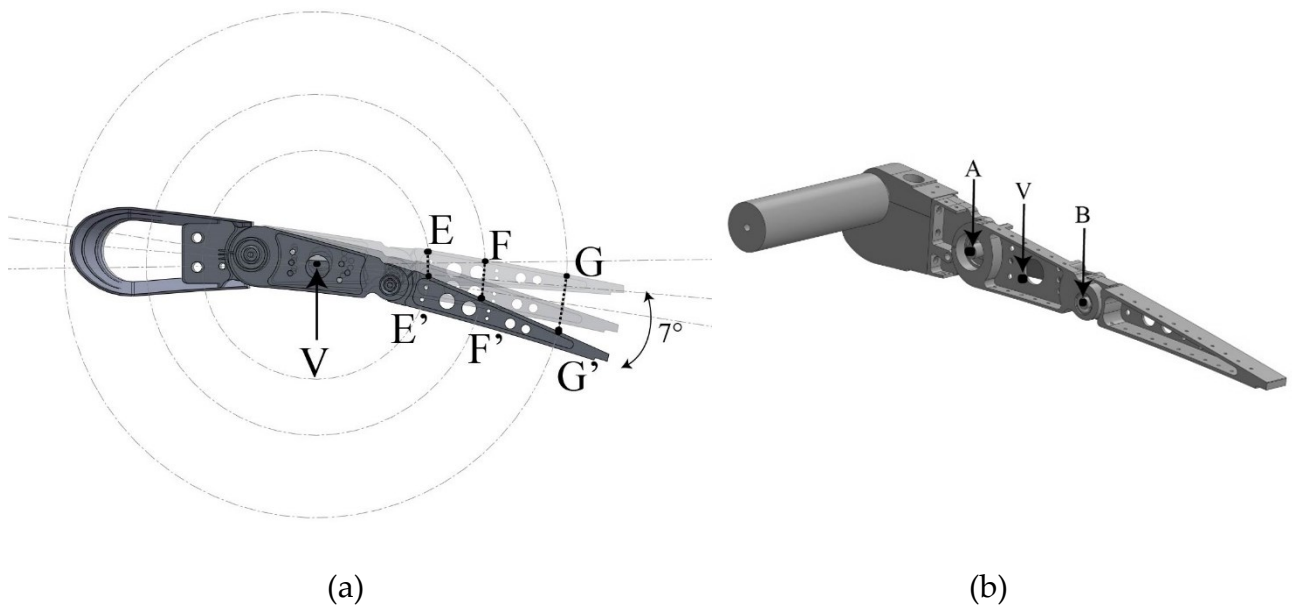


Figure 65 - Circular trajectories of sample points (E, F and G) during morphing (left) and position of hinges A, V and B (right).

The analytical scheme of the mechanism has been carried out in order to define geometrical parameters on which the design is based. Two solutions have been investigated and the basic equations were obtained; furthermore a comparison was performed for discerning the architecture that does not fit the design requirements. The basic necessary equations relate the transmission ratio to the geometrical parameters and the actuator rotation to a specific aileron deflection. After estimating the kinematic behavior of the mechanism, it is necessary to consider stiffness properties, materials, manufacture tools and costs in order to conclude the first loop of design. The analytical model has been validated by means of multi-body simulation and finite elements in order to estimate both stress field distribution over the actuation mechanism and the actuation authority with respect to the target aerodynamic aileron shapes. The numerical simulations were performed under simplified hypothesis that at the same time assure the correctness of the results. The first investigated architecture is schematically depicted in Figure 66.

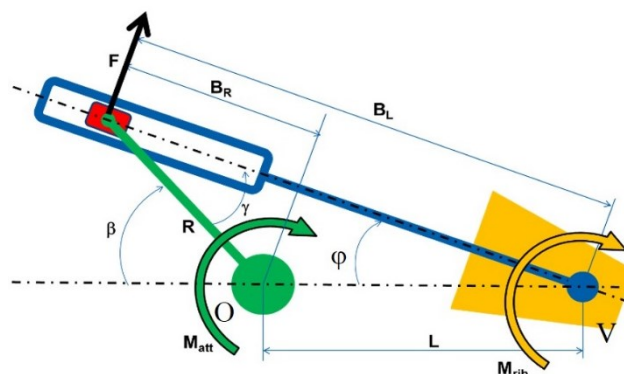


Figure 66 – Oscillating glyph mechanism with internal actuator shaft (O)

The previous configuration is characterized by an internally positioned actuator shaft which is located in O while the point V represent the instantaneous rotation center (also referred as virtual hinge) already defined. This indicates that after estimating the virtual hinge coordinates it is possible to evaluate the L distance that represent the first geometrical

parameter of the mechanism. The actuator shaft rotation of a certain angle (β) produce a crank (R) rotation that forces the sliding element (red) to move along its guide producing a contact force F that counterbalance the external aerodynamic moment. By assuming that the system is perfectly rigid and there is no friction between the components, it follows that the mechanical advantage of the mechanism (MA) can be written as:

$$MA = \frac{LOAD}{DRIVER} = \frac{M_{rib}}{M_{att}} = \frac{FB_L}{FB_R} = \frac{B_L}{B_R} \quad (3)$$

being M_{rib} the torque due to the aerodynamic loads acting on the third rib segment, M_{att} , the torque provided by the actuator to hold the second rib segment in its position, F , the force that the crank produces by means of the cursor, B_L , the arm of the force F , B_R , the projection of the crank along the oscillating rod. From eq. (3), it follows that the mechanical advantage of the mechanism strictly depends upon its geometrical characteristics. The actuation rod is then subjected to the simultaneous action of the force F and the M_{rib} both producing bending stresses. In light of this consideration, it is possible to split the actuation system design in two different phases. Firstly, the geometry of the mechanism shall be defined according to the available room within the aileron structure and the required actuation loads. This aspect becomes fundamental when dealing with an un-shafted arrangement of distributed electrical actuation using a number of actuators to deploy the aircraft control surfaces individually. Secondly, the structural sizing of the components (linear guides, beam, crank dimension and so on) shall be performed by considering the operational (both aerodynamic and structural) loads. In Figure 67 is reported the MA trend for different $\frac{L}{R}$ ratio with the rib morphing angle ϕ .

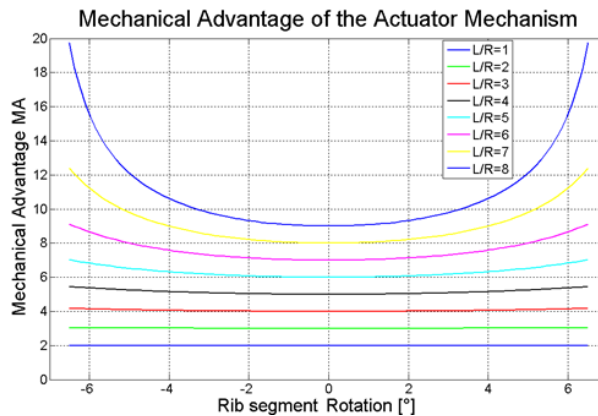


Figure 67 – MA of the mechanism for different geometrical parameters.

Increasing $\frac{L}{R}$ ratio means increased MA and for a fixed value of $\frac{L}{R}$ the MA increase with the rib segment rotation. This means that, as the aileron camber increase, high aerodynamic load are produced; then the mechanism exhibit the highest MA resulting that a lower actuation torque is required to equilibrate the system rather than at the baseline configuration. This suggest that in order to approach the design in a conservative manner, the condition of maximum load (fully morphed down) with mechanism at the lowest mechanical advantage (baseline) must be set. With simple mathematical manipulation

coming from trigonometric relation among angles, the equation relating actuator rotation with the rib deflection can be easily obtained:

$$\cot \varphi = \frac{L}{R \sin \beta} + \cot \beta \quad (4)$$

This equation is helpful for estimating the maximum excursion, in term of rotation, that the actuator must supply in order that a crank rotation, for a given MA , determines the desired rib deflection. As already done for the mechanical advantage, the graph in Figure 68 show the trend of equation (4).

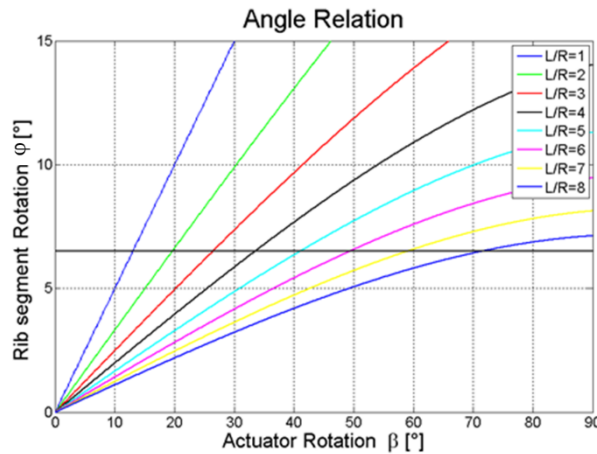


Figure 68 – Rib rotation versus actuator shaft rotation (inner actuator)

It indicates that a fixed rib rotation is obtained by highest values of crank rotation for increased L/R . Greater L/R ratio leads to high transmission advantage however on the other hand, also the mechanical advantage of the mechanism may be constrained by physical limits in the servo rotary actuator rotations and more available room. The final architecture is then obtained by means of a trade-off among the two described constraints. The kinematic analysis of the mechanism shown in Figure 69 can be deduced with the same considerations already mentioned with the previous architectures. The mechanical advantage can be expressed in the same manner as follow:

$$MA = \frac{LOAD}{DRIVER} = \frac{M_{rib}}{M_{att}} = \frac{FB_L}{FB_R} = \frac{B_L}{B_R} \quad (5)$$

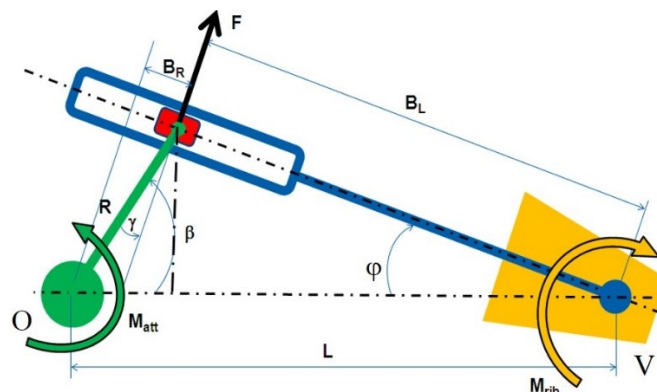


Figure 69 – Oscillating glyph mechanism with external actuator shaft (O)

In Figure 70 is reported the *MA* trend for different geometrical parameters. Also in this case it is noteworthy that *MA* increase as the ratio L/R grows.

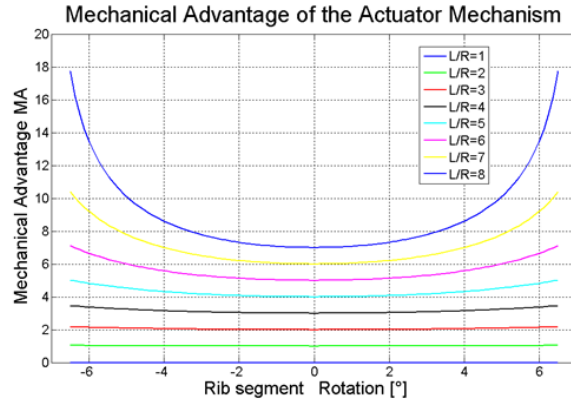


Figure 70 - MA of the mechanism for different geometrical parameters

However it is evident that the configuration with inner actuator shaft exhibit lower performance if compared with the external actuator one. This can be demonstrated showing that for a given L/R and rib angle the mechanical advantage is lower than the correspondent of the first configuration. Finally, the relation that link the actuator shaft rotation with the rib segment angle can be obtained and it has the following form:

$$\cot \varphi = \frac{L}{R \sin \beta} - \cot \beta \quad (6)$$

Its graphical trend is reported in Figure 71. Comparing the two configuration it can be shown that the external actuator arrangement exhibit, for a given L/R , smaller crank rotation to obtain the same rib segment rotation. This implies small crank size.

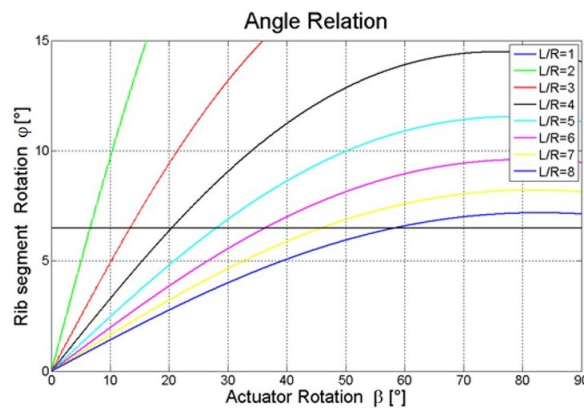


Figure 71 - Rib rotation vs actuator shaft rotation (external actuator)

In any case, both architectures reveal their capability to face great external moment with modest actuator torque leading to benefit in terms of weight, volume and size. The herein conducted analyses are necessary for the further sizing of the real mechanism components because the actuation system housing inside the morphing aileron and the required space for its handling are well estimated. These information constitute the input parameters for the detailed design of the mechanism. The geometrical constraints of the aileron (reduced

volume) are one of the most important aspect that affect the choice of the actuation system configuration. In fact, a complete trade-off analysis has been carried out and widely described in the next section. Due to limited available space between the rib block B0 and the aileron leading edge extremity, it is not possible to achieve high value of L/R ratio with repercussion on the whole design. In fact the configuration with inner actuator shaft cannot be considered for detailed design purposes because the actuator would interfere with LE leading furthermore to lower mechanical advantage with the inability to withstand external loads. On the base of the operative loads described in the previous chapter, the external moments acting on each actuated ribs with reference to the virtual hinge has been estimated. It has been evaluated by multiplying the normal force on the i -th aerodynamic panel for the distance from the point V and finally adding each results. In such manner the moment was scaled by the kinematic mechanical advantage in order to obtain the actuator torque required to equilibrate the system under prescribed loads. Defined the actuation system mechanism, it is desirable to direct the design toward components off the shelf (COTS) soon available on the market and only if they doesn't respond to design requirements the architecture must be customized with "ad-hoc" components. For the morphing aileron, both linear guides and cam follower solutions have been investigated. It can be found many types of linear guide on the market, which differ on the base of maximum allowable load, mass, sliding mechanism (recirculating and non-recirculating balls), sizes and so on. Due to aileron restricted room, only miniaturized linear guides have been taken into account in a sort of invers process where firstly, the size requirements were verified and then the capability to withstand loads. Figure 72 shows the main geometrical parameters that must be set for the components (linear guide and cam follower) in order to avoid, during the morphing, any interference with the upper and lower skin. In the case of the linear guide, the side dimension of the rail is important because it is directly connected with the actuation beam driving the cross-section moment of inertia which is the parameters that define the beam behavior at bending sollicitations. On the other hand (Figure 73), the cam follower diameter drive the beam height by means of the thickness where the cam bearing is positioned. In this region occur high concentrated stress generated by the actuation vertical forces produced by the cam contact and rolling movement during the morphing.

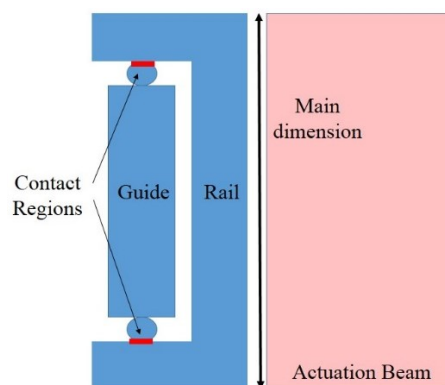


Figure 72 – Conceptual scheme of the linear guide based on recirculating balls.

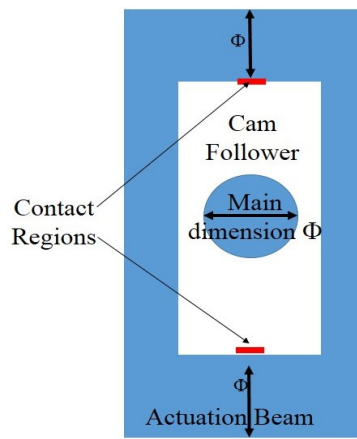


Figure 73 – Conceptual scheme of the cam follower.

In the next Figure 74, it can be seen that some producers build linear guides and cam follower in a wide range of dimension from the biggest one to the smallest. The choice of the appropriate components for the aileron actuation mechanism, was driven by the dimension imposed by the smallest actuated rib.



(a)



(b)

Figure 74 – Example of linear guides and cam followers

The complete actuation system is then composed of: a crank which transmit the actuator torque to the guide that in turn, by means of the contact produced with the rail, generate a vertical force, and a robust leverage that impose the correct rotation to rib segment which is connected. In light of this considerations, it can be noticed that the beam is strictly subjected to bending and torsional stress that are transmitted on the guides. The static load applied on the linear guide is defined as the static load which gives a defined constant contact stress (by the producer) at the centre of the contact area between the rolling element and the raceway receiving the maximum load. This is the limit maximum load at which the elastic deformation of the rolling element guarantee at least accuracy and smooth rolling movement. For this reason, all the components must be studied and validated by means of finite element model and experimental validations.

3.4 *Actuation System Design*

3.4.1 *Trade-off among different concept*

In a morphing aircraft design concept, the actuated system stiffness, load capacity and integral volumetric requirements drive flutter, strength and aerodynamic performance. Design studies concerning aircraft flight speed, manoeuvre load factor and actuator response provide sensitivities in structural weight, aeroelastic performance and actuator flight load distributions. Based on these considerations, actuation mechanism constitutes a very crucial aspect for morphing structures design because the main requirement is to accomplish variable wing shapes within the limits established by the appropriate actuation arrangement. Hydraulic actuators are typically used for primary flight control surfaces due to the high forces required. Whereas electromechanical actuators are considered too slow and bulky to compete with hydraulics on surface actuation, the advent of digital motors have made electromechanical actuators a viable solution for controlling some secondary surfaces in which jam is not catastrophic and a hydraulic motor may be used in parallel. The use of electro-mechanical actuators is coherent with a “more electric approach” for next-generation aircraft design. Benefits are obvious. No hydraulic supply buses (easier to maintain and store without hydraulics leaks), improved torque control, more efficiency without fluid losses and elimination of flammable fluids. In addition, it is potentially possible to move individual ribs either synchronously or independently to different angles (twist) in order to enhance aerodynamic benefits during flight. On the other side, actuators susceptibility to jamming may represent the most important drawback. In what follows, different actuation concepts able to transform the actuator torque into the aileron morphing deflection are assessed for a trade-off study. In detail, five actuation concepts based on either precision linear guides or cam followers are investigated to transmit actuation forces to the structure in order to fulfil general design targets, such as:

- compactness and lightness for a self-contained morphing application;
- morphing capability and structural robustness under the operative loads;
- wider stress distribution over the actuation components.

Five different distributed actuation arrangements were specifically developed for the morphing aileron. In specific, the distributed actuation design consists of a number of actuators potentially enabling a redundant and fault tolerant operation of the adaptive ribs. In this work, the following solutions were investigated:

- linear guide with rollers with arm linked to the first movable rib block (*B2*);
- precision linear slide with recirculating and non-recirculating ball carriages driving the second movable rib block (*B3*).
- cam follower with arm linked to the second movable rib block (*B3*);
- cylindrical ball bearing guide mechanism driving the second movable rib block (*B3*).

The actuation system design included the worst design case in terms of operative loads and room available for the kinematics. For this reason, the third aileron rib (Rib3) was taken into

account for the structural sizing of the actuation architecture (Figure 75). Due to their small size, Ribs 4 and 5 were considered passive and their movements slaved to Rib 3.

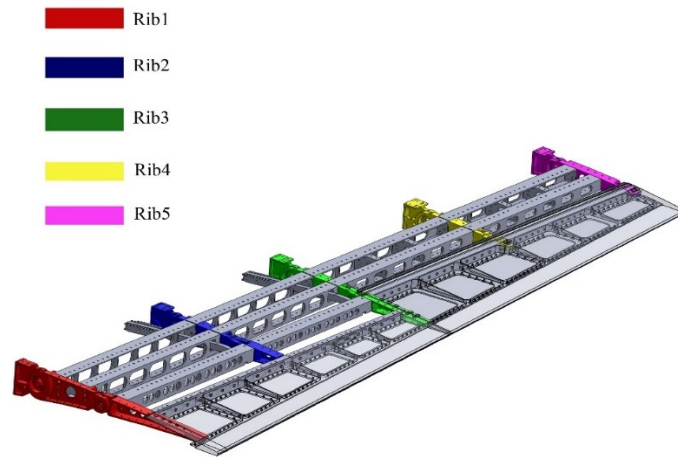


Figure 75 – Aileron inner structure with coloured segmented rib

3.4.2 Linear Guides with Roller

The first concept is based on the adoption of a compact linear guide characterized by a slider and a steel rail with a C-shaped cross section (Figure 76). The slider is equipped with radial bearing rollers in alternating contact with both sides of the raceway. Radial bearings enable the guide to withstand high forces normal to the sliding line (in the order of 800 N).

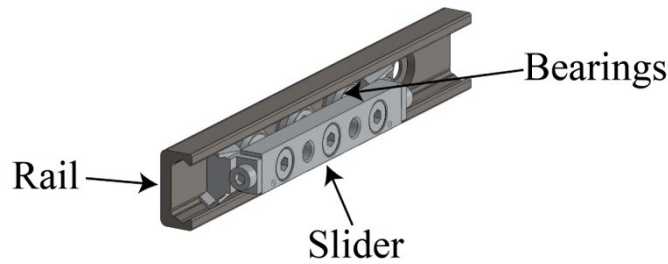


Figure 76 – CAD of the linear guide with rollers.

As shown in Figure 77, such a device is fastened to the actuation steel rod of the morphing aileron driving the morphing rib kinematics through the control of B2 position. On the other side, the system transforms the actuator rotation in actuation force by means of the actuation leverage made of a crank.

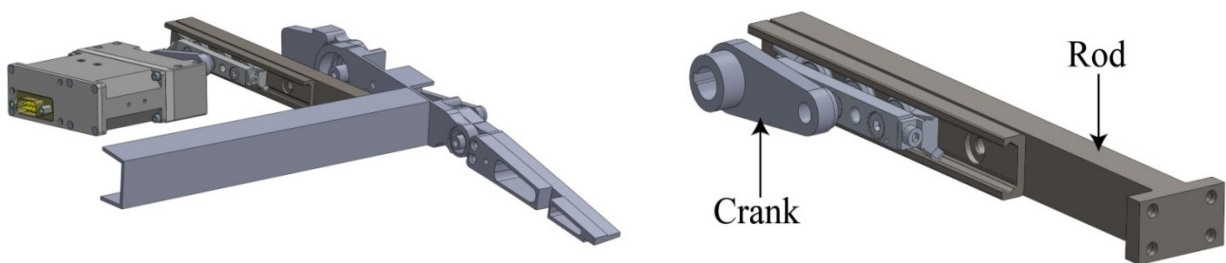


Figure 77 – Schematic CAD model of the actuation mechanism concept based on the rollers.

3.4.3 Precision Linear Slide

A precision linear slide with recirculating and non-recirculating ball carriages were investigated (Figure 78) as alternative solution to the linear guide. The former is made of a light weight and compact linear motion rolling guide comprising a U-shaped slip-table and a stainless steel track rail obtained by precision forming. The latter is made of a synthetic resin retainer used to host the balls while preventing their contact noise. The actuation architecture is shown in Figure 79.

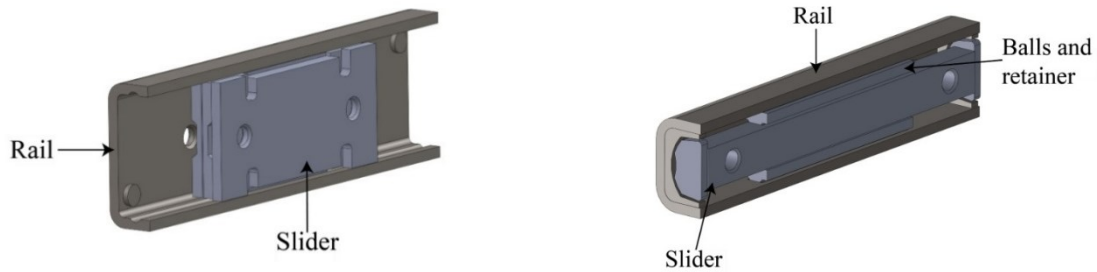


Figure 78 – Precision linear slide with recirculating (left) and non-recirculating (right) ball carriages

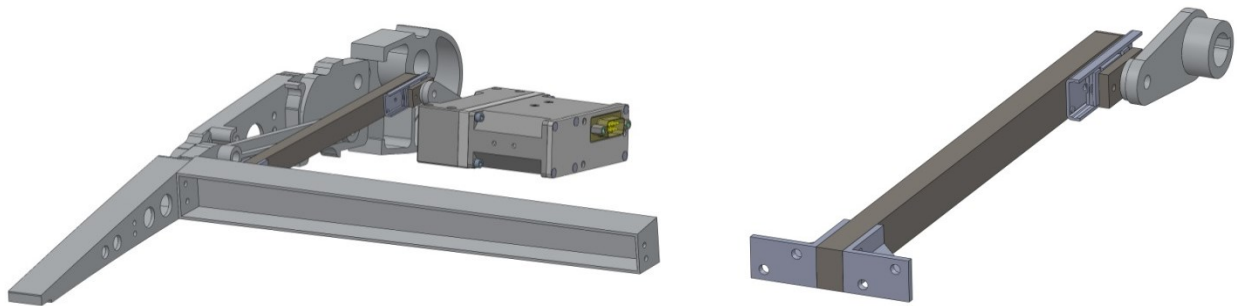


Figure 79 - CAD of the actuation system concept using a precision linear slide mechanism

3.4.4 Cam Followers

Cam followers are bearing provided with a stud in which needle rollers are assembled in a thick outer ring. They exhibit small friction coefficient and excellent rotating performances with high radial load capacity. The inner components are shown in Figure 80.

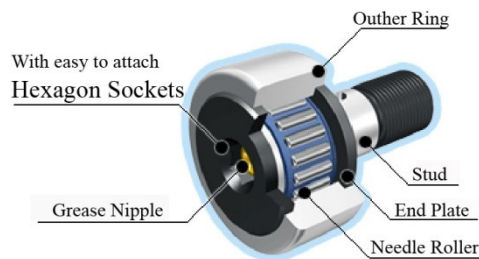


Figure 80 – Cam Follower components

In order to maximise the mechanical advantage (L/R increase) with respect to the previous configuration and to prevent potential mechanical plays arising during the manufacturing process, it was decided to connect the actuation rod to the rib block B3. The installation layout conceived for this solution is shown in Figure 81.

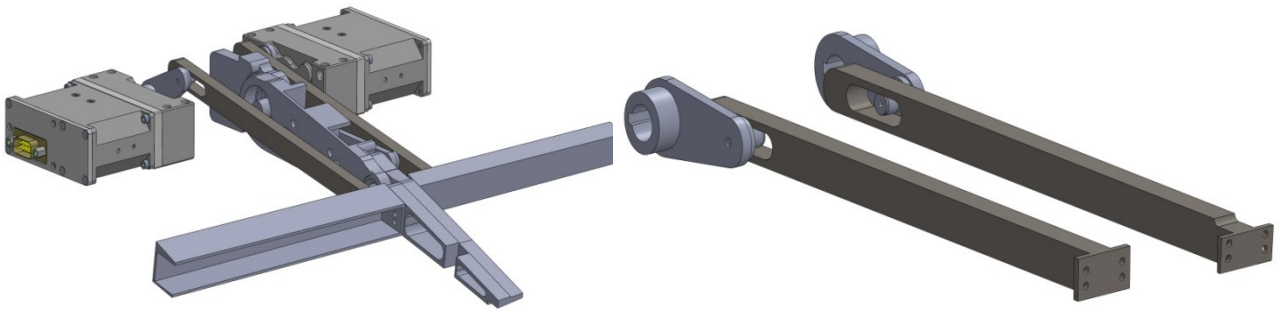


Figure 81 - Cam follower-based actuation system

It has to be noticed that cam follower shall be positioned along the beam longitudinal axis inside the grinding surface. In order to transmit the actuator torque, the cam shall go in contact with the upper (morphed down) or lower (morphed up) sides of the grinding surface. At the same time rotation and sliding must be ensured during deflection. This means that beam cross section shall be sized on the base of the cam diameter; however due to high load, the contact surface between the cam and the beam may be subjected to excessive stresses because of the low thickness. On the other hand, the increased distance between the actuator shaft and the morphing pivot results in higher mechanical advantage at the expenses of a largest beam excursions during operation.

3.4.5 *Ball Bearing Guide Mechanism*

A new architecture based on a cylindrical bushing which slides along a cylindrical beam is here considered. The device is sketched in Figure 82. This concept represents a more compact solution leading to smaller (upper and lower) excursions of the actuation beam during operation but with limited mechanical advantage. The system architecture is shown in Figure 84, detailing the morphed down configuration and the kinematic components like beam, cylindrical bearing, fork and actuator crank.



Figure 82 - Main components of the ball bearing guide mechanism

This architecture refers to the analytical scheme depicted in Figure 83.

3.4.6 Actuation System Selection

In this section, the actuation concepts are assessed in terms of mechanical advantage, excursion angle, dimensions and structural interferences. By limiting the study to a single design case concerning Rib 3, the achieved results are summarized in Table 7. Such solutions are those avoiding any structural interference with morphing aileron skin and spars while deployed. A comparison between the mechanical advantages versus rib morphing angle (ϕ) of the different architectures are reported in Figure 85.

CONFIGURATION	ϕ [deg]		L [mm]	R [mm]	MA at 7°	β [deg]	s (mm)	N
	Morphed d up	Morphed down						
Linear guide with Rollers	7	-7	92,8	30	2,3	15,2	2,2	5
Cam Follower	5	-4	117,9	30	7,3	49,7	16	5
Cylindrical ball bearing guide	5	-4	127,2	30	7,3	60	14,14	3
Recirculating balls	6,5	-4	121	30	8,5	52,7	17,65	3
Non-Recirculating balls	7	-4	119,2	35	4,2	37,3	12,68	3

Table 7 - Comparison of investigated actuation concepts

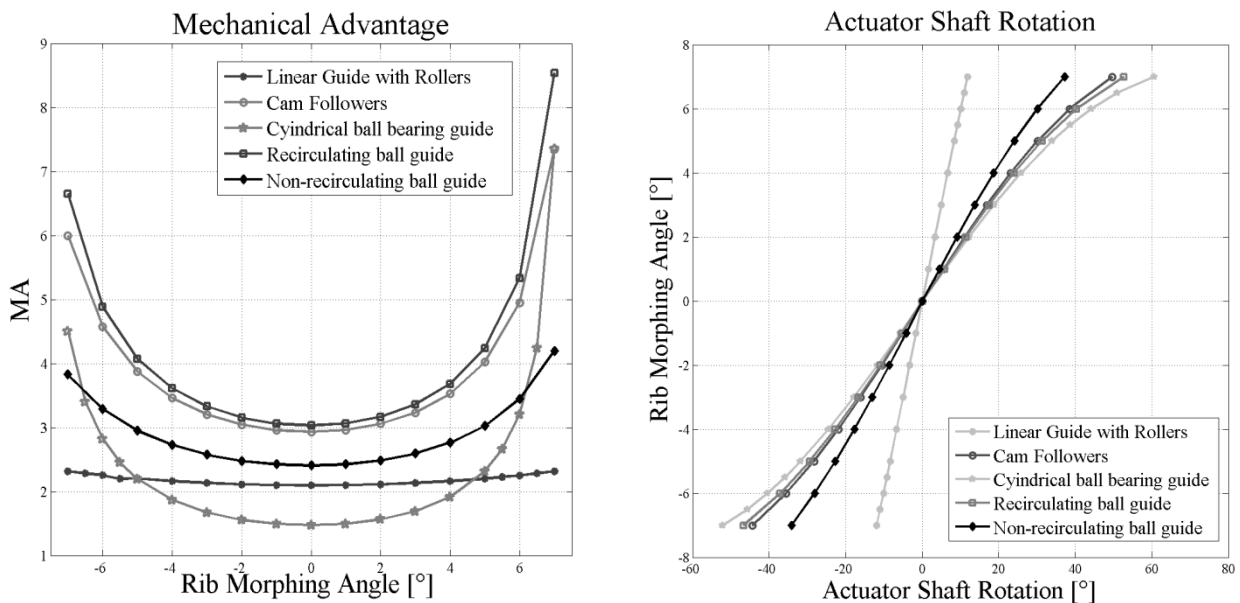


Figure 85 - Comparison of MA and actuator shaft rotation achieved by the investigated actuation concepts

A full deployment up to $\pm 7^\circ$ of morphing is guaranteed by the linear guide solution with rollers, thanks to the resulting lower actuator rotation. Being linked to the first movable part (B1) of the rib, this solution may be affected by mechanical plays which may potentially arise during the manufacturing and assembly phases. Furthermore, due to the low L/R ratio, this architecture exhibits low mechanical advantage. In the cam follower-based concept, the morphing deflection is drastically reduced to $+5/-4$ degrees due to the interference arising between the actuation rod and the upper/lower skin during morphing operation. Similarly, despite its small size, linear guide rail architecture enables morphing aileron deflection in

the range between + 6.5 degree to -4 degree due to the structural interferences occurring with upper and lower skin. Finally, the cylindrical ball bearing guide was excluded due to the decreased mechanical advantage associated with the limited BL. In order to fulfil the design target shapes in morphed down configuration, both recirculating and the non-recirculating ball carriage-based actuation concepts were selected. However, these solutions are unable to reach morphing angles major than -4° in morphed up configuration. Nevertheless, being the most promising devices, such solutions have been further FE model investigated from the structural standpoint in order to be implemented in the morphing aileron. It is then meaningful to validate the analytic model that describes the glyph mechanism with a multi-body simulation where the body are considered rigid point with concentrated mass and stiffness. This analysis was conducted on the precision linear guide with recirculating ball carriages and the results are depicted in the graph in Figure 86.

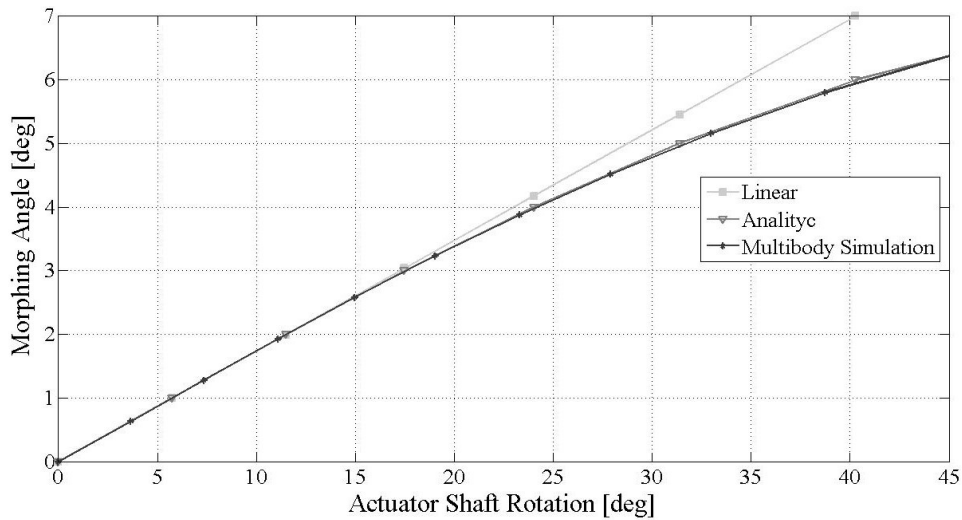


Figure 86 – Comparison between linear, analytic and multi-body simulation.

The curve represent the equation (6) trend and shows a correlation with the numerical simulation. It can be noted that in the range of actuator rotation 0-25 degree, the curve is linear. The pressure distribution calculated by means of the VLM method (see section 3.2), was approximated by equivalent lumped loads applied to each aileron rib, as shown in Figure 87. In particular the Rib 3 was taken into account because it resulted the most loaded.

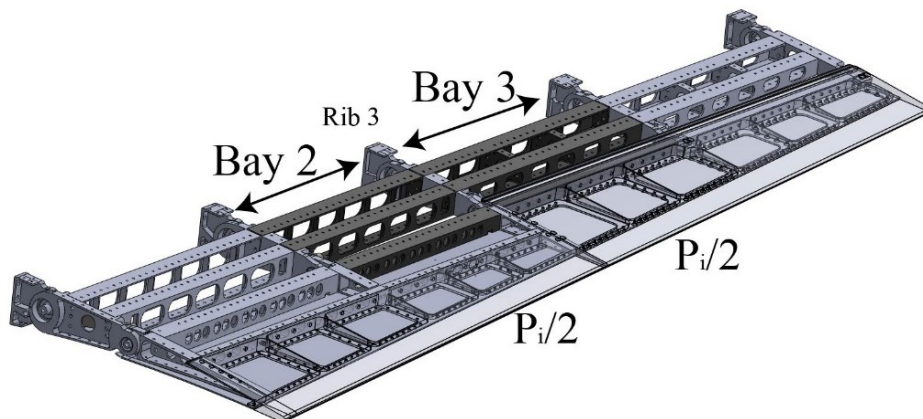


Figure 87 – Sketch of the concentrated load evaluation (hidden skin)

linear guide is blocked in fact, the actuation beam is simultaneously loaded with the external aerodynamic moment (respect to V), the vertical static force acting on the slider and a horizontal component (linked to the jamming), both producing a pure bending state with a higher stress level rather than the free guide. These considerations are validated by the study conducted by [19], where a non-linear simulation was conducted, showing a low level of solicitations. The hypothesis of a perfect bonding between the rail and slider was formulated and implemented; in such manner, the analyses was then conducted. The reaction force acting on the linear guide for a given aerodynamic moment was firstly evaluated and then compared to the expected actuation torque, as shown in Table 8 for a given *BR* length at 5 deg. This conservative approach assumed that the baseline (un-morphed) structure, whose actuation chain exhibits the lowest mechanical advantage, was loaded by the highest aerodynamic moment (33.81 Nm) associated with the morphed configuration (+7 deg). For different morphing angles and MA, FEA results are reported in Figure 89, Figure 90 and Figure 91, in terms of total displacements (maximum value: 3.01 mm at beam tip) and load transmitted to the guide (maximum value 371 N).

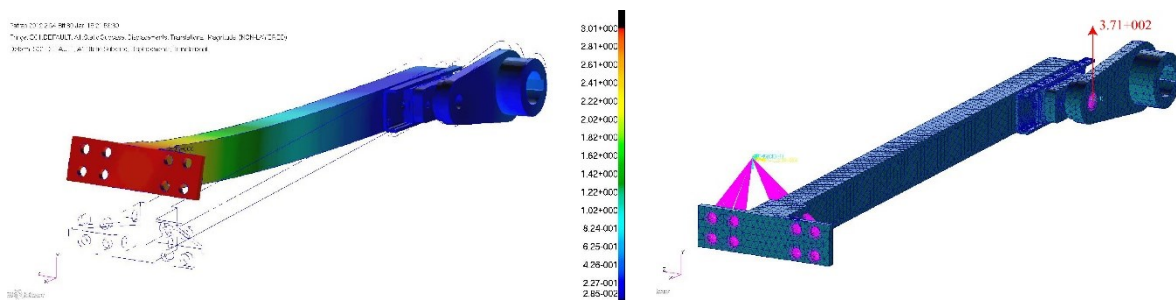


Figure 89 - Beam displacement contour (left); guide reaction loads of 371 N (right)

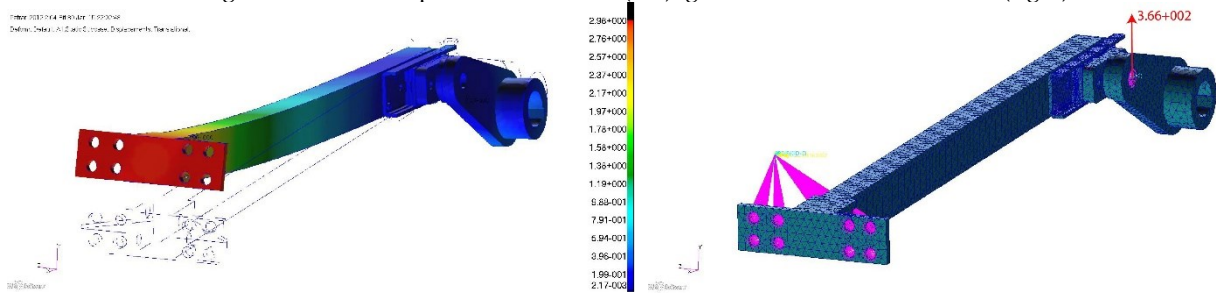


Figure 90 - Beam displacement contour (left); guide reaction loads of 366 N (right)

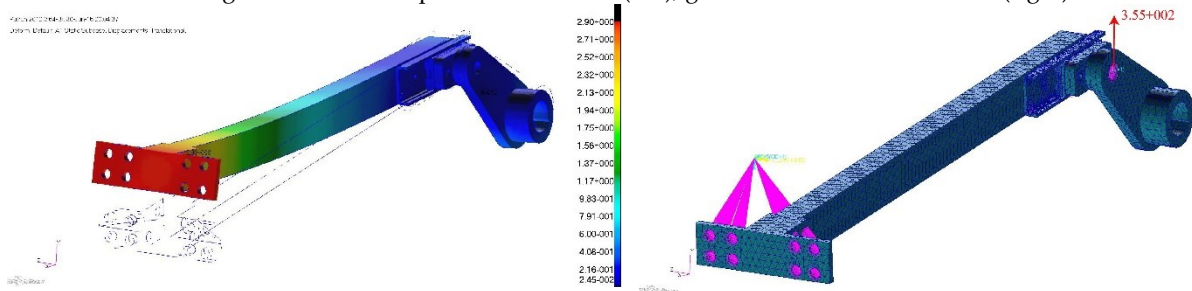


Figure 91 - Beam displacement contour (left); guide reaction loads of 355 N (right)

Furthermore, the stress acting on the linear guide are depicted in Figure 92. It is reported the Von Mises magnitude stress and its component among x direction. It is noticeable the high stress level in the contact region in Figure 93.

Stress Magnitude (MPa)

σ_x (MPa)

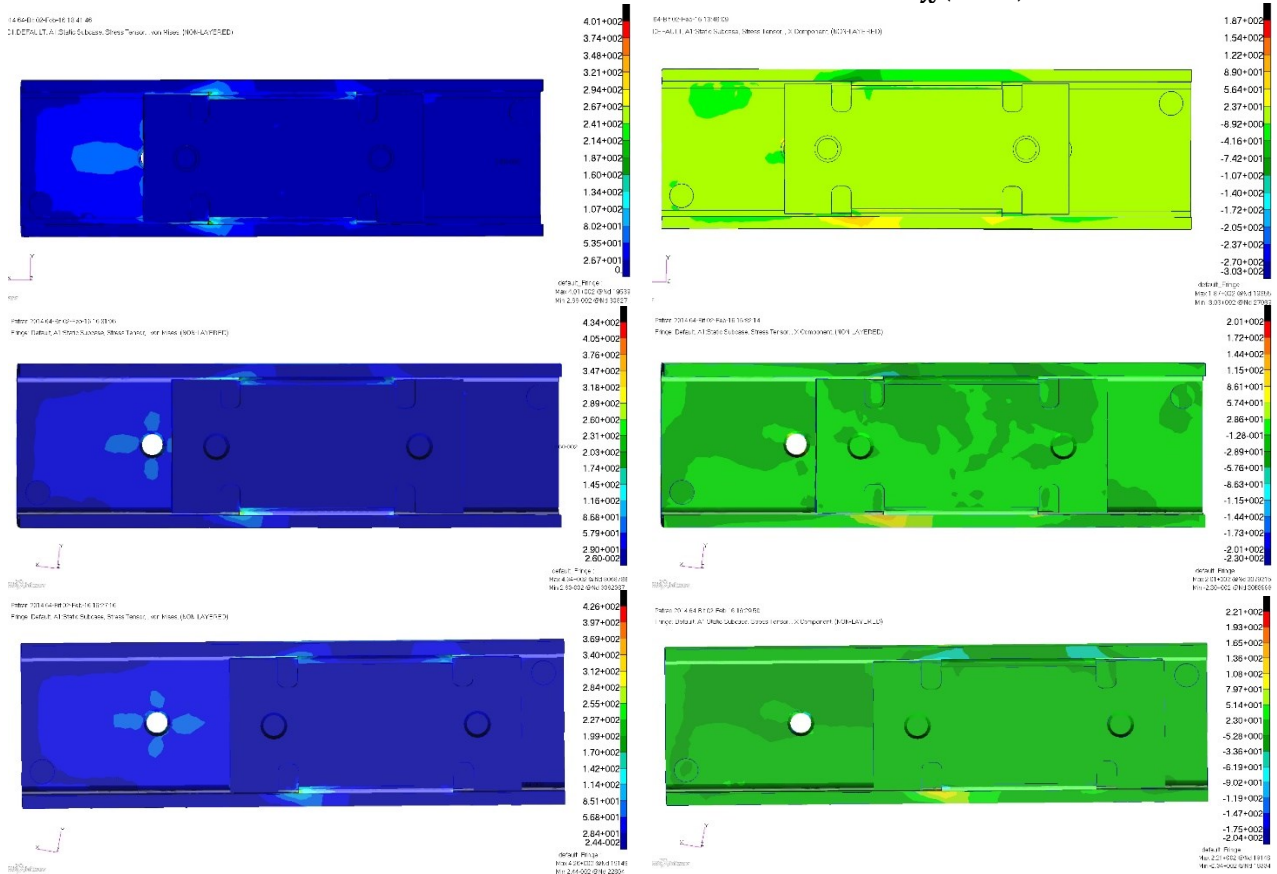


Figure 92 – Stress contour on linear guide

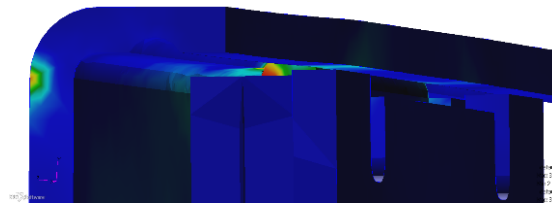


Figure 93 - Stress peak in the contact region between slider and rail

Figure 94 shows the comparison between the analytical and FE results for the selected aerodynamic moment and for a given set of morphing angles. An excellent agreement between the two curves was achieved.

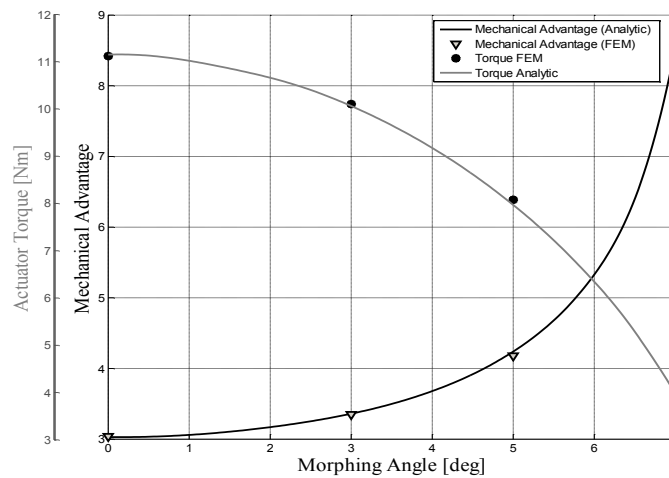


Figure 94 - Comparison between analytical and numerical trend of Actuation torque and Mechanical Advantage versus Morphing Angle (ϕ)

Being the maximum allowable static force that can be applied to the linear guide limited to 140 N [44], it was then demonstrated that single linear guide solution was structurally inadequate. As a result, an alternative linear guide-based device based on a non-recirculating ball carriage Figure 78 (right) was investigated. This device exhibits substantial benefits, mostly resulting in an increased allowable static force equal to 232 N [44]. In addition, in order to mitigate the maximum counterbalancing load acting on the guide to equilibrate the aerodynamic moment, a fork-shaped crank coupled with a double sided linear guide was also preferred with positive effect on the beam torsion that is completely avoided. Nevertheless, such a solution resulted in a lower mechanical advantage for the given morphing angle due to the slightly lower B_L . In the same way, a multi-body simulation was performed for the non-recirculating ball carriage. In particular, two conditions have been examined: a conservative design approach and a refinement analysis. The first one consists of analyse the structure with the most sever load condition expected (33.8 Nm at +7°deg) with minimum mechanical advantage which correspond to structure physically positioned in the un-morphed configuration. The last one is more similar to the real working of the actuation system due to the linear variability of the moment from the minimum of 23.29 Nm to 33.8 Nm with consequent change of the mechanical advantage with morphing angle. The main results are shown in the following graphs (Figure 95). For the first case, it can be deduced that the actuator torque decrease with morphing angle due to increasing of MA , while the vertical static force also decrease with morphing angle. Moreover for the second case, the actuator torque envelope is well below the limit of 13 Nm and the vertical static force increase with morphing angle due to the increased external moment. This confirm that the most critical design condition can be considered when the actuation system is at the minimum mechanical advantage with the maximum load relative to the morphed configuration, because physically, when the aileron is positioned at its maximum deflection, the leverage amplification factor is maximum and the critical point is obtained at an intermediate angle value at which correspond a lower aerodynamic moment leading to a not conservative design.

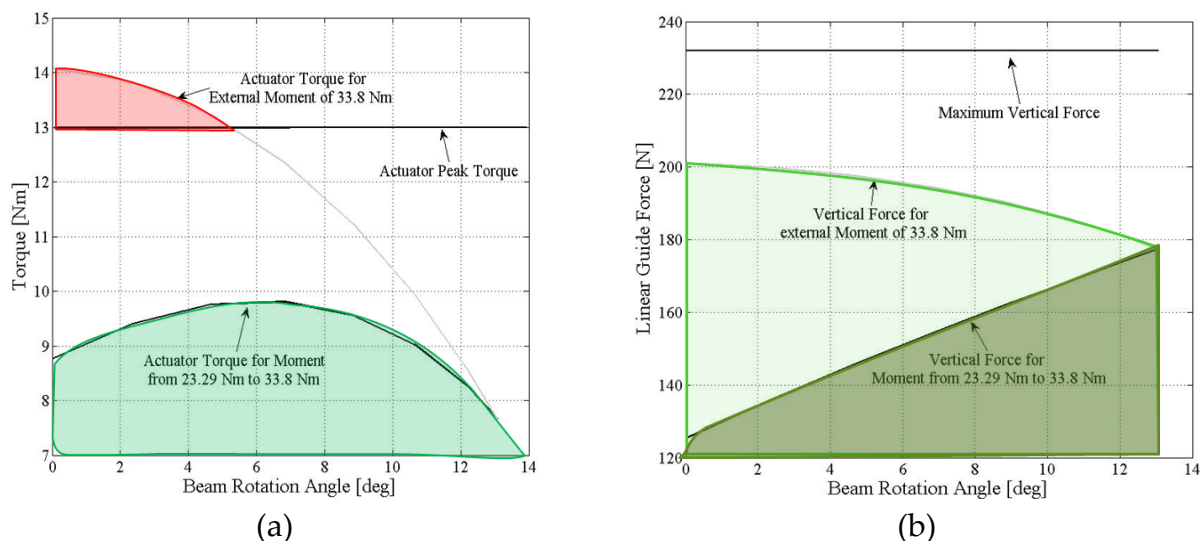


Figure 95 – Multi-body simulation with allowable design region for actuator torque (a) and linear guide vertical force (b)

3.5 FE model and stress results at LL and UL

3.5.1 Reference system, conventions and units of measure

The reference Cartesian system S_1 (Figure 96) was used as datum for all the analyses addressed by this document; the following conceptual definition applies to S_1 :

- Origin (O) located on the root rib, in correspondence of the hinge between aileron leading edge and the first movable segment [1];
- X-axis onto root rib plane, joining O with the trailing edge of the airfoil, and aft oriented;
- Z-axis normal to the root rib plane and oriented towards the WT (Wind Tunnel) floor;
- Y-axis perpendicular to XOY and oriented to complete the left-handed Cartesian system.

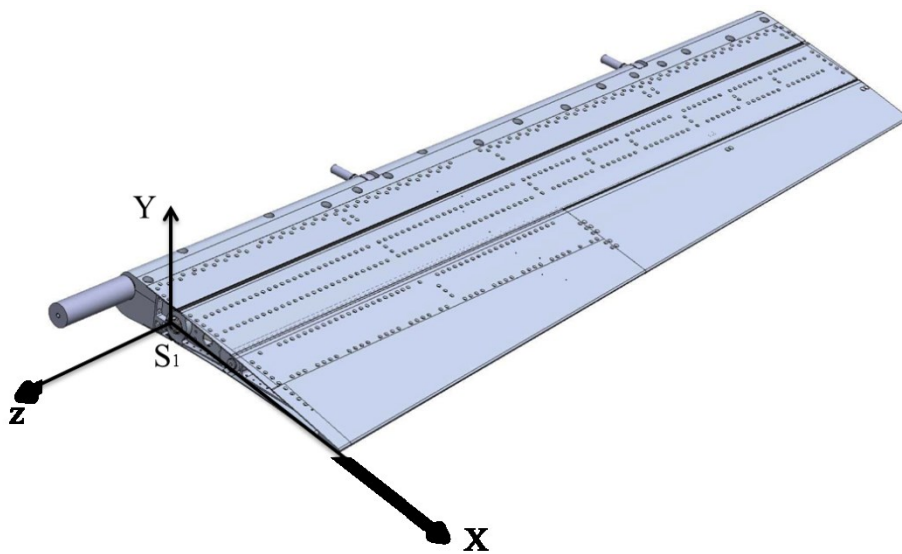


Figure 96 - Reference system S_1

Forces and moments components were assumed positive if coherent to S_1 axes orientation; more in detail:

- forces components were considered positive in sign if oriented as S_1 axes;
- moments components were considered positive in sign if inducing counter-clockwise rotations about S_1 axes.

Unless otherwise specified, all the units of measure adopted in this document have to be intended as referred to the International System. The following exceptions applies:

- Length: Millimeters [mm]
- Mass: Tons [T]
- Force: Newton [N]

3.5.2 FE model description

The FE model is representative of the 3D CAD of entire aileron demonstrator. It includes main structural components such as segmented ribs and spars, actuation system leverage and skin panels. Solid elements (CTETRA) were used for the mesh of the primary structure and the actuation leverage, meanwhile beam elements (CBEAM) were used for modeling all the joints (fasteners, hinges, pins and so on). FE model general data have been recapped in Table 9.

FE Model general data	
Number of Elements	2.138 E+6
Number of Nodes	1.393 E+6
Estimated DOFs	3.638 E+6
Total estimated Volume [m3]	6.785 E+6
Total estimated Mass [Kg]	21.00
Moment of inertia about aileron hinge-line, I_{HI} [Kg*m ²]	0.403

Table 9 - Aileron FEM, general data

3.5.3 Primary structure

The aileron primary structure is composed of ribs, actuation kinematic chains, spars and skin. Aileron leading edge was not modelled for stress analysis purposes; it was considered only to properly evaluate the interface loads transmitted by the aileron to the wing box (paragraph xx). In Figure 97, a global view of the aileron FE model is depicted while in Figure 98 (a) and (b) details of rib and spars meshes are shown. As reported in [xx], the rib is segmented in 3 blocks which are internally connected by rotational hinges and links. The system is a SDOF kinematic driven by load-bearing actuators. The entire structure is arranged in 5 bays where the first 2 bays (separated by 3 ribs) are actuated. Due to their small size, Ribs 4 and 5 were considered passive and their movements slaved to the actuated portion of the aileron. The inner structure is covered by a segmented aluminum skin in an *armadillo-like* configuration where each segment slides along the consecutive one (in the chord-wise direction); silicon strips are used to fill the gaps between the skin segments and do not play any role in the adsorption of external loads. The connections between rib blocks, spars and skin, have been modeled by means of MPC, type RBE2.

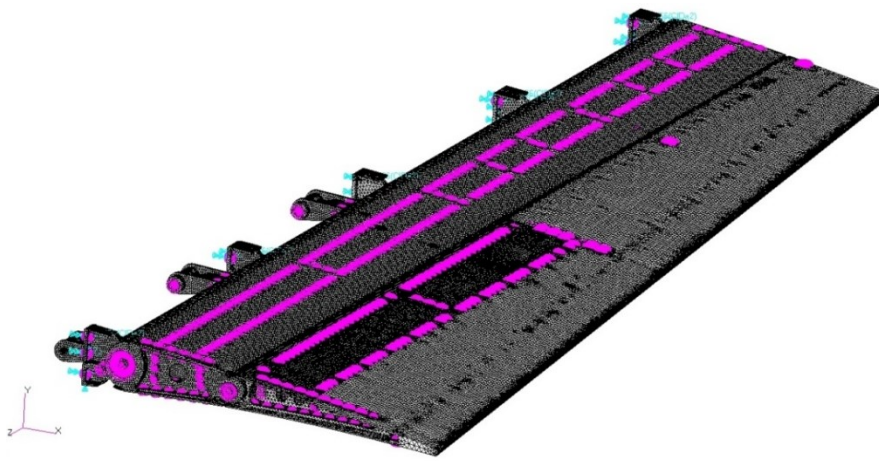


Figure 97 - Aileron FE model

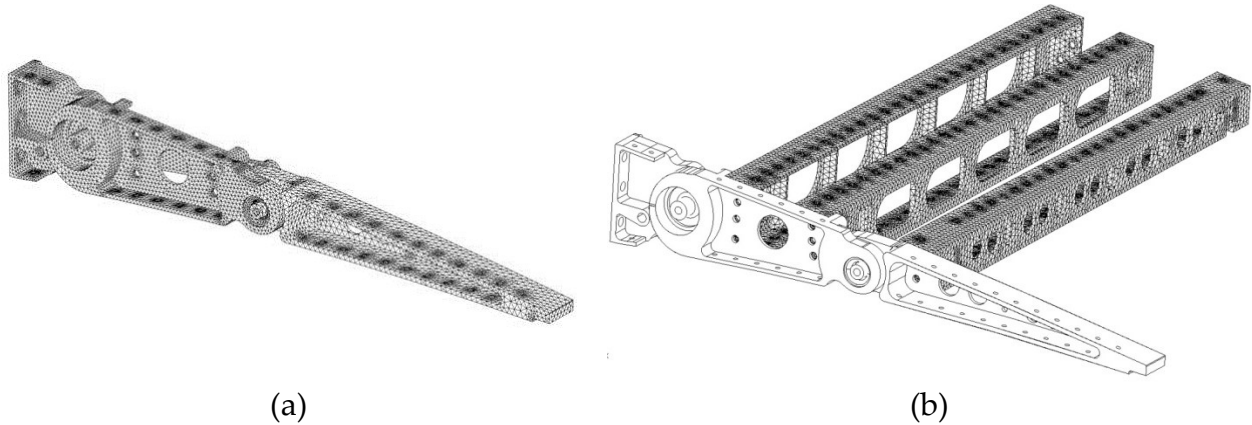


Figure 98 - (a) Aileron Rib solid mesh (CTETRA), (b) Spar solid mesh (CTETRA)

Main mechanical properties of the materials adopted for the aileron components are listed in the next table; in Figure 99 and Figure 100, aileron components have been colored according to their constitutive material: the aluminum components are depicted in grey while the steel components in black.

Material (isotropic)	E [Gpa]	ρ [kg/m ³]	ν	Items
Steel C50	220	7850	0.3	Beam of the actuation system, linear guide features, crank and rib links
Al 2024-T351	70	2768	0.33	All other items

Table 10 - Mechanical properties of adopted materials

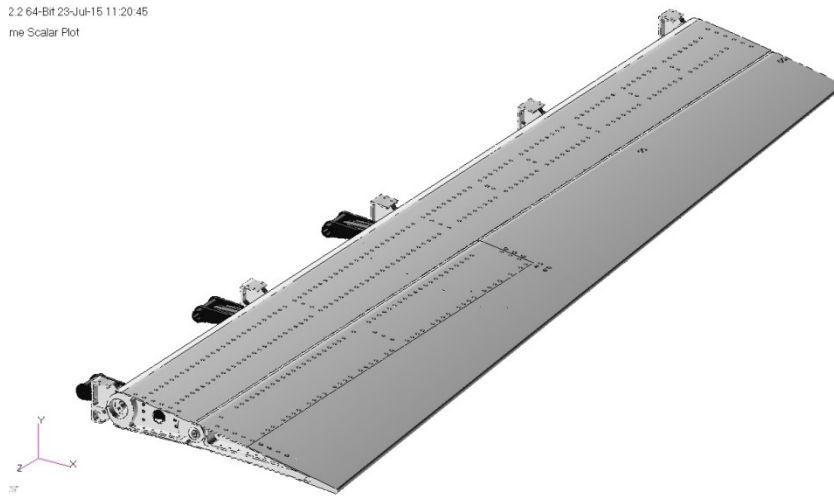


Figure 99 - FE model, materials contour plot (light grey: Al2024-T351, black: steel)



Figure 100 - FE model, materials contour plot, skin hidden, (light grey: Al2024-T351, black: steel)

3.5.4 Actuation system

The actuation system mechanism consists of a set of two linear guides, composed of a carriage and a rail in a double-sided configuration with respect to a lever beam. This arrangement resulted to be advantageous since the beam torsion is avoided and the total static force on the carriages is split in two components of lower magnitude. Moreover, the layout exhibits the highest mechanical amplification factor compatibly with the available room for the mechanism. In Figure 101 the finite element model of the first bay of aileron bay is shown together with a zoom in correspondence of the transmission mechanism. Actuator's torque is transmitted to the aileron structure by means of a fork-shaped crank and a connecting plate (Figure 102) which in turn generates a lateral forces on the beam through the contact between the linear guides carriage and its rail. The lever beam is then subjected to a pure bending stress which was evaluated by means of static analysis.

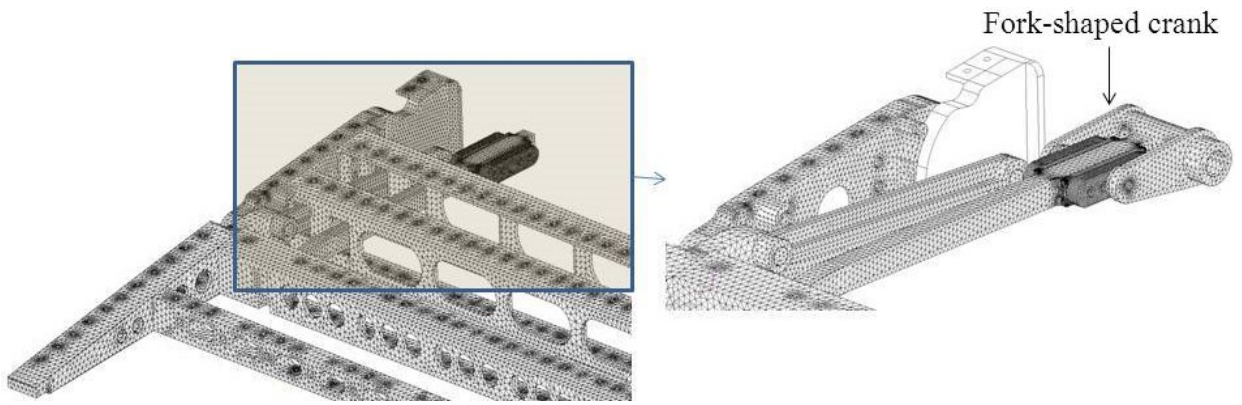


Figure 101 – Mesh of the actuation transmission chain

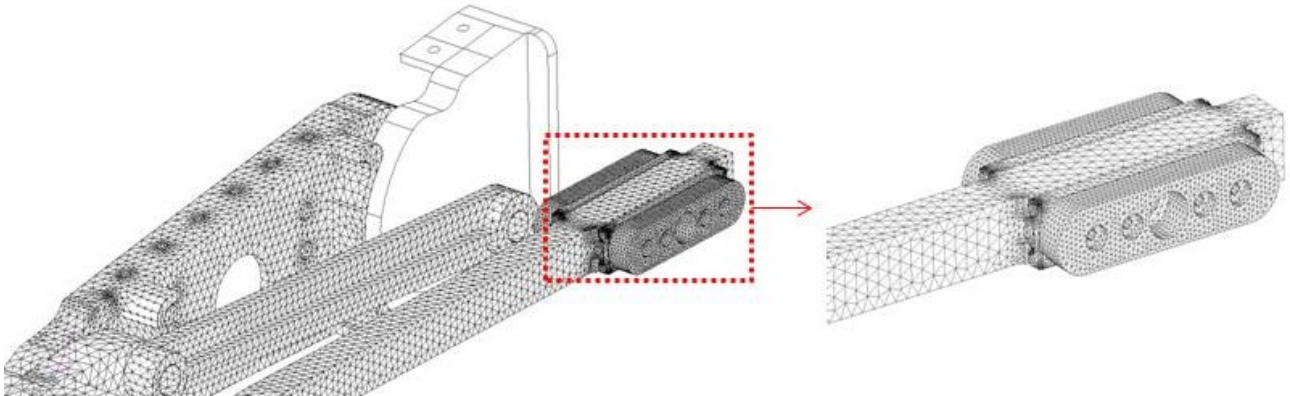


Figure 102 - Detail of the linear guides mesh

All the components of the actuation system were connected to each other by means of several pins which were simulated using CBEAM elements (Figure 103).

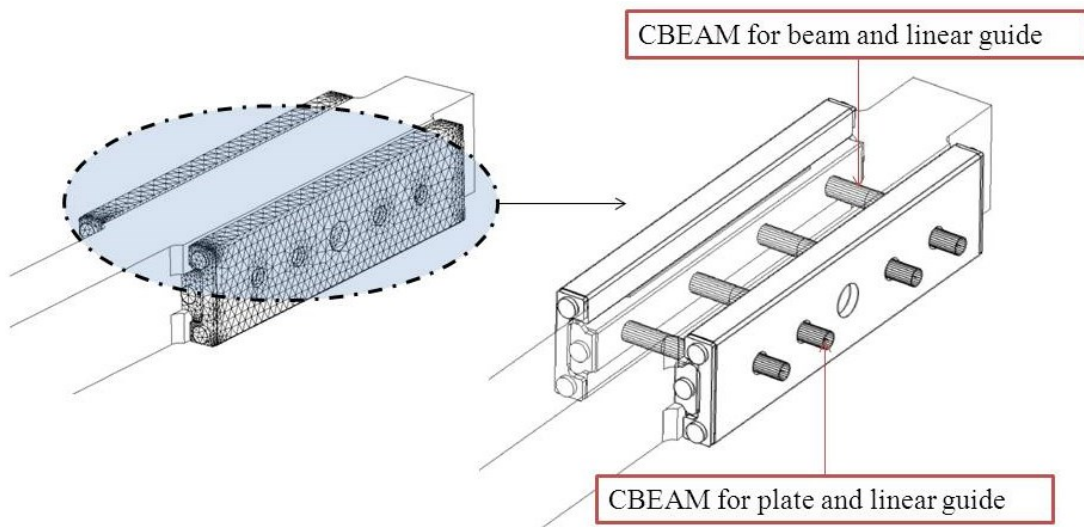


Figure 103 - Connection pins between linear guides components

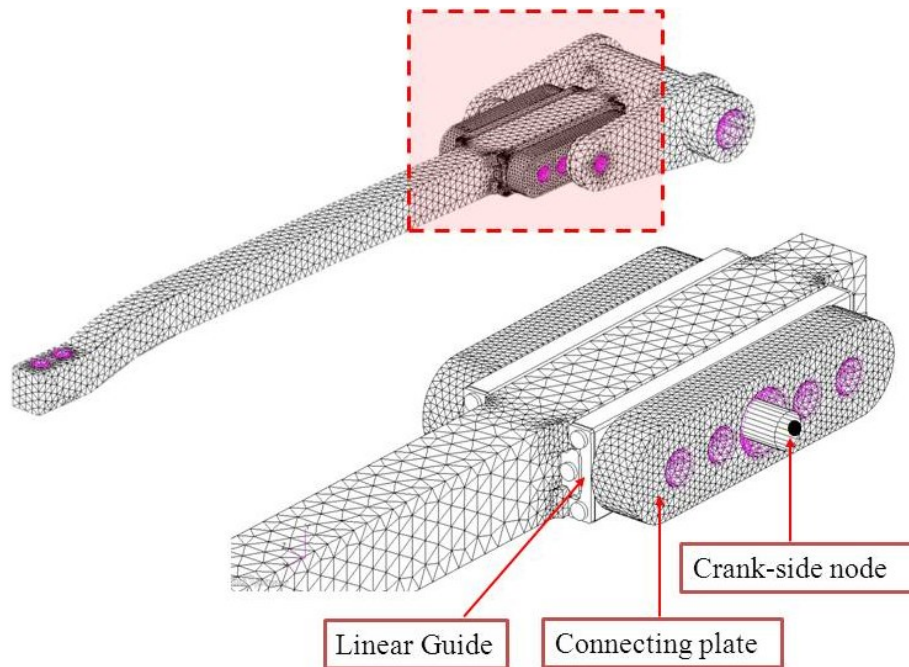


Figure 104 - Detail of the connection among the actuation transmission components

3.5.5 Joints

Hinges were modeled referring the usual scheme of rigid body connections. At each of the two sides of the hinge housing a master node is placed at the center of the circular hole, nodes on the edge of the circular node are then slaved to it through RBE2 connection. Master nodes belonging to the two sides of the hinge housing are finally joined through a CBUSH element showing low stiffness about the hinge axis. In Figure 105, the hinges connecting rib block 1 with 2 and rib block 2 with 3 are shown.

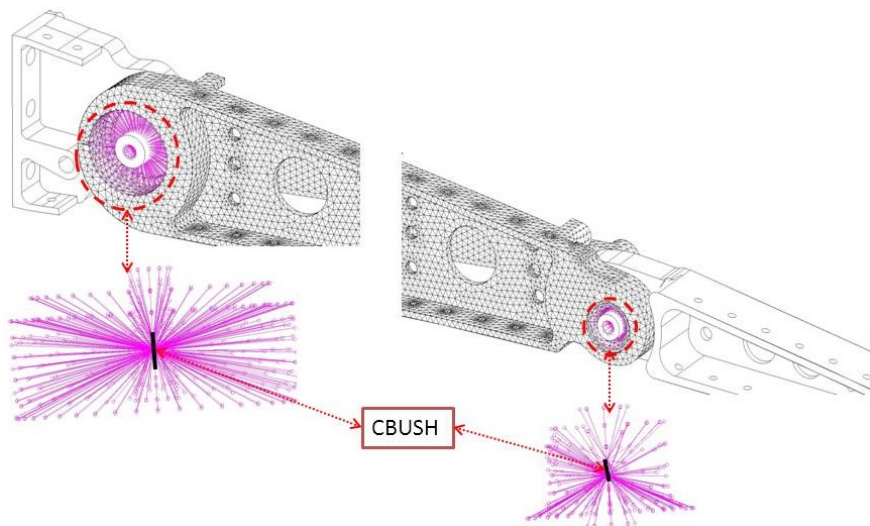


Figure 105 - Modelling approach for the hinged connection

In Figure 106, the approach used to link ribs and spars has been sketched. For each fastener (or screw) hole, a master node was generated at the center and connected to all the nodes on the edge through an RBE2 element. The fastener (or screw) was then modelled with a beam element joining the master nodes at the center of each hole.

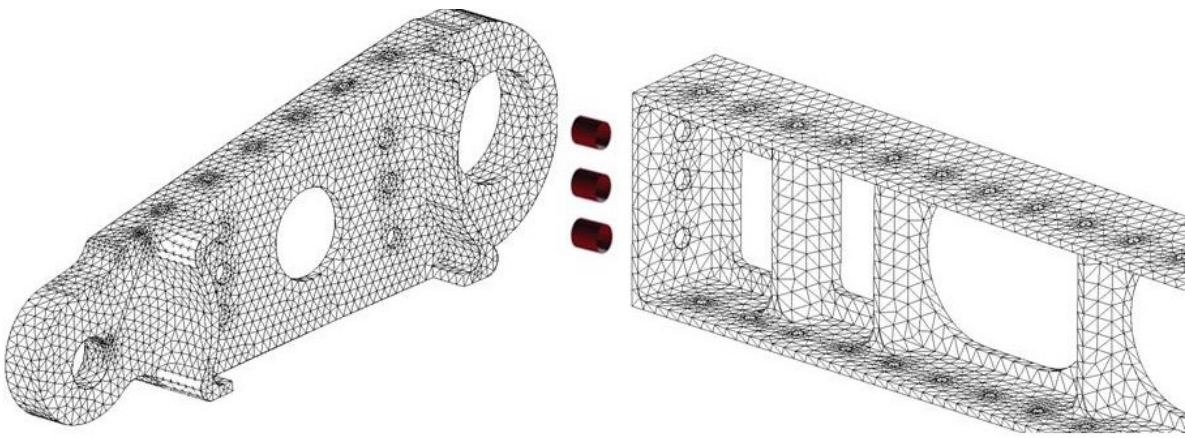


Figure 106 - Fasteners modelling approach for rib-spar connection

Finally, the same modeling-approach was used for the fastening connection between spars and skin and between rib segments and skin (Figure 107)

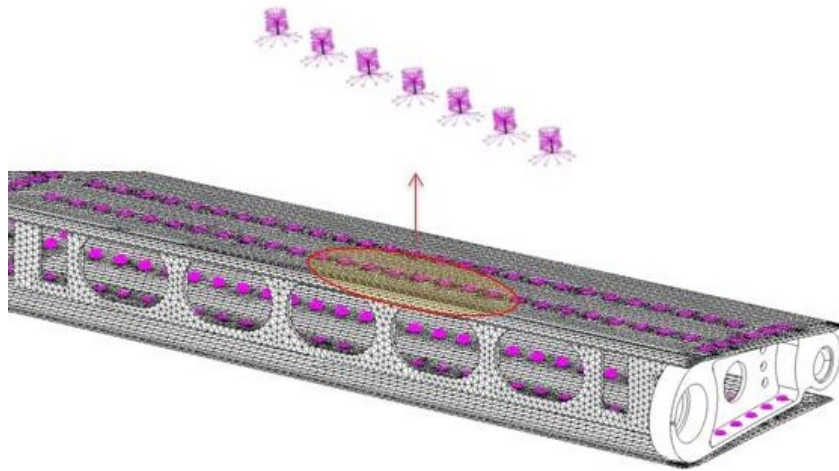


Figure 107 - Fasteners modelling approach for rib-skin and spar-skin connection

3.5.6 Design Loads evaluation

With reference to the design load described in section xx, the pressure distribution was imposed to the FE model of the aileron. In particular, for static purposes, only the last two segments were considered because the load directly affect the actuation system and they are the blocks involved during morphing while otherwise the first components is fixed to the leading edge. The pressure distribution is reported both in the contour of Figure 108 and as vector in Figure 109.

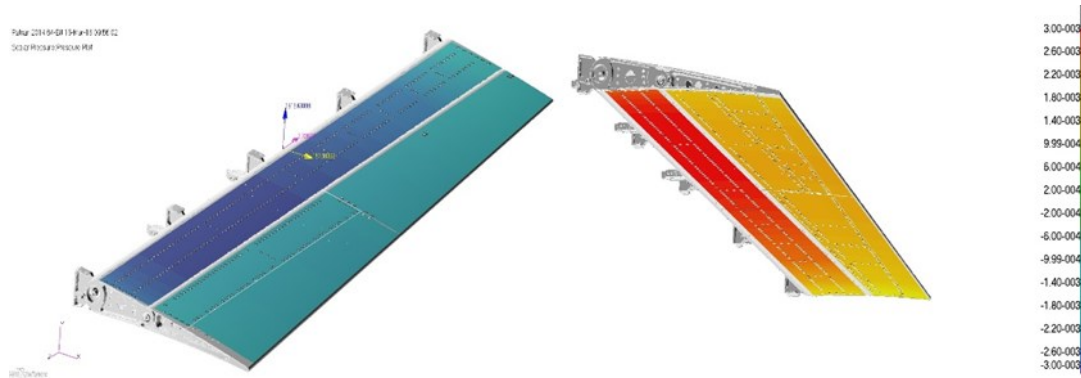


Figure 108 – Pressure distribution along the aileron

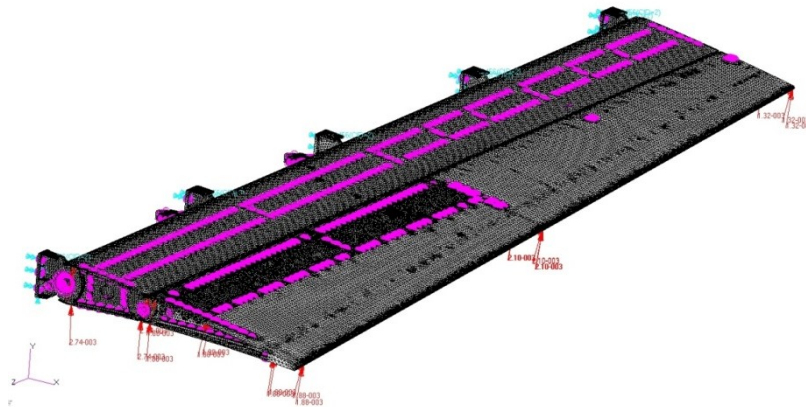


Figure 109 – Vector representation of the distributed pressure applied to the structure

The global resultant load applied on the aileron are summarised in Table 11 with reference to S1 coordinate system.

Lift [N]	Drag [N]	Side [N]
1520	160	-2.70

Table 11 – Load resultant

3.5.7 Constraint set

The first movable block of the morphing aileron was considered constrained in correspondence of its joints to the leading edge; all DOFs were suppressed to the nodes belonging to the interface region between leading edge and first block. In addition, other two different constraint sets were generated: the first one located in correspondence of the nodes on the linear guides and used to evaluate, as reaction load, the total lateral force acting on the sliding elements (Figure 110); the second one positioned on the nodes in the fork-shaped crank to simulate the locking of the actuator shaft (Figure 111).

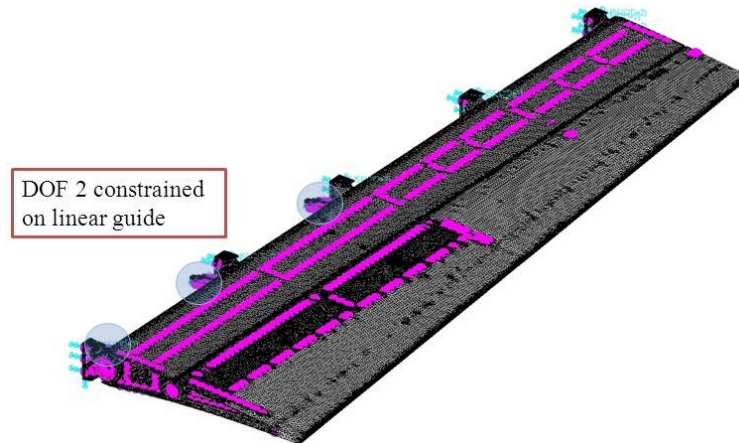


Figure 110 - Constraints along the linear guide

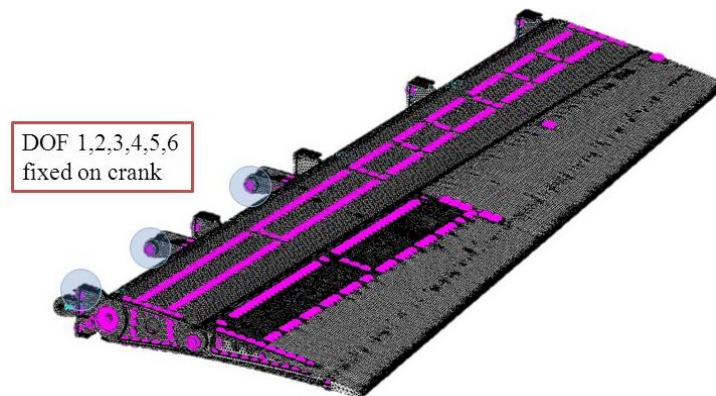


Figure 111 - Constraints on the crank

3.5.8 Static analysis at limit and ultimate load condition

Static analysis results have been here reported with reference to the limit load and ultimate load conditions. Limit loads have been defined in paragraph 3.5.6; ultimate loads were obtained by multiplying limit loads by 1.5. In Figure 112, the global magnitude of the displacements exhibited by the aileron at limit load condition is shown. The maximum value (21.8 mm) is located at the trailing edge in proximity of the 1st bay. No relevant torsion around the hinge axis was detected (Figure 112); in spite of ribs and skin segmentation, the conceived multi-box layout showed to be adequately stiff in torsion with practical no impacts on roll control effectiveness. A moderate but in any case undesirable elastic rotation of the last aileron segment about its hinge axis was observed; instead of adding stiffness to the structure, it was considered wiser to investigate about the feasibility of recovering the rotation using actuator torque. The torque required to restore the un-deflected configuration

was then calculated by means of a dedicated linear analysis carried out on the deformed shape with enforced motion of the actuator shafts. The obtained torque resulted successfully compliant with the performances of several actuators available in commerce; moreover the recovery of the un-deflected configurations occurred without any local increase of stress.

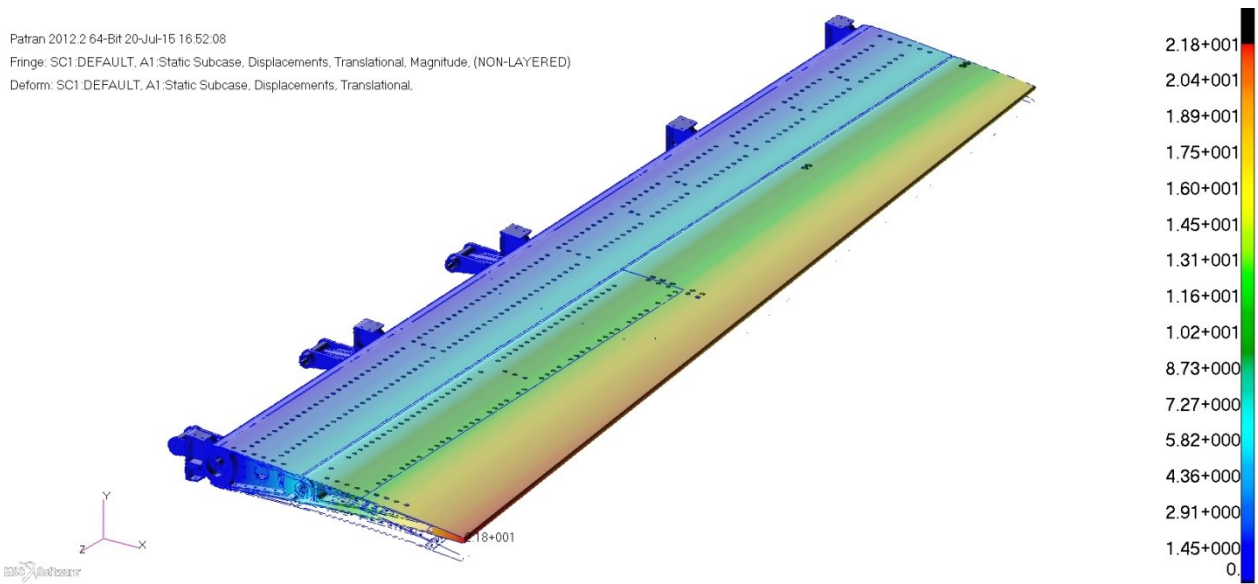


Figure 112 - Global aileron displacement distribution at LL condition

In Figure 113, the same results are shown with a focus on the primary structure (skin hidden).

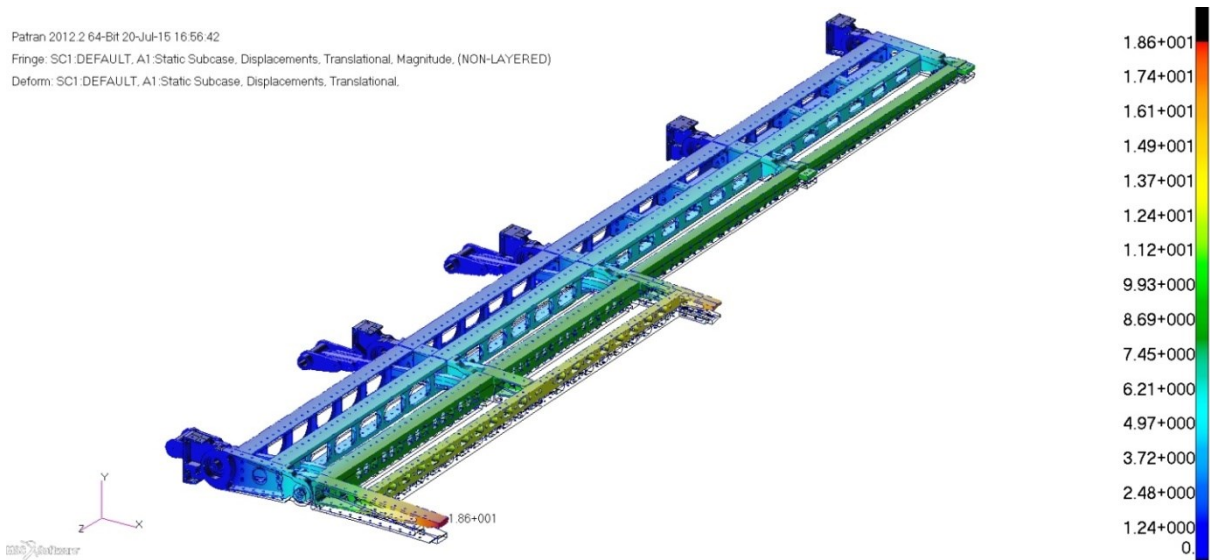


Figure 113 - Global aileron displacement distribution LL condition (skin hidden)

The stress distribution along main structural components is shown in Figure 114 - Figure 120.

Patran 2012.2 64-Bit 20-Jul-15 16:58:04
 Fringe: SC1 DEFAULT, A1-Static Subcase, Stress Invariants, Von Mises, (NON-LAYERED)
 Deform: SC1 DEFAULT, A1-Static Subcase, Displacements, Translational.

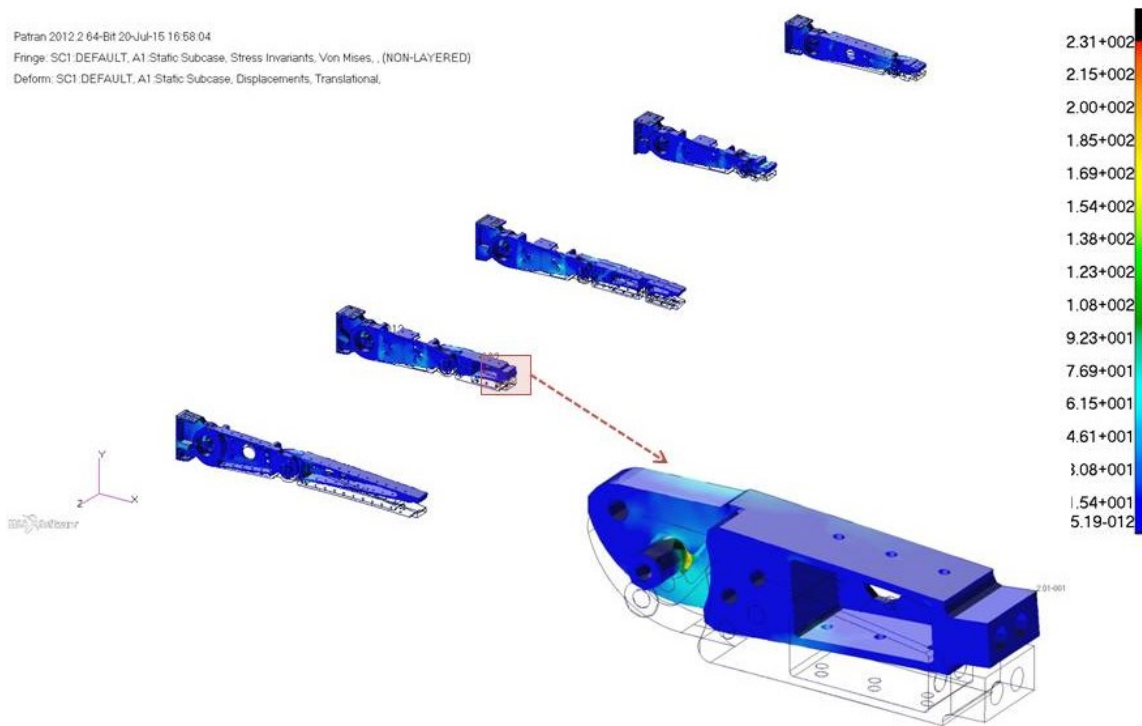


Figure 114 – Global VM stress distribution on ribs at LL condition

The maximum stress on the ribs occurs at the third block of the rib 2 and it is equal to 231 MPa (see figure above). It is localized in a very small area around the hinge connecting block 3 with block 1. The elements with stress level higher than 150 MPa are also shown in Figure 115. This result indicates that a rapid stress reduction occurs while moving away from the hinge axis.

Patran 2012.2 64-Bit 20-Jul-15 17:01:06
 Fringe: SC1 DEFAULT, A1-Static Subcase, Stress Invariants, Von Mises, (NON-LAYERED)

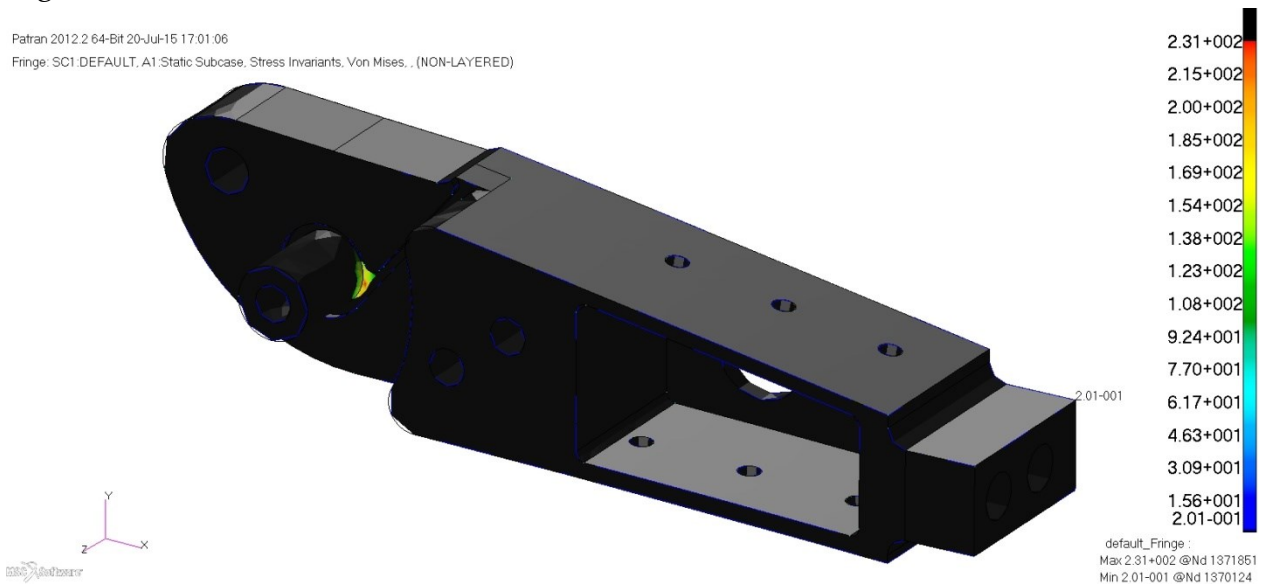


Figure 115 – Element Stress Distribution above the threshold of 150 MPa

For what regards the rib links, the highest VM stress arises in correspondence of the element connected to the third block of rib 4; however the stress value (257 MPa) is well below the yield stress of link material (steel, ~ 1000 MPa).

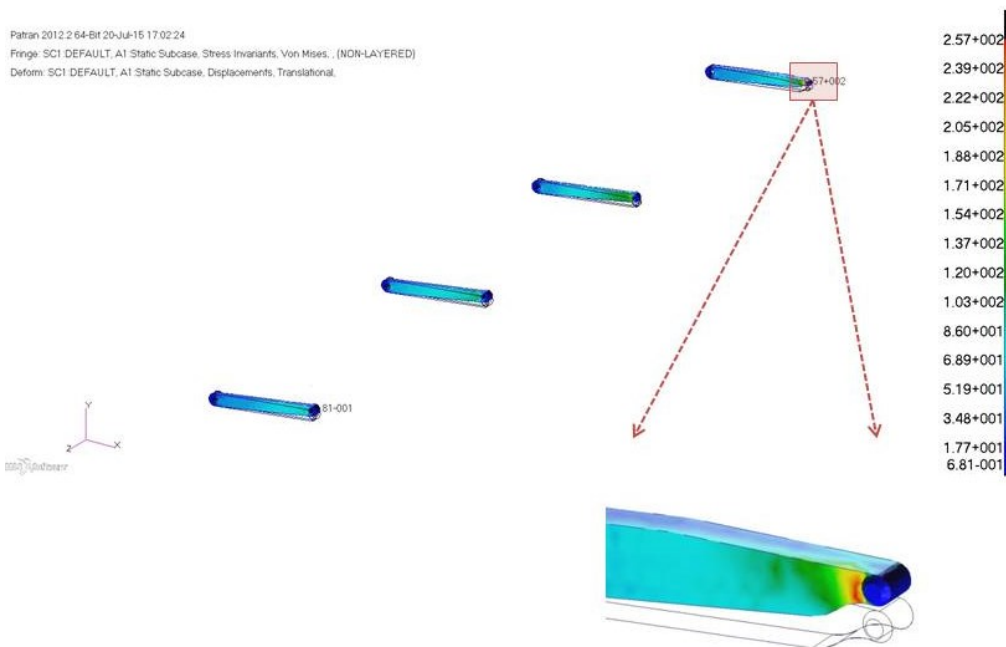


Figure 116 – Global VM stress distribution on links at LL condition

The VM stress distribution on the spars is shown below. The elements are not particularly stressed, with the exception of localized areas around the hole between the spar and the rib 5 at aileron tip. The value is close to the yield stress of AL 2024 in a very small region.

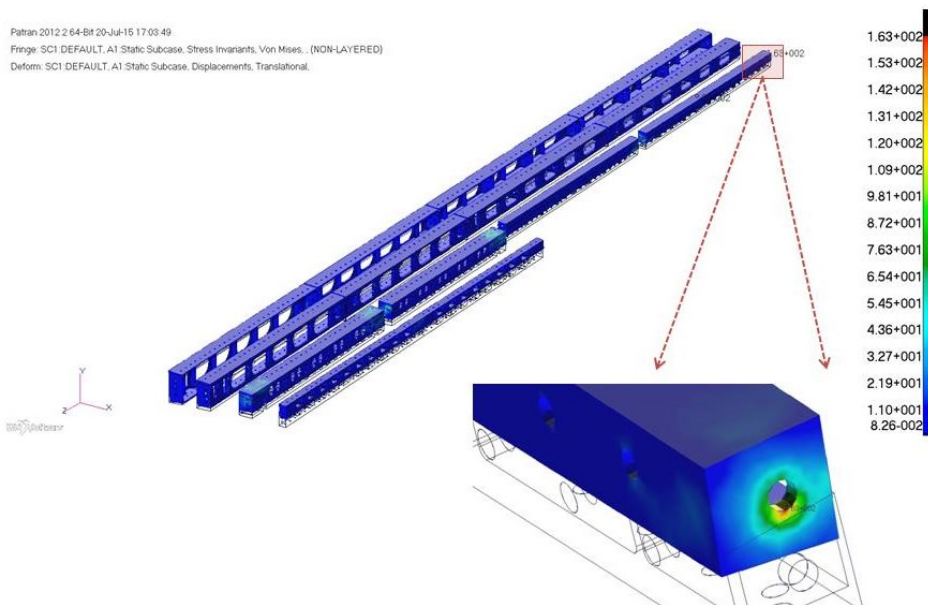


Figure 117 – Global VM stress distribution on spars at LL condition

Stress values along the skin resulted instead globally uniformly distributed with values well below the aluminium yielding except some (small) peaks around the fasteners (Figure 118). As shown for the rib components, the low level of solicitation of the aileron structures is related to the fact that the most of the external load is withstood by the internal actuation mechanism, leverage and actuators.

Patran 2012.2 64-Bit 20-Jul-15 17:06:02
 Fringe: SC1.DEFAULT.A1:Static Subcase, Stress Invariants, Von Mises, (NON-LAYERED)
 Deform: SC1.DEFAULT.A1:Static Subcase, Displacements, Translational.

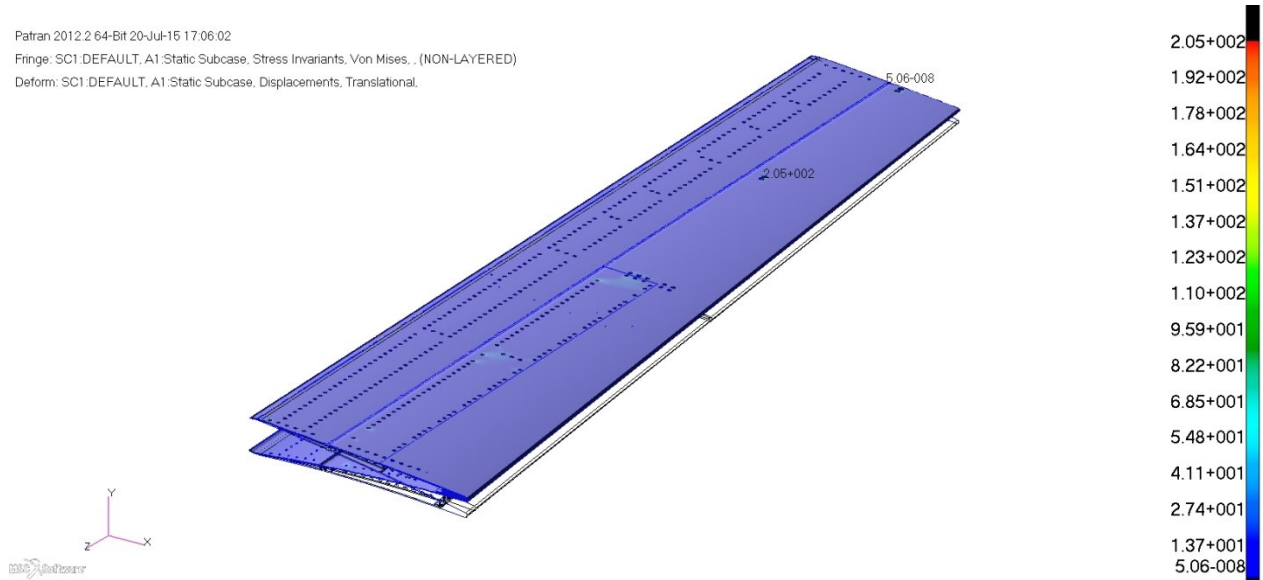


Figure 118 – Global VM stress distribution on skin at LL condition

Actuation levers showed the typical stress distribution of the beams in bending; stress peaks greater than 350 MPa were found close to un-chamfered notches (Figure 119).

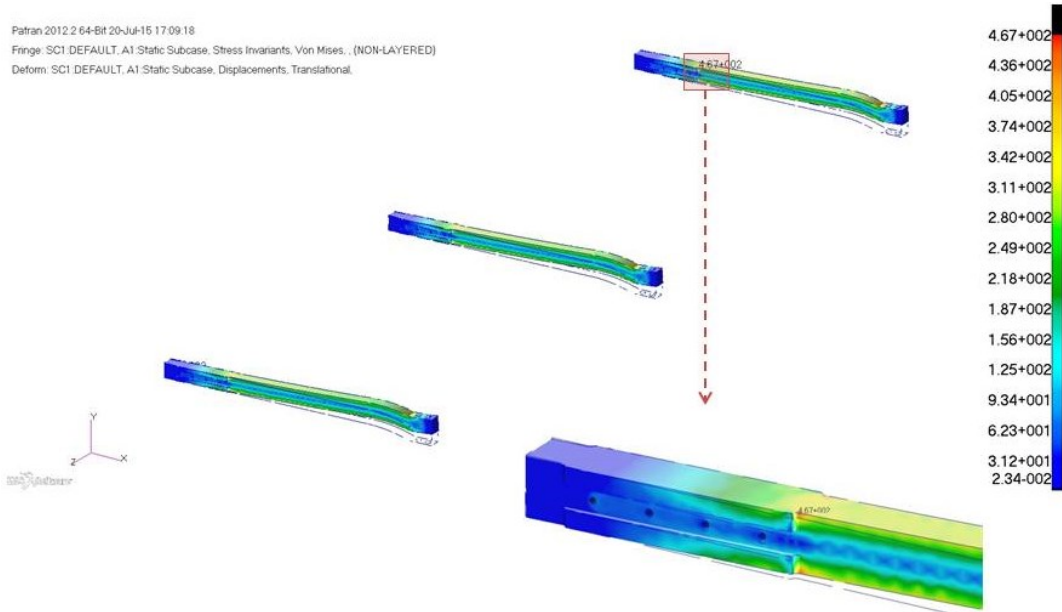


Figure 119 – Global VM stress distribution on Actuation Beam at LL condition

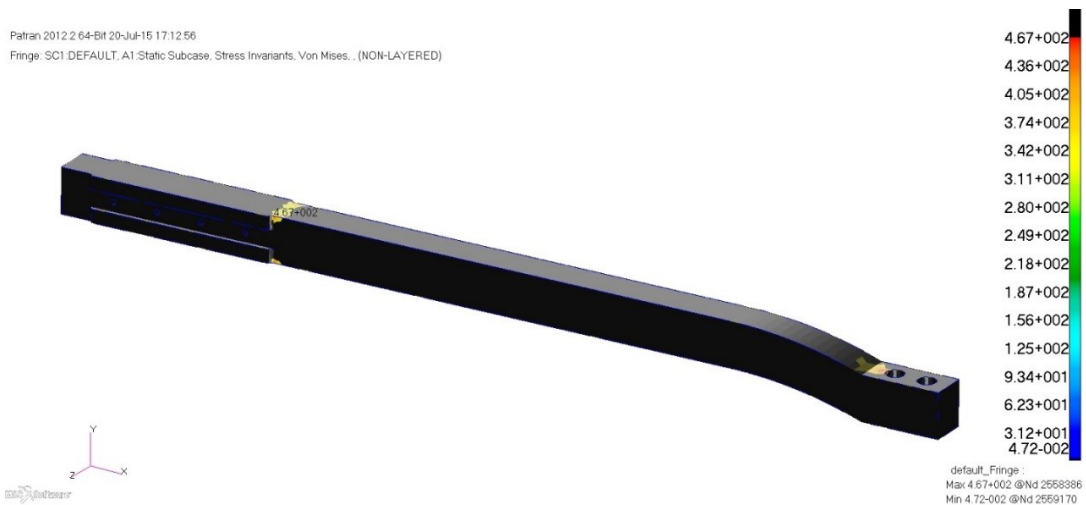


Figure 120 – Beam element stress distribution above threshold values of 320 MPa

The stress distribution on the linear guide component are reported in the next Figure 121 with slider in transparency. The larger extent of the constraints (additional clamps) is expected to lead to higher stresses, locally (in the contact region) and distributed (overall).

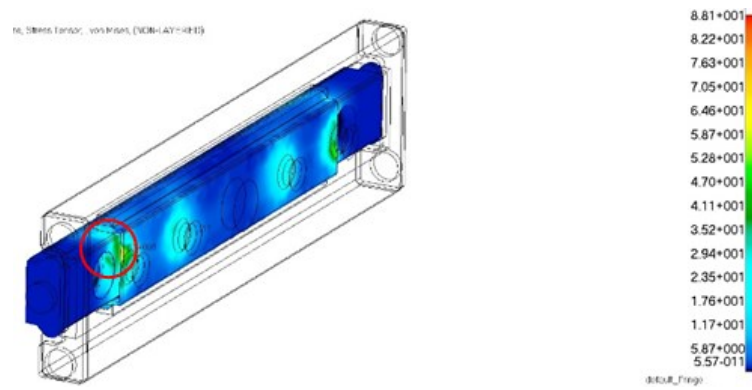


Figure 121 – Von Mises Stress distribution around the most solicited linear guide.

Margin of safety with respect to local plasticization (/failure) at limit (/ultimate) load have been recapped in Table 12(/Table 13) for each component type.

Part	F_{ty} [MPa]	f_{ty} [MPa]	MS_{LL}	Stress contour
Rib	324	231	0.40	
Link	520	257	1.02	
Spar	324	163	0.98	
Skin	324	205	0.58	
Actuation beam	520	467	0.11	

Table 12 - MoS with respect to local plasticization at LL condition

Part	F_{tu} [MPa]	f_{tu} [MPa]	MS_{UL}
Rib	469	346.5	0.35
Link	900	385.5	1.33
Spar	469	244.5	0.918
Skin	469	307.5	0.525
Beam	900	700.5	0.28

Table 13 - MoS with respect to failure at UL condition

3.5.9 Reaction loads at wing box interface

In order to evaluate the reaction loads at wing box interface, the finite element model described in paragraph 3.4.2 was completed with the mesh of the aileron leading edge as well as of all those elements assuring its connection to the wing box. Aileron hinge axis was virtually reproduced by adopting specific constraint conditions implemented with reference to the coordinates system¹ depicted in Figure 122; tie-rods were fully modelled and their bases were rigidly connected to master nodes in turn constrained in all DOFs (grids 4820028, 4813397, Figure 122). Hinges at root and tip ribs, as well as in correspondence of tie-rod heads, were modelled by using the same approach described in paragraph 3.4.5.

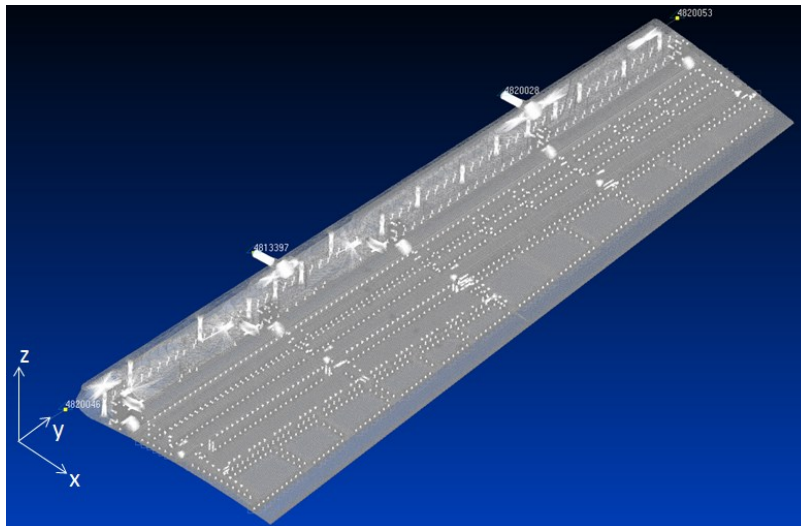


Figure 122 - FE model used for the evaluation of reaction loads at wing box interface

Master grids at root and tip hinges locations (namely grids 4820046 and 4820053, Figure 122) were respectively constrained in DOFs 123456 and 12346. Linear static analysis was then carried out and limit reaction loads were finally evaluated.

GRID	T1 [N]	T2 [N]	T3 [N]	R1 [Nm]	R2 [Nm]	R3 [Nm]
4813397	-6.9792E+2	0.0	-5.1779E+2	3.6005	4.3742E+1	-1.2532
4820028	1.6819E+2	0.0	-4.5130E+2	5.7469	2.5147E+1	1.4515E+1
4820046	1.7739E+2	0.0	-3.0889E+2	-1.3898	3.0719E+2	5.7412E-1
4820053	-7.9091E+2	0.0	-7.8816E+1	3.1102	0.0	-2.8114

Table 14 - Reaction loads at wing box interface (limit condition)

¹ Y axis along aileron hinge axis, XZ plane parallel to root rib plane.

3.5.10 Reaction loads on linear guides

In order to evaluate the actuator torque required to equilibrate aerodynamic loads at limit condition ($Mach = 0.25$, $\alpha = 0^\circ$, $\delta = 0^\circ$, $\gamma = 7^\circ$), the reaction loads acting on the linear guides were estimated for each actuation chain. The estimated lateral forces and the corresponding torque are reported in Table 15. The first column identifies the FE model nodes where the reaction loads were calculated. The vertical forces are reported in the second column and the torque in the third one. The torque was obtained by multiplying the force by its distance from the hinge axis of the rib block, the result was then divided by the mechanical advantage.

Node ID	Lateral Force [N]	Actuator Torque [Nm]
2634247	297.14	12.15
2634246	260.47	
2634245	282.72	12.17
2634244	275.58	
2634243	277.70	12.88
2634242	313.41	

Table 15 - Actuator torque evaluation

Each reaction force resulted well below the allowable static load of the linear carriage (1091 N) as prescribed by the producer. Also the actuator torque resulted below the peak torque of 13 Nm.

3.5.11 Checks on joints

Joints were verified with respect to failure by shear, tension, shear plus tension and bearing at ultimate loads. The equations reported in [43] and recapped below were used; relevant forces for MoS computation were extracted from FEM in correspondence of ultimate loads; no criticality was found and all joints resulted characterized by MoS greater than 3.

Fastener shear check:

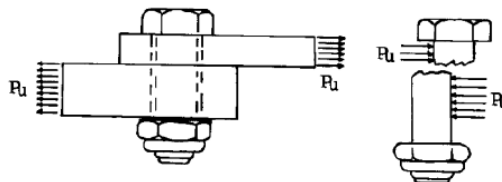
$$MS_{shear} = \frac{S_{all}}{1.5 * S_a} - 1 \quad (9)$$

Where $S_{all} = F_{su} * A$

F_{su} is the ultimate shear stress of bolt material

A is the cross section area of bolt

S_a is the applied shear load



Fastener tension check:

$$MS_{shear} = \frac{T_{all}}{1.5 * T_a} - 1 \quad (10)$$

Where $T_{all} = F_{tu} * A$

F_{tu} is the ultimate tensile stress of bolt material

A is the cross section area of bolt

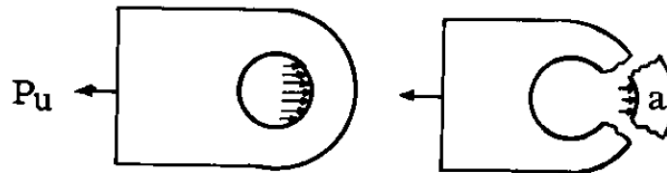
T_a is the applied tensile load

Fastener shear + tension check:

$$\frac{(1.5 * S_a)^3}{S_{all}^3} + \frac{(1.5 * T_a)^2}{T_{all}^2} < 1 \quad (11)$$

Bearing check:

$$MS_{bry} = \frac{P_{bry}}{S_a} - 1 \quad MS_{bru} = \frac{P_{bru}}{1.5 * S_a} - 1 \quad (12)$$



Where $P_{bry} = F_{bry} * D * t$

F_{bry} is the bearing yield strength

F_{bru} is the bearing ultimate strength

D is the bolt diameter , t is the plate thickness

The margin of safety for each connection are reported in Table 16.

Fastener Check					
Location	MSshear	MStens	MSCOMBINED	MSBRY	MSBRU
Skin to Structure	HIGH	HIGH	OK	HIGH	HIGH
Spar to Rib	0.082	HIGH	OK		
Actuation Beam to Spar	HIGH	0.470	OK	HIGH	HIGH

Table 16 - Table of MoS for connections

3.5.12 Buckling analysis at limit condition

Buckling analysis was carried out in correspondence of limit loads only. No buckling occurs at limit load; the first buckling eigenvalue was found equal to -10.4 and the corresponding eigenvector shows the instability of all crossed links between the third rib block and the aileron leading edge (Figure 123).

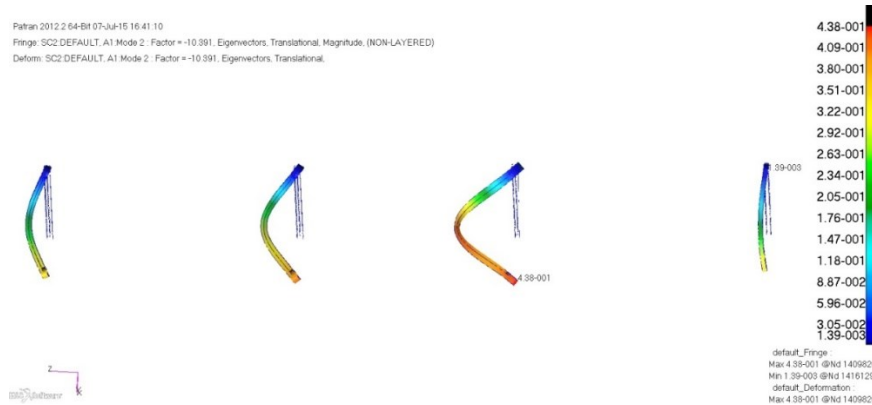


Figure 123 - First buckling mode (instability of rib links, eigenvalue: -10.4, ref. loads: LL)

3.6 Aeroelastic Stability Analysis

The present chapter concern the preliminary aeroelastic study conducted on the morphing aileron. It was firstly conducted in the work [45] and summarized in [46]. Moreover the results obtained numerically have been validated by experimental GVT on the morphing aileron. In order to assure the safety of WTT campaign, the aeroelastic behavior of the T/A was investigated and clearance from any dynamic instability (flutter) was demonstrated up to 1.2 times the maximum flow speed expected during tests. The analysis consist of four main steps:

- evaluation of the T/A theoretical modes (with reference to the real wind tunnel constraint conditions);
- generation of T/A aerodynamic lattice;
- interpolation of modes on aerodynamic lattice and GAF evaluation;
- flutter analysis by theoretical modes association.

The aeroelastic analysis was carried out by means of the AELAB-software. With reference to the already described wing model (section 3.1), the imposed constraint conditions are important for assure correct results from the aeroelastic analysis. The aileron finite element model was assembled to a FE model of the wing box in order to evaluate the normal modes of the entire T/A. The model is at high level of detail reproducing with accuracy the hinged connection between the aileron and the wing box as well as the external mechanical system for aileron actuation. As first step, the modal analysis on the morphing aileron has been carried out showing the main modal parameters such as modal shapes, frequencies and generalized masses. These results will be used to create a database necessary to perform the aeroelastic stability analysis. Then a complete aeroelastic model will be assessed to analyze the dynamic behavior of the complete T/A to avoid instabilities during wind tunnel tests. Moreover also the effect of a variable stiffness of the external linear mechanical actuator on

the modal parameters will be considered. Real eigenvalue extraction have been performed with Lanczos Method in the frequency range 0-80 Hz. Method for normalizing eigenvectors will be the maximum (i.e. NORM=MAX) which normalize to unit value of the largest displacement in the analysis set. Due to the basic difference if compared with the conventional aileron, it will expected unconventional modal shapes for the morphing one. The main results are reported in Table 17. The morphing aileron has been constrained in four grids. Master nodes of tie-rods' MPC are constrained in all 6 DOFs, while root and tip nodes of the shaft allow aileron rotation about hinge-line. The modes are depicted from Figure 124 to Figure 127.

Order	Freq [Hz]	Gen. Mass [kg*m^2]	Modal Shape	Notes
1	0.0026	0.4046	Figure 124	Fundamental aileron mode
2	41.379	0.0148	Figure 125	Morphing Aileron mode
3	58.774	0.0357	Figure 126	I torsional mode
4	120.27	0.0236	Figure 127	II torsional mode

Table 17 – Morphing aileron modal analysis: freq. and generalized masses

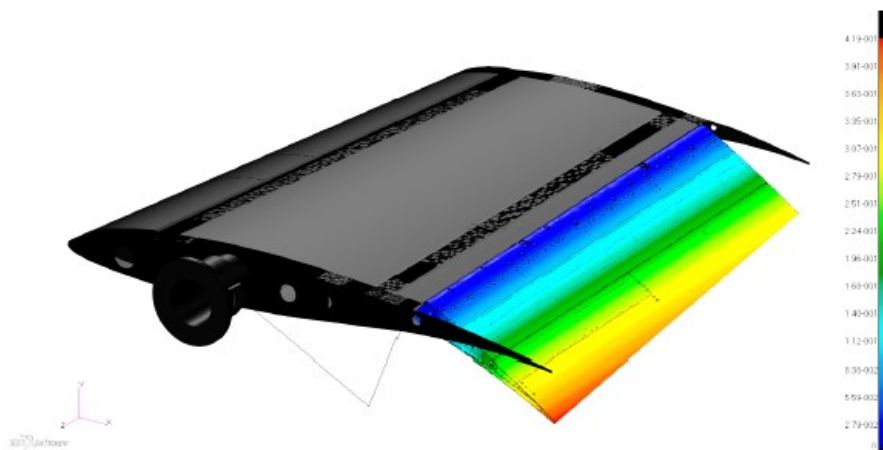


Figure 124 – Mode 1: freq = 0.0026 Hz.

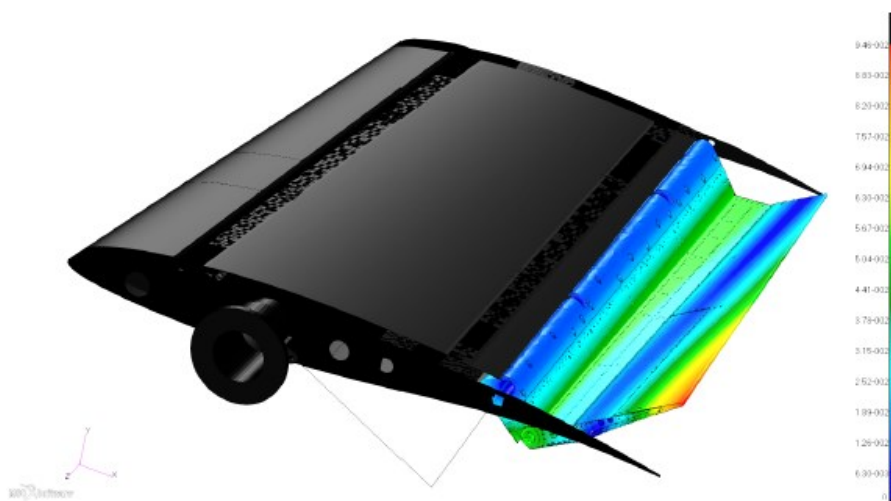


Figure 125 – Mode 2: freq=41.379 Hz

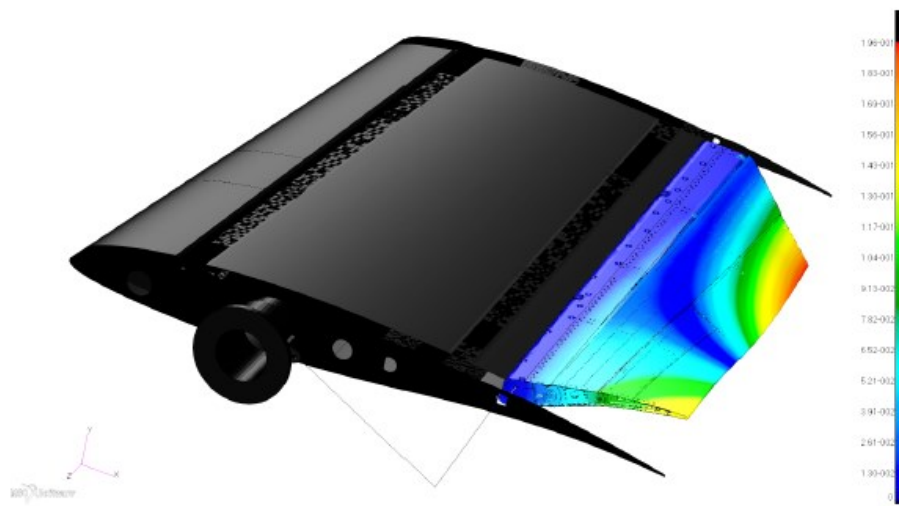


Figure 126 – Mode 3: freq = 58.774 Hz

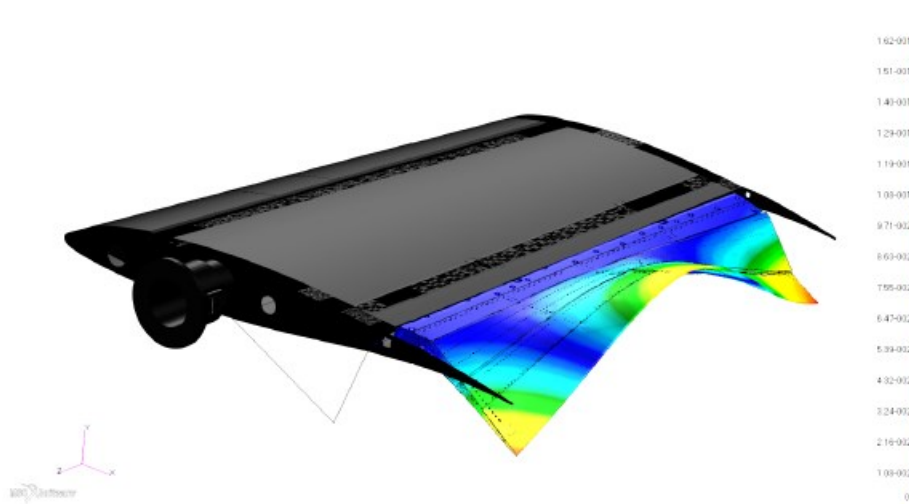


Figure 127 – Mode 4: freq = 120.27 Hz

It can be seen that first mode, also called fundamental, is a typical free rigid rotation of the aileron around the hinge-line, because the modal frequency is nearly zero, and translational eigenvectors increase linearly from hinge-line. Moreover, the generalized mass of the first mode is almost coincident with the moment of inertia about the aileron hinge axis, $I_y = 0.403 \text{ kg} * \text{m}^2$ (Figure 124 Figure 125). The second mode is a typical mode of a morphing surface (Figure 125). This mode is not expected for usual aileron, which otherwise exhibit a torsional mode to higher frequencies. Finally the third and the fourth frequencies (Figure 126 & Figure 127) represent the torsional modes around X-axis and they occur at high frequency due to aileron elevated torsional stiffness. Unina provides also the structural model of the complete T/A that will be further assembled with the aileron finite element model in order to evaluate the normal modes of the prototype necessary for the aeroelastic analysis. On the base of the wing box geometry furnished by the Canadian team, the CAD was simplified and adjusted in order to achieve high mesh quality. A general overview of the wing box mesh is provided in Figure 128.

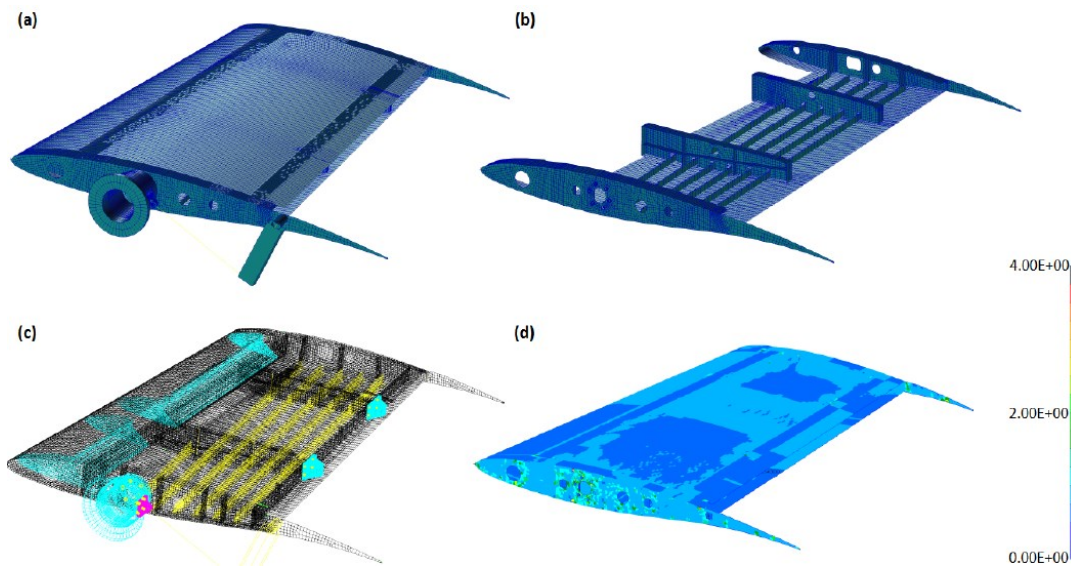


Figure 128 – Wing box mesh: (a) complete model, (b) upper skin and support hidden, (c) wireframe view, (d) Jacobian ratio

All the mesh characteristics are reported in Table 18.

ELEMENT TYPE	NUMBER OF ELEMENTS	REFERENCE ITEM
CBEAM	475	Morphing skin actuators / joints between the root rib and the T/A support
CROD	1	External Actuator (for rigid aileron deflection)
CQUAD4	39563	Skin
CTRIA3	64	Skin
CHEX	29933	Leading Edge core and T/A support
RBE2	14	Joints between the root rib and the T/A support / joints between morphing skin actuators and structure

Table 18 – Wing box FEM elements summary

As reported in the previous table, the external actuator was modelled through a rod element linked to the T/A support and to the lever arm of the aileron hinge axis (Figure 6.2). Four different values for the linear stiffness of the actuator were taken in account (Table 19) in order to assess the aeroelastic stability of the T/A with respect to changes in control surface harmonics. Actuator stiffness was modified by working on the Young modulus of the rod material according to the following equation:

$$E = KL/A \quad (13)$$

Where:

- L is the length of the actuation rod simulating the actuator;
- A is the section of the actuation rod simulating the actuator;
- K is the value assigned to the actuator stiffness.

K [N/m]	E [N/m ²]
5.0 E+04	6.80 E+06
1.0 E+05	1.36 E+07
1.5 E+05	2.04 E+07
2.0 E+05	2.72 E+07

Table 19 – Actuator Stiffness

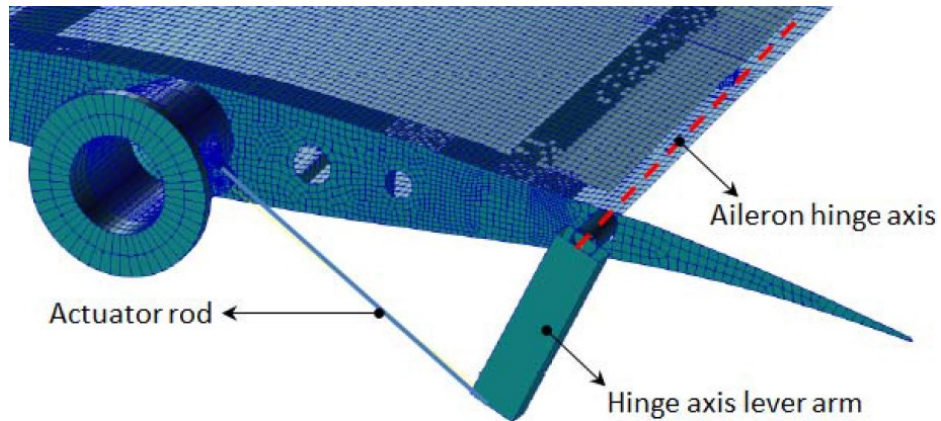


Figure 129 – Actuator model

Modal analysis in absence of actuator rod connection was preliminarily carried out and FE model capability to reproduce aileron fundamental (0 Hz aileron rigid mode) was positively checked. For this preliminary check and for all the analysis reported in this document, T/A support was constrained coherently with the bolted connection to the wind tunnel floor. The aeroelastic analysis requires the computation of unsteady AIC matrices that were evaluated by means of DLM ([47]); aerodynamic grid was characterized by 6 flat panels (Figure 130) representative of:

- wing box (3 panels, P1: inner wing region, P2: mid wing region, P3: outer wing region);
- morphing aileron (3 panels, P4-P6, one for each movable segment).

Each panel was divided into strips and every strip split up into boxes. In fact, the aileron panels was modeled aiming at having a finite number of boxes strip-wise per each aileron block in this way, it was better estimated the aerodynamic behavior of the morphing aileron. The aileron panel has three macro-areas, indicated with thick lines in Figure 130, which represent the three blocks of the morphing structures.

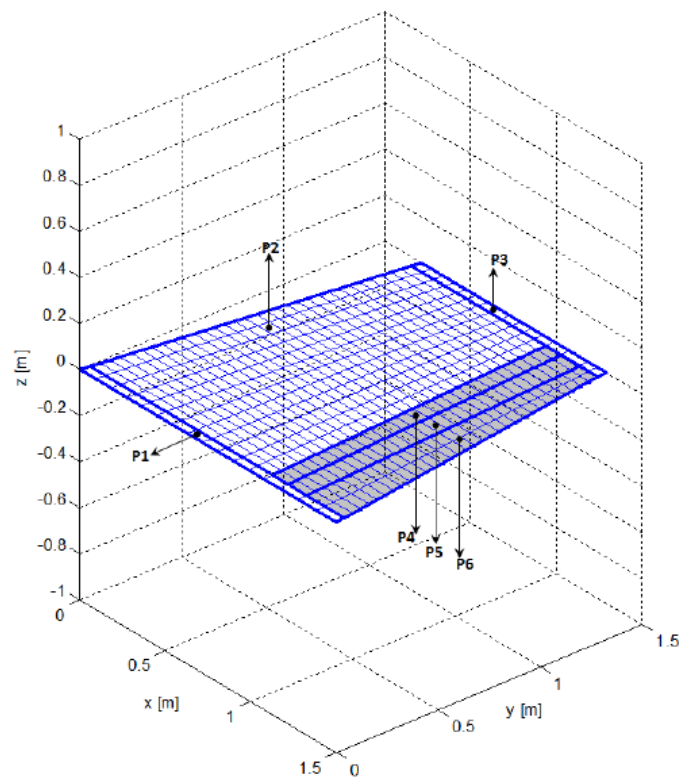


Figure 130 – T/A aerodynamic lattice

The aileron structural model was realized for static analysis purposes and not for aeroelastic stability analysis because of its large number of nodes ($3.6 * 10^6$). Therefore, it was necessary to select several nodes from the structural model from whose the modal eigenvectors could be reconstructed. Displacement induced by elastic modes along the normal of each aerodynamic box, were obtained through *surface spline interpolation* of the modal displacements at several FEM grids. The structural grid point locations on the aerodynamic lattice used for modes interpolation are marked in red in Figure 131.

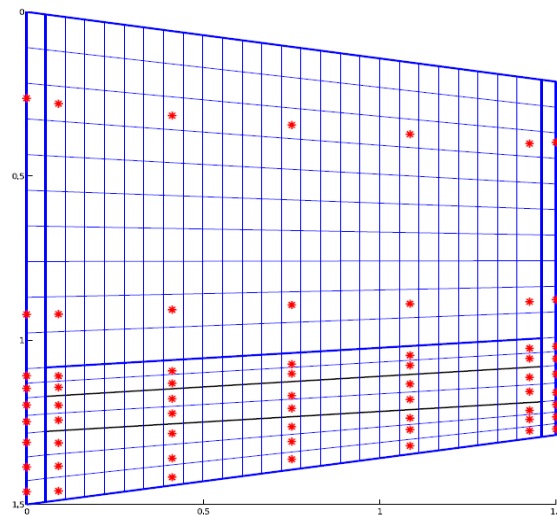


Figure 131 – Interpolation grid on aerodynamic model.

In the next figure, the output of the modes interpolation has been graphically sketched with reference to the displacement field induced by the aileron harmonic (Figure 132).

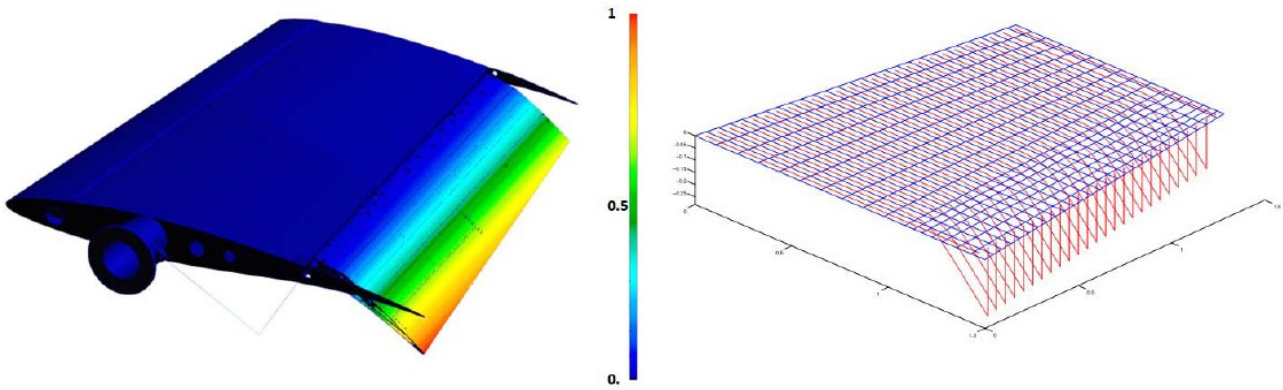


Figure 132 – Aileron Harmonic: modal displacement on structural model (left), interpolation on aerodynamic grid (right)

The aeroelastic stability analysis of the T/A was investigated under the following working assumptions:

- a) PK-continuation method ([47]) for the evaluation of modal frequency and damping trends versus flight speed;
- b) theoretical elastic modes association in the frequency range 0Hz-80Hz (elastic modes being pertinent to T/A constraint condition expected during tests);
- c) modal damping equal to 0.01 for all the elastic modes;
- d) sea-level altitude, airflow speed range 0-2 V_M , V_M being the maximum airflow speed expected during WTT ($V_M=85.0$ m/s);
- e) morphing aileron actuators in power-on configuration (fixed value of rotational stiffness at internal actuators' shafts);
- f) external actuator stiffness according to the values reported in Table 19, section 3.1.

Depending on the value of the external actuator stiffness (K), the following results were obtained (Table 20).

CASE ID	K [N/m]	V_F [m/s]	V_F/V_M	Flutter Mode ID (frequency)	REF. V_g plot
1	5.0 E+04	146.081	1.719	3 (22.53 Hz)	Figure 133
2	1.0 E+05	115.724	1.361	3 (22.59 Hz)	Figure 134
3	1.5 E+05	111.353	1.310	3 (22.60 Hz)	Figure 135
4	2.0 E+05	109.872	1.293	3 (22.60 Hz)	Figure 136

Table 20 – Flutter analysis results

For all the investigated cases, flutter of mode 3 (aileron tab mode, see Figure 137 - right) was detected always at speed higher than $1.2V_M$. In order to isolate the minimal modal association causing flutter, modal participation factors into flutter mode were determined at flutter speed. The instability was found to be essentially due to a typical ternary mechanism characterized by the coalescence of modes 1 (aileron harmonic, Figure 137 - left) and 3, *sustained* by mode 2 (T/A bending, Figure 137 - centre). As external actuator stiffness increases, the frequency of the aileron harmonic gets closer to the one of the flutter mode (practically constant at 22 Hz) thus anticipating the coalescence at a lower speed values (Table 20). On the other hand, the trend of the flutter speed vs. the parameter K (Figure 138)

shows an asymptotical stabilization at around 108 m/s for $K \rightarrow \infty$; this means that the flutter speed keeps to be greater than $1.2 V_M$ also in correspondence of K values greater than the ones covered by the addressed analysis cases.

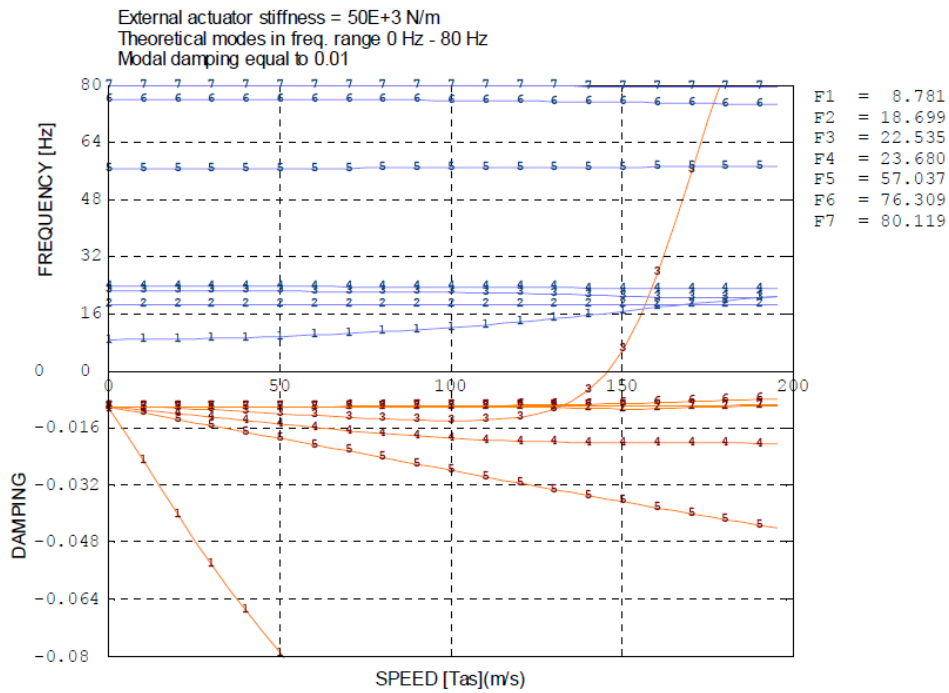


Figure 133 - Vg plot for case 1

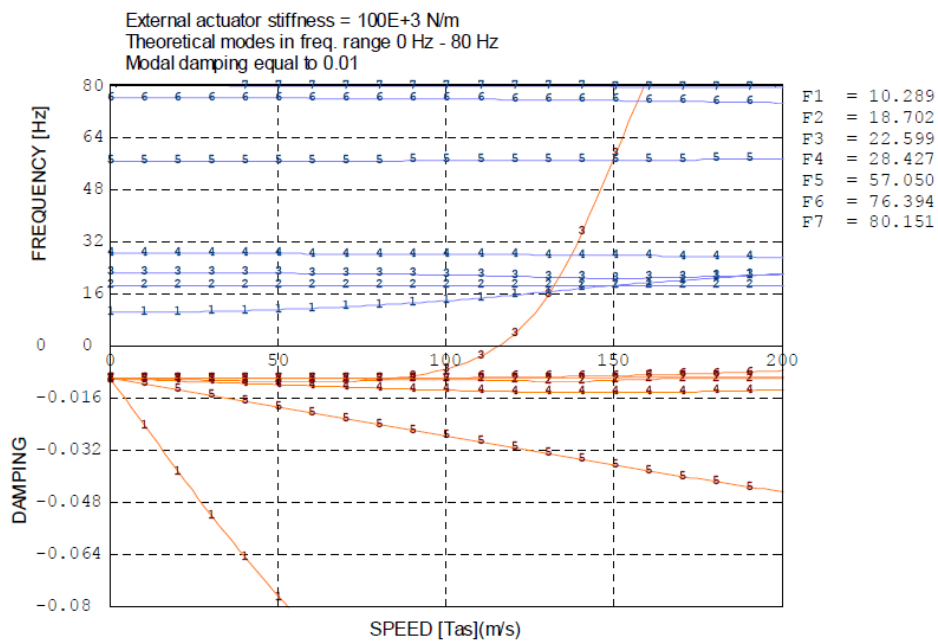


Figure 134 - Vg plot for case 2

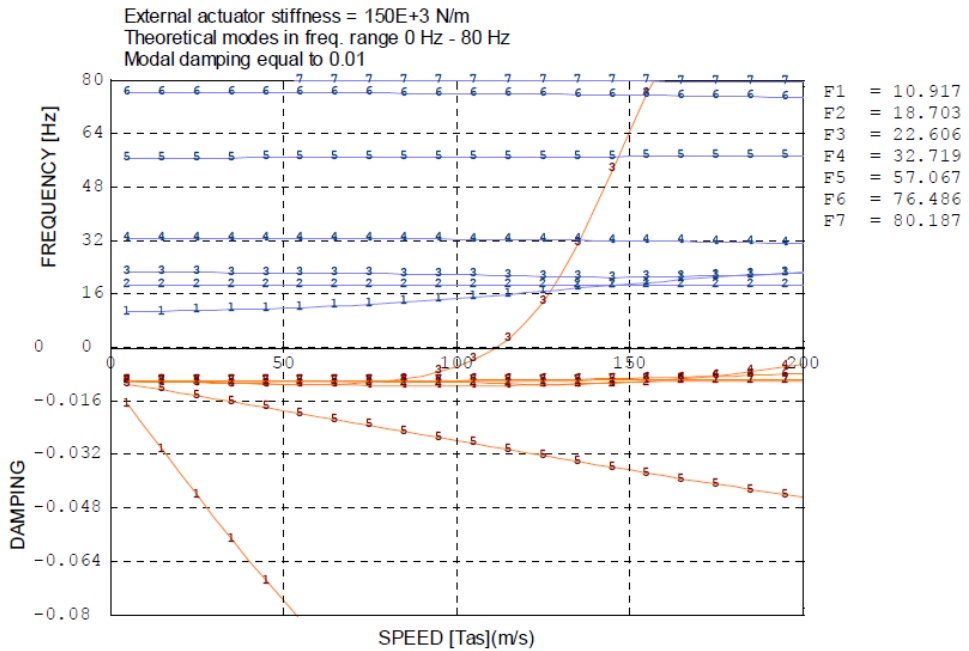


Figure 135 – Vg plot for case 3

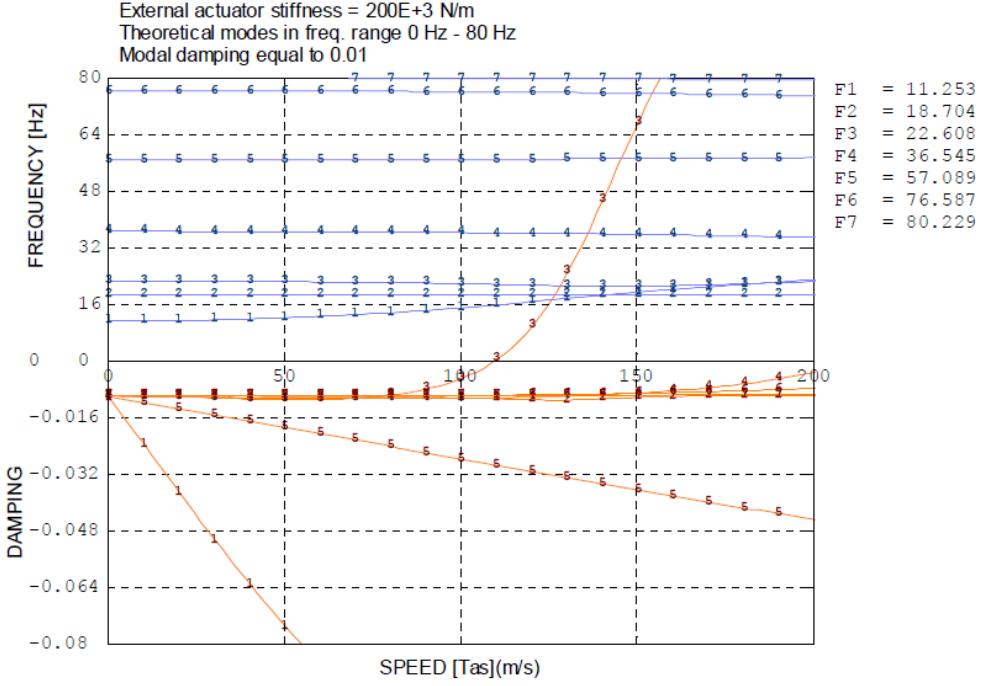


Figure 136 – Vg plot for case 4

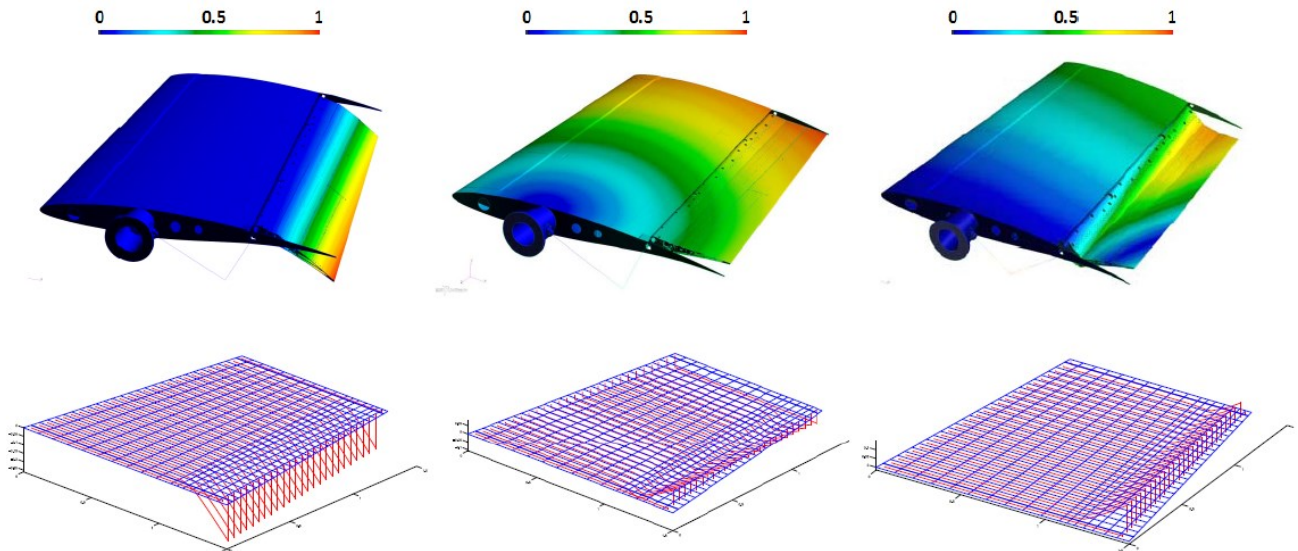


Figure 137 – Mode 1: Aileron harmonic (left); Mode 2: T/A bending (centre); Mode 3: Aileron tab mode (right)

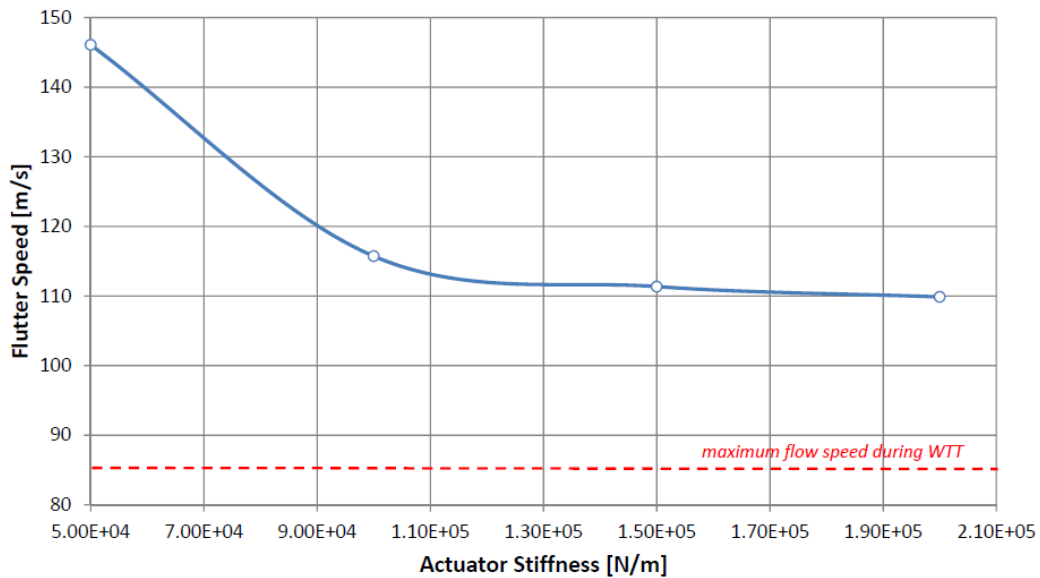


Figure 138 – Flutter Speed versus aileron actuator stiffness

In light of these results, it has been demonstrated that, from a theoretical point of view, the T/A is free from any dynamic aeroelastic instability up to 1.2 times the maximum expected airflow speed during tests; in addition, the robustness of the obtained results are proven with respect to change in control surface harmonic covering a wide range of value for the stiffness of the aileron external actuator.

The next step consist of a validation of the flutter analysis with experimental normal modes, which is schematically reported in Figure 139.

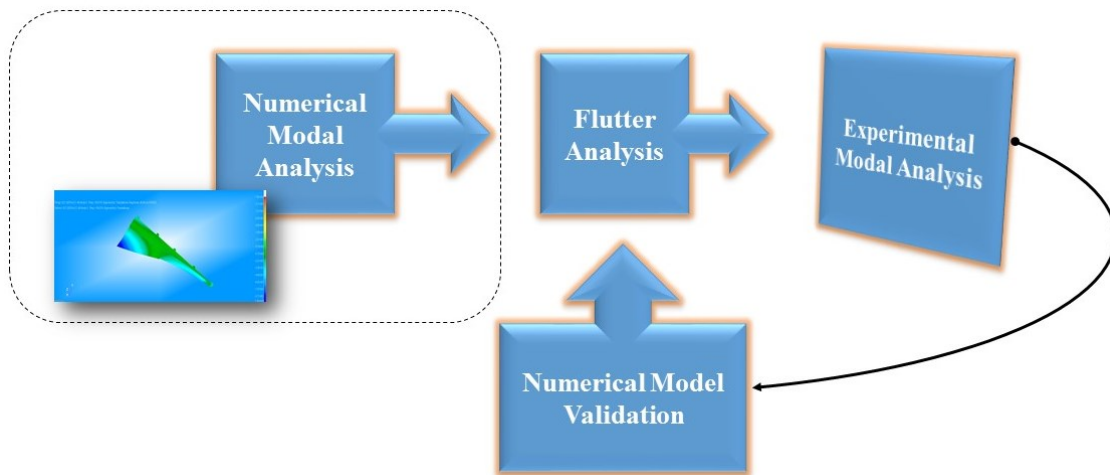


Figure 139 – Aeroelastic scheme for flutter validation

3.7 *Aileron Manufacturing*

The aileron manufacturing phases are herein presented and described with reference to the material in Table 10. Structural parts was manufactured by means an high precision (54 μ m axis error) CNC while linear guides and actuators are components off-the-shelf (COTS). In the subsequent pictures the segmented rib architecture is reported with focus on the connection hinges and link.

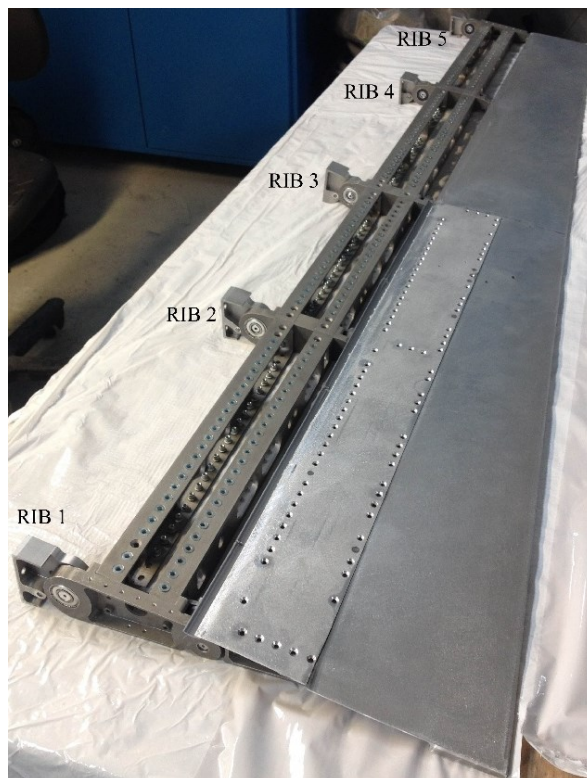


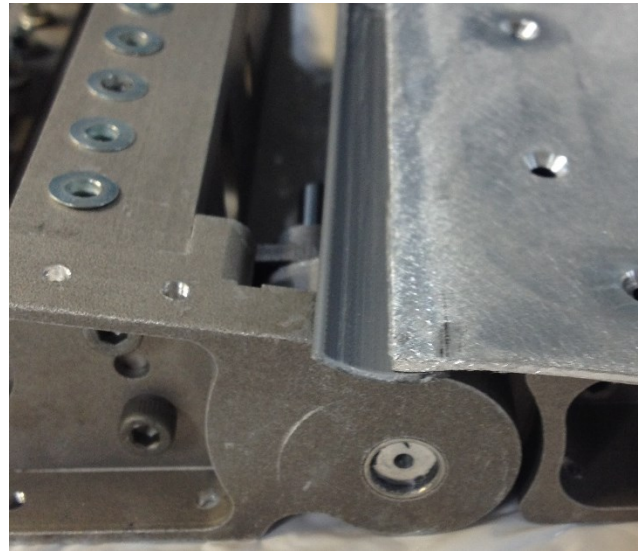
Figure 140 – Aileron assembly during manufacturing process



Figure 141 – Aileron segmented Rib with rotational hinges



(a)



(b)

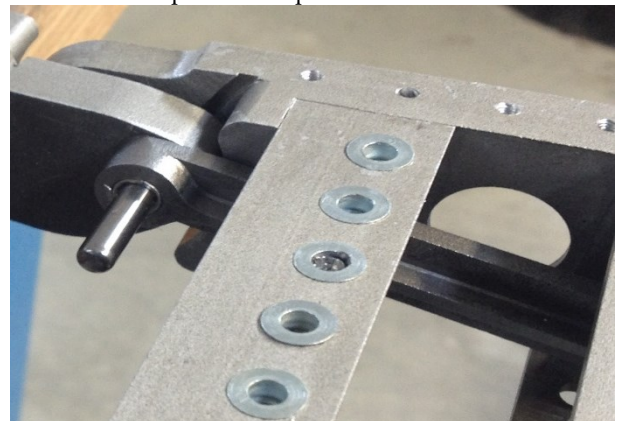
Figure 142 – Enlargement on the Hinge 1 (a) and Hinge 2 (b) with internal bushing



Figure 143 – Connection link between non-consecutive rib plate 1 and plate 3



(a)



(b)

Figure 144 – Focus on the link pin of the rib plate 1 (a) and rib plate 3 (b)

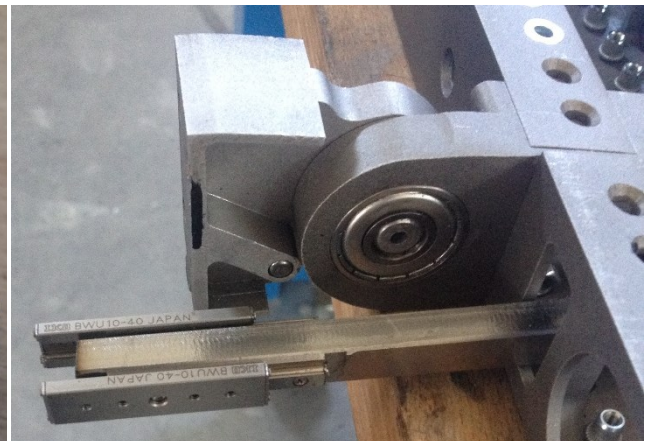
The main components of the actuation kinematic chain are schematically reported below (from Figure 145 to Figure 147) where it is also represented the integration inside the aileron skeleton.



Figure 145 – Actuation system components: Beam, plates and crank



(a)



(b)

Figure 146 – Linear guides (a) and double sided configuration partially integrated into the aileron (b)

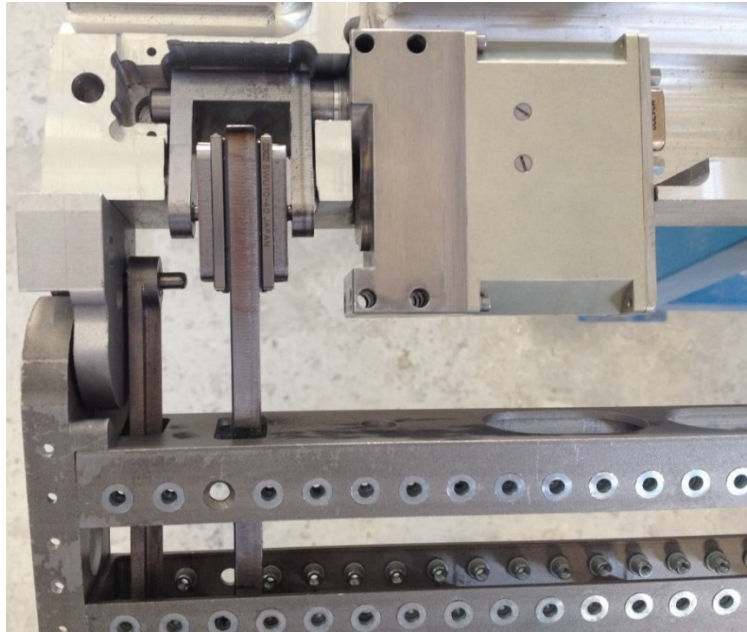


Figure 147 – Full integration of the actuation kinematics and the rotary actuator into the aileron

Finally the full system equipped with three actuators are showed in Figure 148. The actuator properties (BENTAL RSA-06) are summarized in Table 21. In particular, this actuator was developed according to UAV specifications in compliance with MIL-STD-461E,704D,810E. It is a high performance low-weight compact servo actuator used for flap control and other UAV applications based on pulse-width modulation (PWM). The 28Vdc RSA-06 includes a permanent magnet brushless servomotor, reduction gear, feedback sensor on output shaft, electronic servo control and amplifier, all packed inside a low-weight compact anodized aluminum case.

Specifications	Unit	Value
Nominal Operating Voltage	Vdc	28
Operating Voltage	Vdc	18 ÷ 32
No load Speed	sec ^o /	250
Intermittent Stall Torque	Nm	12.0
Continuos Torque	Nm	6.5
Nominal Continuou	A	0.5
Useful Angular Stroke	°(deg)	±45
Mechanical Limits	°(deg)	±49
Angular Backlash	°(deg)	Max 0.6
Bandwidth @ No-load		
4° Amplitude	Hz	15
6° Amplitude	Hz	10
10° Amplitude	Hz	6
Weight	g	415

Table 21 – Actuator characteristics



Figure 148 – Actuation kinematic contained into the aileron structure

The actuators cabling layout are now discussed. At NRC wind tunnel, the aileron control equipment are positioned below the test chamber; so that all the cables must go through the T/A, under the wind tunnel floor and directly to the controller. The aileron leading edge is properly designed in order to accomplish cabling requirements. In fact, it consist of two

different parts (upper and lower), both machined, with defined cables path from actuators serial ports to the external side of the aileron (Figure 149) passing through a 50 mm diameter hole positioned in the wing-box as shown in Figure 150.

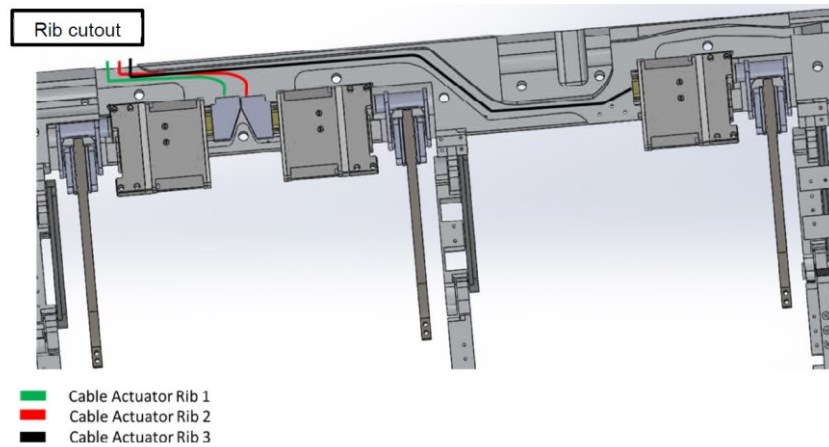


Figure 149 – Aileron cabling layout

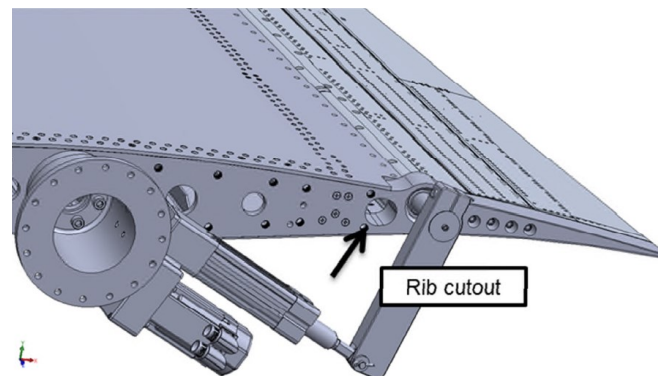


Figure 150 – Cabling hole

A schematic scheme of the entire cables path are shown in the next Figure 151.

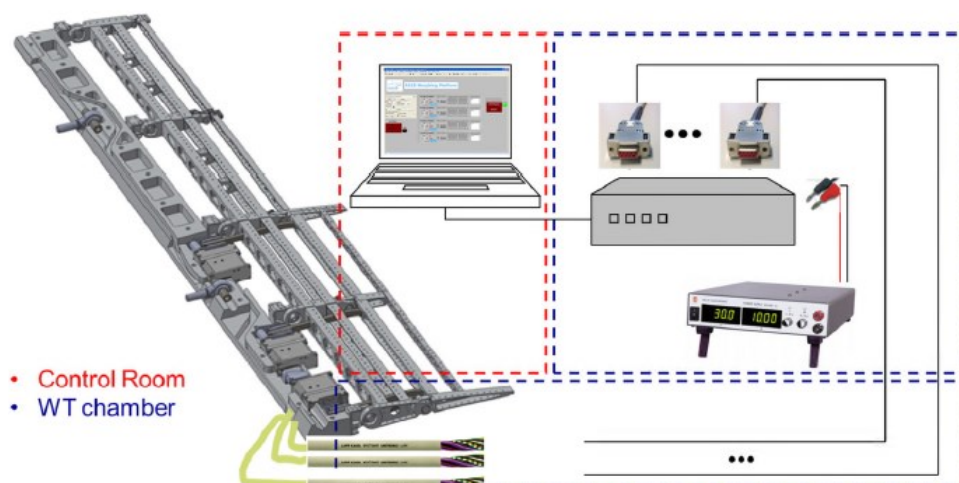


Figure 151 – Synthetic representation of the aileron set-up inside the wind tunnel

The next two images (Figure 152&Figure 153) represent firstly a detail of the actuator in power on condition and aileron in morphed down (moved linear guides) and finally the

cabling passing through the LE hole. It is evident that the LE is divided into an upper and lower part as previously mentioned.

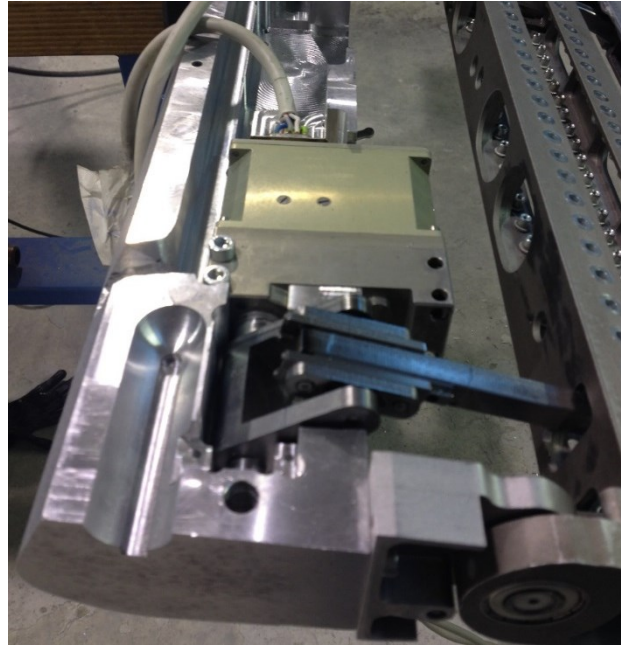


Figure 152 – Actuator cabling



Figure 153 – Aileron leading edge with cabling hole

The final manufactured prototype (after painting) are shown in Figure 154.



Figure 154 – Photo of the Actual Aileron Prototype.

4. Experimental tests and correlations

A dedicated experimental campaign was carried out with the aim of characterizing the demonstrator and estimating eventual deviations from the numerical expectation before the wind tunnel test campaign. A dedicated experimental campaign was assessed out to:

- Verify the control logic algorithm by means of actuators bench tests. In this tests, the actuators operative conditions were simulated such as fast and slow movement with a “step” or a “sine” function.
- demonstrate the morphing capability of the conceived structural layout;
- comparison between the numerical and experimental shapes;
- characterize the dynamic behavior of the morphing structure through the identification of the most significant normal modes;
- validate the numerical model.

The equipment used to drive the aileron (control system) during the validation testing is depicted in Figure 155 and below listed with other instrumentation used for experimental modal analysis.

- Power supply (1.5 ÷ 24 VDC @ 1.0 A): to supply prototype actuator;
- DSPACE DSP controller;
- Fiber optic cable and BNC cable;
- switch box;
- control panel;
- tri-axial accelerometers;
- excitation shaker.

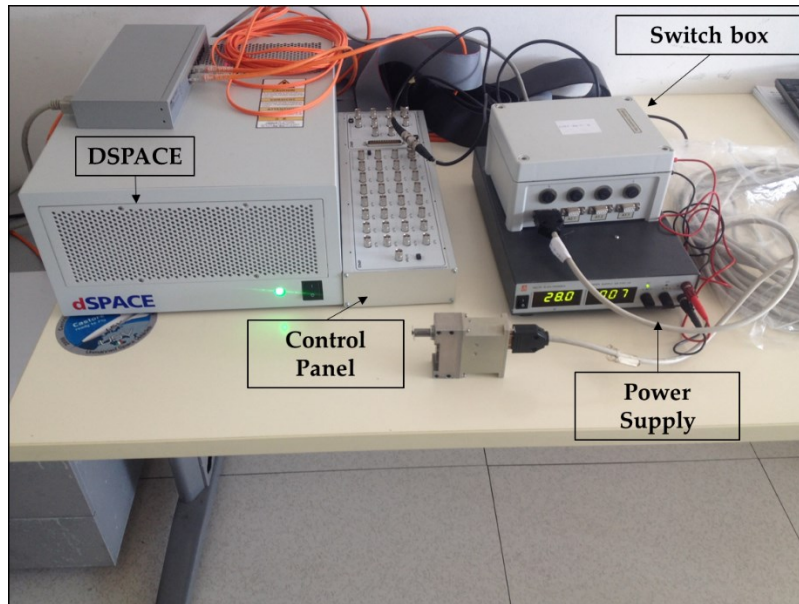


Figure 155 – Setup for aileron experimental campaign.

4.1 Control Logic implementation

4.1.1 Basic mathematical model of an electrical Servo-Actuator

The dynamic model of the electrical servo-actuator consists of two sub-models: DC motor and PD controller [48]. A comprehensive approach for building a mathematical dynamic model of an electric motor is a second-order dynamic system:

$$J\ddot{\theta} = I_{motor}K_t - M_{ext} - F_i\dot{\theta} \quad (14)$$

where the state variable θ is an angular position, J is a moment of inertia of motor moving frame, I_{motor} is an armature current, K_t is a motor constant, F_i is a friction coefficient and M_{ext} is an external moment acting on the motor axis. The block diagram of an electric motor is represented in Figure 156. Additional parameters, which are not represented in the dynamical equation but essential for the whole system modelling, are K_b generator constant and the Gear-Ratio.

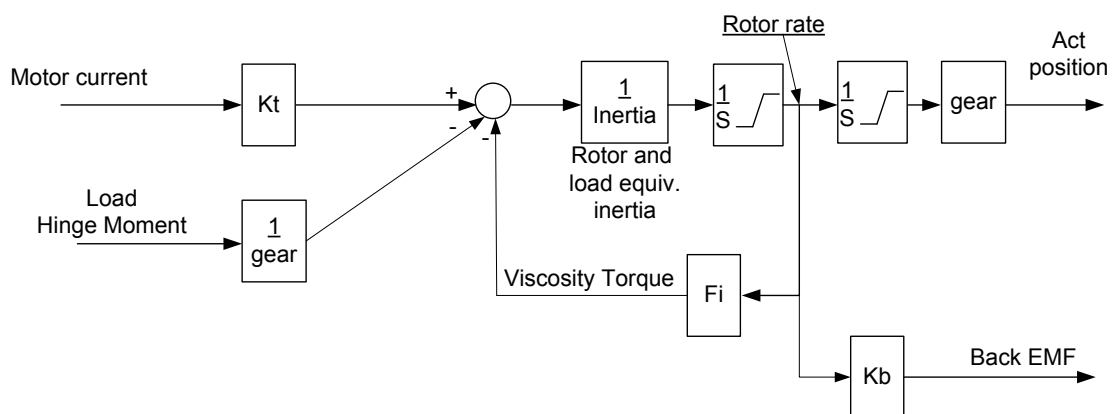


Figure 156 - Block Diagram of an Electric Motor ([48])

A simple mathematical model of a built-in controller is shown in Figure 157. This model is a basic PD feedback controller with command input of desired angular position θ_{cmd} and output of the direct current for the electric motor I_{motor} . The absolute maximal current is limited by supplied voltage subtracted with back EMF divided by coils resistance R .

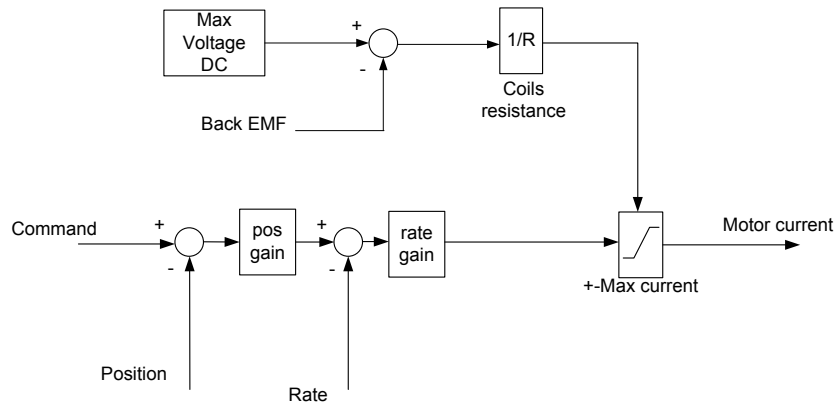


Figure 157 - Block Diagram of Built-in Controller ([48])

4.1.2 Selected actuator modelling

Using manufacturer provided data (Table 21) concerning the Bental® RSA-06 DC servo-actuator, some model coefficients were calculated directly from the specifications, while others were tuned in order to meet manufacturer's declared performance. The only parameters needed to be calculated are K_t , J and F_t . The motor constant K_t is calculated by continuing the maximal Torque-to-Rate line, shown in Figure 158, to get the maximal unsaturated static torque (14.8 Nm), by given rated current of 0.5 A. The immediately derived K_t is then $0.136 \frac{Nm}{A}$.

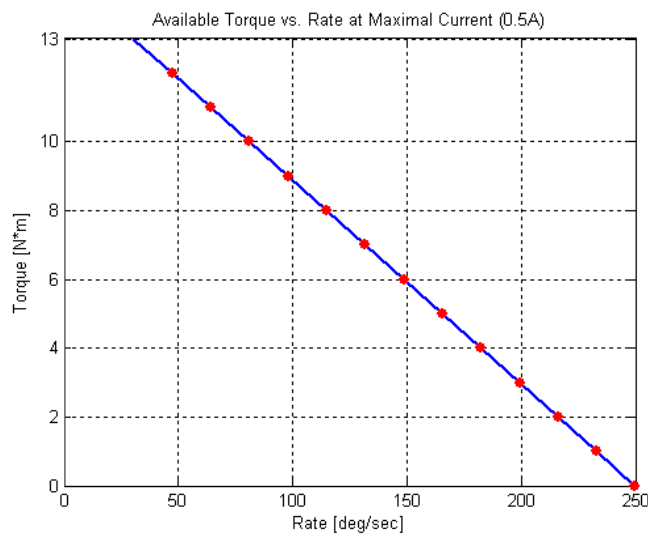


Figure 158 - Bental RSA-6, Maximal Torque vs. Maximal Rotation Speed

The motor moment of inertia J and friction coefficient F_i must be fitted in such a manner that (assuming unlimited integrals both in position and rate) the maximal declared steady-state rate will fit for the each maximal declared torque. As a result J and F_i became $0.137 \cdot 10^{-4} \text{ Kg} \cdot \text{m}^2$ and $7.14 \cdot 10^{-5} \frac{\text{Nm} \cdot \text{sec}}{\text{rad}}$ respectively. Other parameters fitted in such a manner are coils resistance R and back EMF coefficient K_b . Giving maximal operating voltage of 32V and maximal current of 0.5A, by using maximal static load and maximal angular rate, the derived R is 64Ω and K_b is $0.128 \frac{\text{V} \cdot \text{sec}}{\text{rad}}$.

In order to meet the declared bandwidth of 6 Hz and assuming damping of 0.6, the controller's gains became: $K_{pos} = 31.5$ and $K_{rate} = 0.02$. Figure 159 shows the frequency response of the full servo-actuator model.

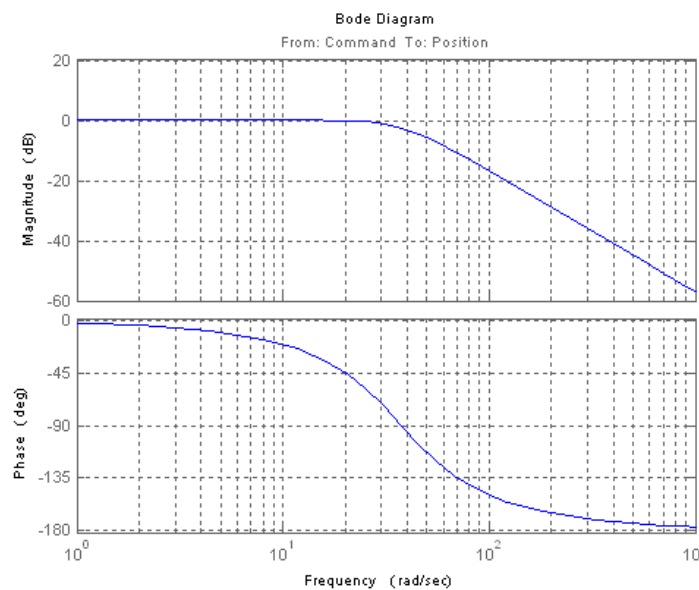


Figure 159 - Frequency Response of the Servo-Actuator

4.1.3 Morphing Aileron Controller strategy

The objective of the morphing control platform is to control the wing shapes by introducing actuation forces so as to match as accurately as possible each of the desired wing shapes exhibiting optimal aerodynamic performance. At each iteration, the actual shapes are compared with the optimal ones so as to minimize the error function in approximating them. The process concludes when such a difference is lower than a threshold value. Figure 160 illustrates the controller design work-flow suitable for a morphing wing controller design application [49]. It comes up from an adaptation of the well-known "V diagram", widely employed for the development of model-based control systems using the techniques of rapid prototyping and hardware-in-the-loop testing. The most important aspects of the process are:

- Design of the control system: Use of MATLAB/Simulink to design and select the system coefficients of the controller;

- development of a Simulink model: Use of Simulink blocks to graphically model the physical system;
- run simulations in non-real time: check the behavior of the model before creating a real-time application. Check the stability of the model;
- hardware in the loop simulations: the controller design is tested with hardware in the loop. This step provides a validation feedback of communication protocol and parameter tuning in an actual dynamic environment
- create a real-time application: real-time workshop code generation (C code) from simulink model. The C/C++ compiler compiles C code to an executable code downloaded to the controller DSP board running in real-time;
- run the application in real time;
- analyse and visualize data;

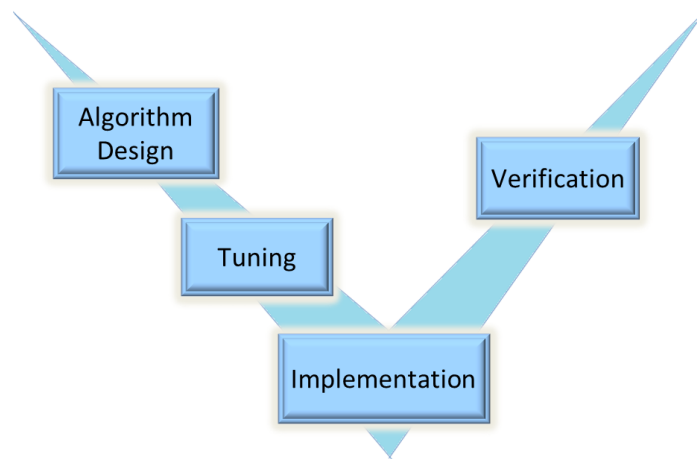


Figure 160 - Controller Design Work-flow diagram ([49])

As the control performance depends on the accuracy of the identified model, a mathematical model capturing adequately the system dynamical motion is needed for a successful controller design. This model can be also experimentally captured on dummy structures. Before controlling the system in mathematical terms, it is fundamental to understand how the system behaves without control. To this aim, numerical simulations and experimental data of the morphing system and the rotary actuator are necessary. This provides the opportunity to prove out processes prior to field implementation enhancing the degree of confidence of the assumptions made in the controller design. The controller executed the driving command on the basis of the off-line predictions of the actuator shaft rotations needed to reach specific aileron morphing angles. As a result, the controller gives no feedback on the achieved trailing edge shape (open loop). Such a logic was implemented in a morphing platform running in a dSPACE system, shown in Figure 161 during actuators bench test. The dSPACE system is high performance digital control system directly interfaced with MATLAB/SIMULINK running on a PC. The control logics are developed in SIMULINK block diagram, then converted to real time C running in real time in the DSP.

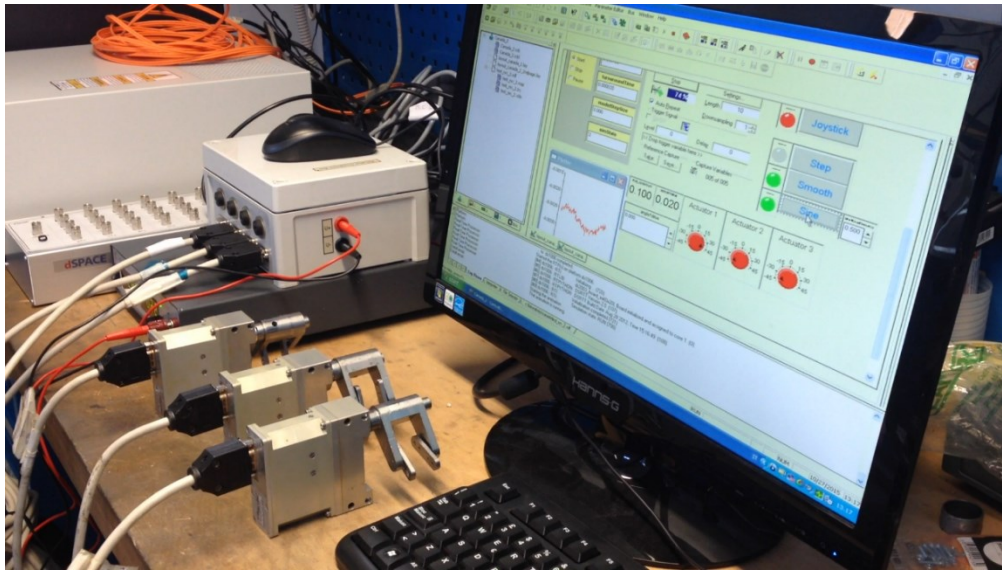


Figure 161 – dSPACE graphic interface unit during actuators bench test

In Figure 162 and Figure 163 are shown some encoder positions given by the actuators embedded in the WT model demonstrator for a step command rate of 4 [deg/sec] and a sinusoidal actuation of 0.5 Hz, respectively. Such experimental results matched perfectly the numerical expectations.

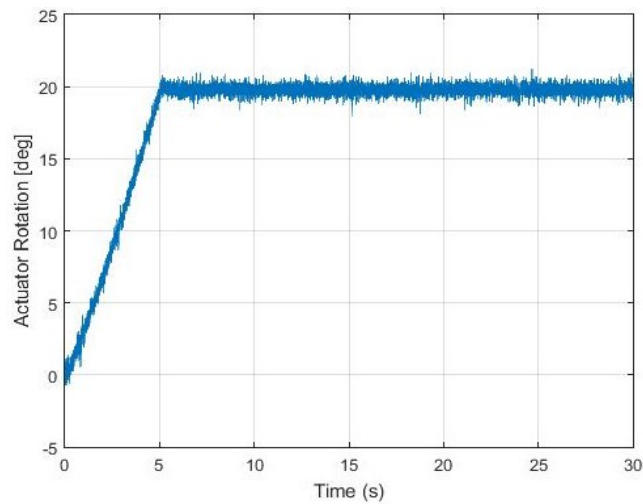


Figure 162 - Actuator encoder signal: step function

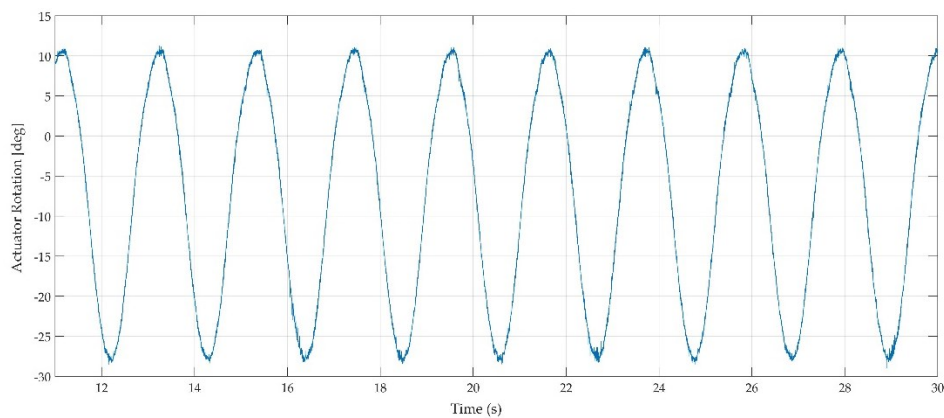


Figure 163 - Actuator encoder signal: sine function

4.2 GVT and numerical Correlations

The aileron GVT was conducted with the objective to confirm the numerical FE model of the aileron and with the purpose to confirm the aeroelastic stability analysis with the real normal modes. In the free-free condition, two most significant normal modes were detected in the range of interest from 0Hz – 100Hz:

- torsional mode, which is an antisymmetric elastic deformation;
- morphing mode, which is the aileron kinematic fundamental.



Figure 164 – Aileron GVT experimental setup

Finally, in the next Figure 165, it is represented the measurement points on the aileron upper skin where in red is indicated the monitoring points while in blue the driving point.

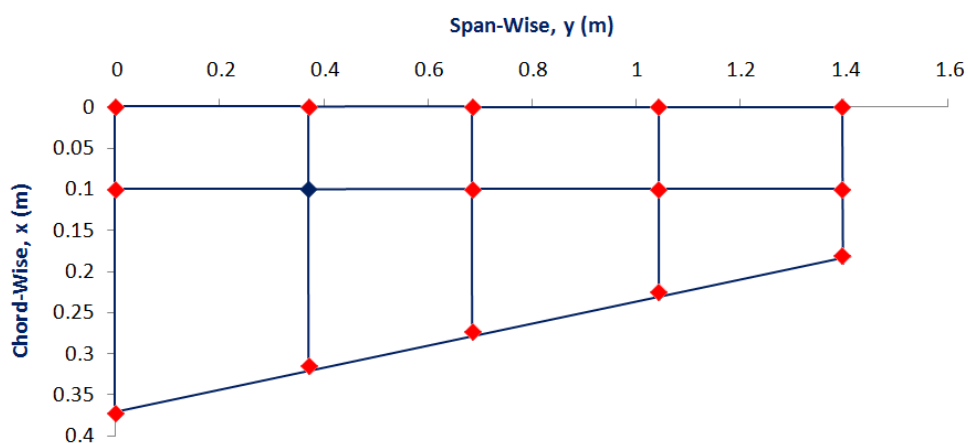
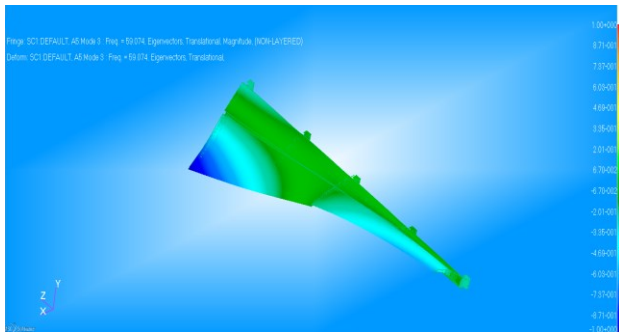
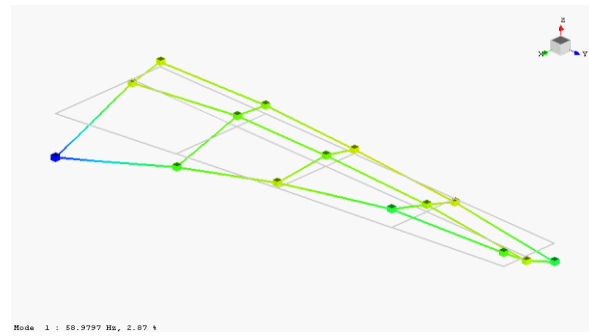


Figure 165 - Aileron Measurement Points

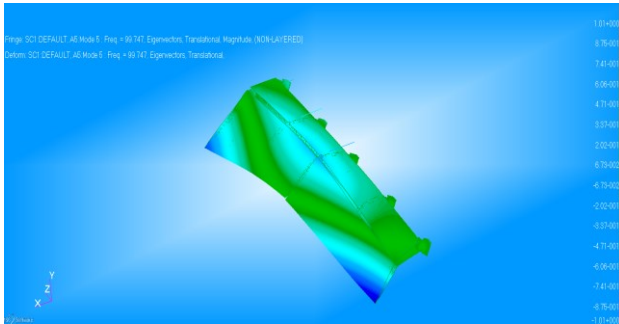
In the next Figure 166 the numerical and experimental modal shapes are reported while the graph Figure 166 shows a satisfactory correlation.



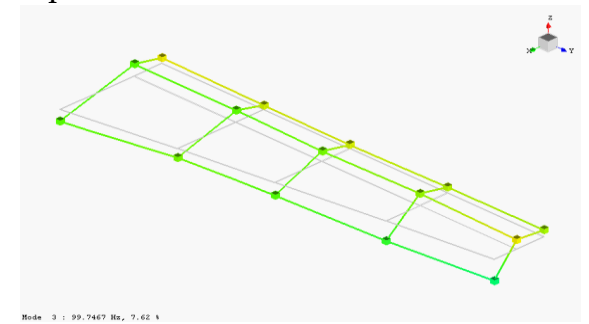
Torsional mode at 59.07 Hz



Experimental torsional mode at 59.98 Hz



Morphing mode at 97.75 Hz



Morphing mode at 99.75 Hz

Figure 166 – Numerical and experimental normal modes comparison

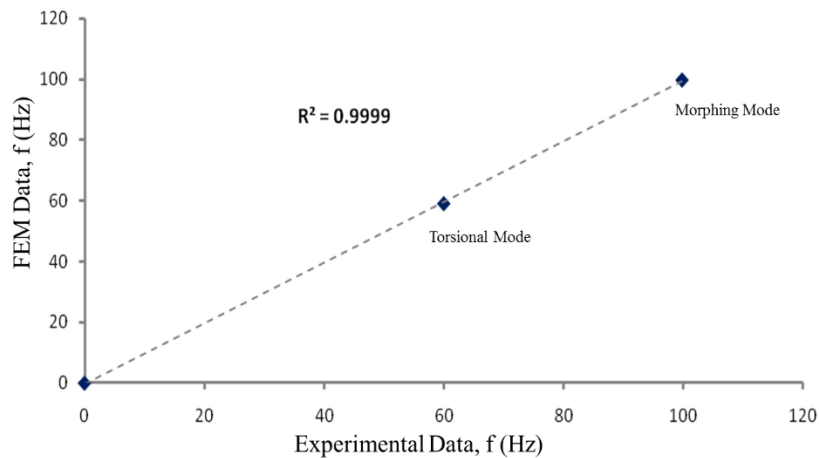


Figure 167 – Normal modes correlation

4.3 Functionality Tests

A full scale laboratory demonstrator was finally manufactured and tested to:

- demonstrate the morphing capability of the conceived structural layout;
- characterize the dynamic behavior of the morphing structure through the identification of the most significant normal modes.

Rational approaches were implemented in an efficient test campaign providing the necessary database for the mechanical demonstration of the morphing structure. Test outcomes showed that:

- reliable and stable morphing compliant with design requirements is assured by the device;

- normal modes result unaffected by architecture's settings (morphed/unmorphed) and related parameters (frequency/damping/shape) do not give rise to specific concerns of aeroelastic nature.

The functionality test consist of characterize the aileron kinematic in terms of actuator rotation and rib deflection. This is analytically expressed by equation 2. For each morphing angle, within the range from -4° to $+6^\circ$, a given actuator shaft rotation was imposed and the tip displacement was measured as reported in Figure 168. The experimental points have been reported in the diagrams in Figure 169 with the comparison, showing then a good agreement.

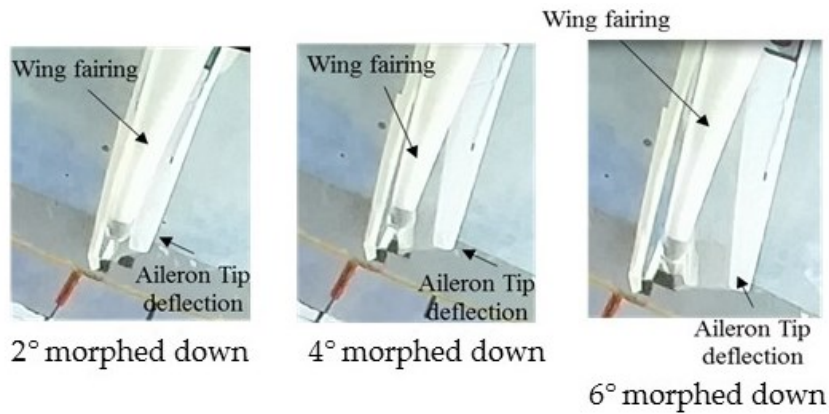


Figure 168 - Morphing Aileron at various deflections

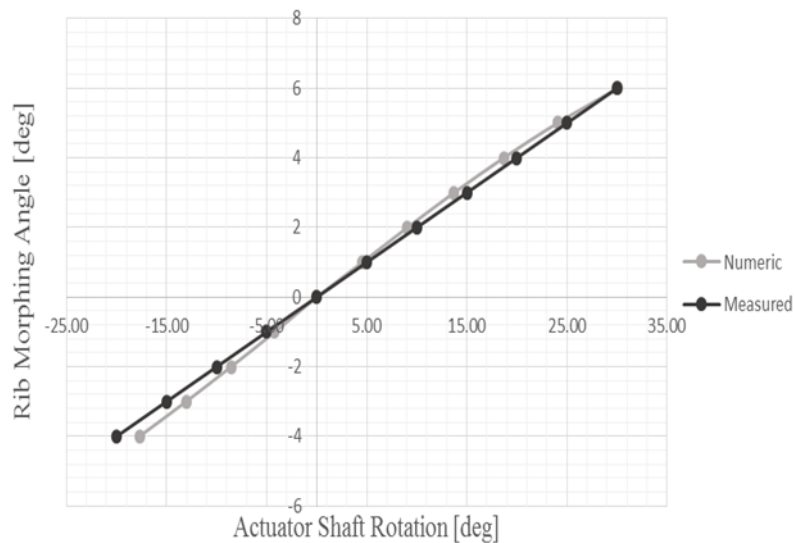


Figure 169 - Correlation between numerical and experimental: actuator rotation versus morphing deflection

4.4 Experimental shape

In this section, a comparison between the numerical and experimental aileron shapes will be carried out. In Figure 170, the CAD model expectations are depicted. The aileron is represented in both morphed down (+5°) and morphed up (-2°) configurations.

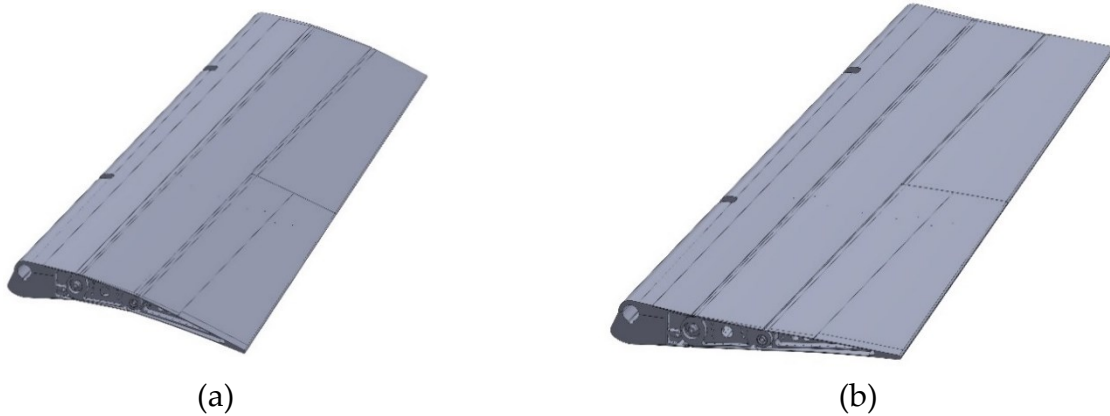


Figure 170 - Dimetric view of the aileron morphed shapes respectively +5° and -2°

The upper aileron surface was generated by a smooth reconstruction based on biharmonic spline interpolation. The actual attained aileron shapes were measured. The aileron scan was performed by NRC (National Research Council – Ottawa) using high precision photogrammetry procedure utilizing 3D-tracking cameras with circular retro-reflective markers applied on the upper skin. In the graph reported in Figure 173, the correlation are shown. Green marker represent the experimental measurements while the aileron skin is reported as a uniform surface. It can be noticed that there is a good level of matching except in some points for the morphed up configuration where small deviation is observed.

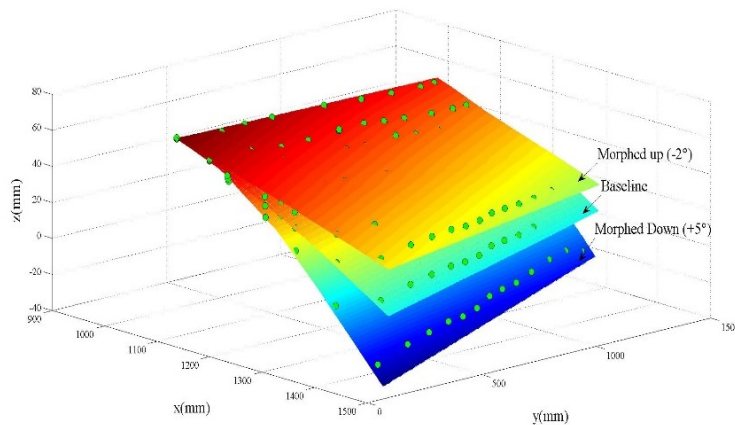


Figure 171 – Comparison between numerical and experimental aileron shapes

5. Wind Tunnel Tests

5.1 Aileron assembly

This chapter is aimed at providing a step-by-step procedure for the installation of the morphing aileron on the wing box. The procedure is characterized by four steps:

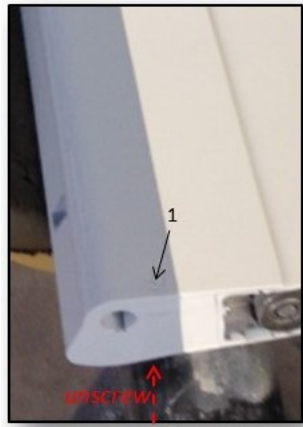
- I. Remove the upper side segment of the morphing aileron leading edge;
- II. Insert the inner hinges into the wing box;
- III. Insert root and tip shafts;
- IV. Reinstall the upper side segment of the morphing aileron leading edge.

Regarding the first step, the leading edge is characterized by 2 blocks (upper and lower) joined by 10 screws. In order to remove the upper segment you need to remove all the screws which all have a specific length matching its own hole only; in order to efficiently reinstall the upper block of the leading edge the screws have been marked after the removal according to the nomenclature given in the Figure 172.

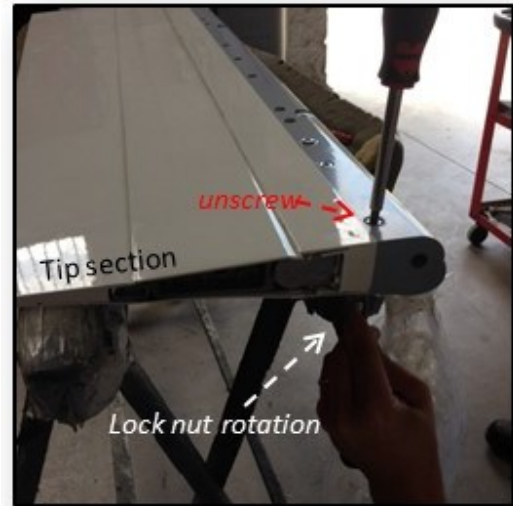


Figure 172 – Photo of the morphing aileron with leading edge holes numbering

The first screw is nut-less; the head is on the lower side. You can unscrew it by working as shown in the Figure 173 (a) on the left. Moreover, all the other screws have a nut; the head of each screw is on the upper side of the leading edge, the nut on the lower side. In order to remove each screw, it is necessary to prevent the rotation of the nut and to unscrew from the upper side as shown in the Figure 173 (b) below.



(a)



(b)

Figure 173 – Procedure of removing the leading edge first screw

After the removal of the upper segment of the leading edge, the inner part of the device will be fully accessible. Removing inner hinges (tie-rod end) from their housing and lock them to the rear spar of the wing box. After this, put the hinges shafts again in their housing on the morphing aileron.

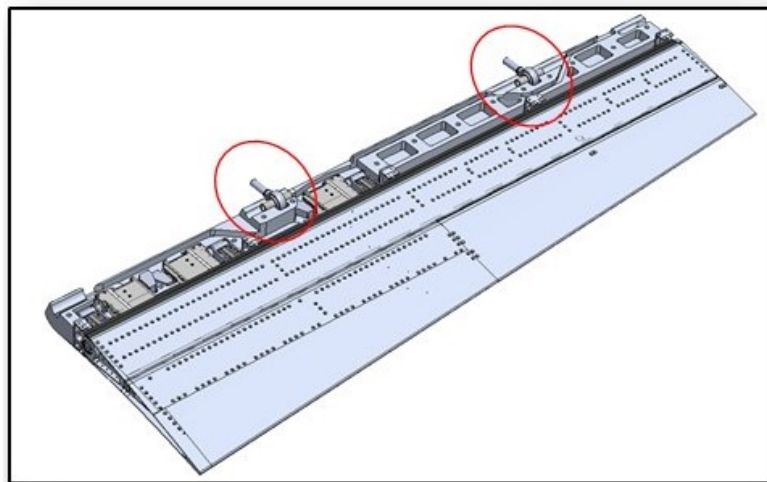


Figure 174 – Aileron tie rod

The subsequent step (3) consist of insert root and tip shafts (red circles in the Figure 175 below) into the holes at root and tip wing sections; finally place them into their housing on the morphing aileron.

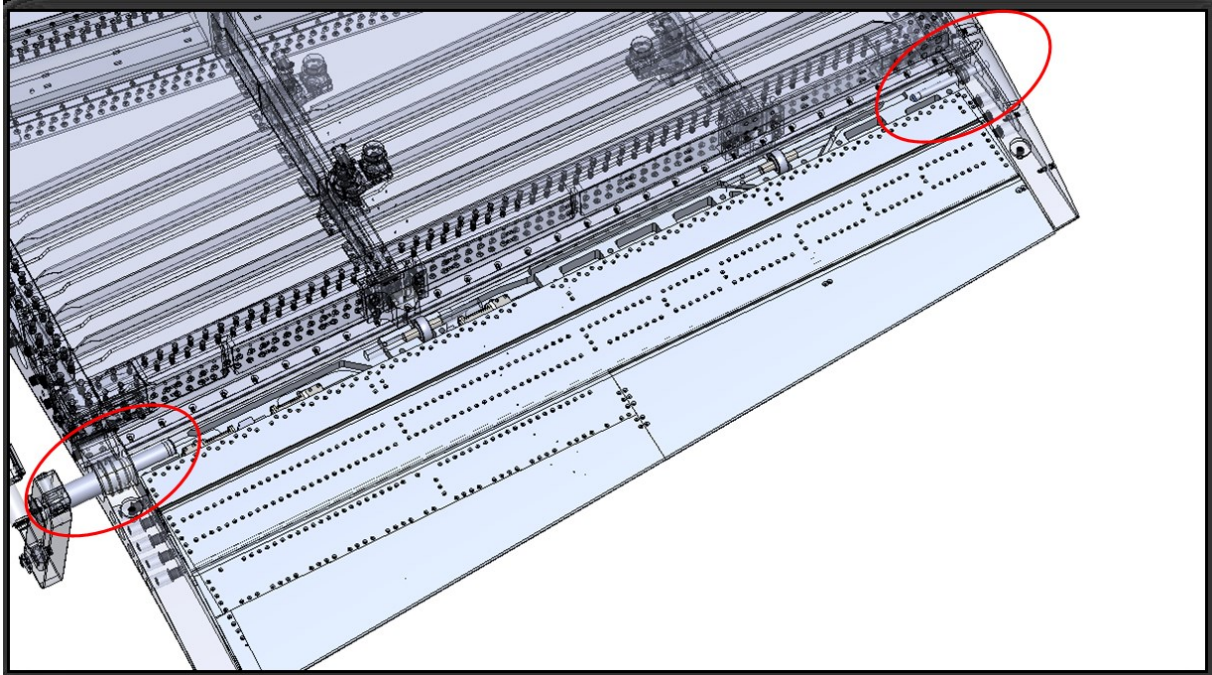


Figure 175 – Aileron shaft housing

At this point, reinstall the upper side segment of the morphing aileron leading edge as already done in the step 1 but in a reverse sense. The morphing aileron is equipped with 16 pipes/taps as reported in Figure 176. Pressure taps on the morphing aileron are a subset of those defined for the rigid aileron and they have the same chord-wise and spanwise positions of those on the rigid aileron which has been provided by the Canadian team.

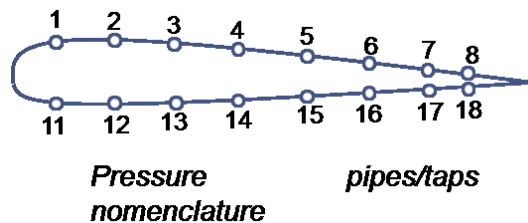


Figure 176 – Nomenclature of the pressure taps

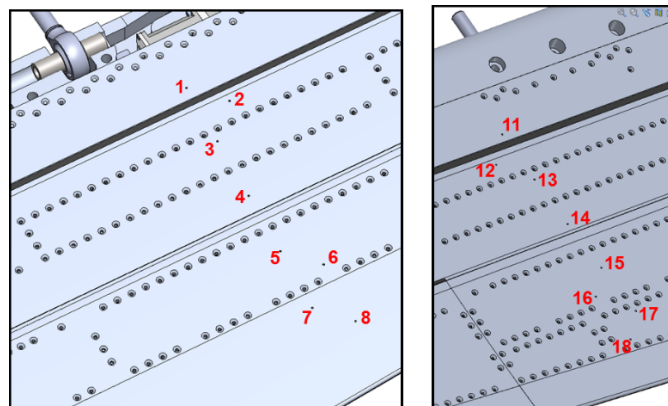


Figure 177 – Pressure taps position on the upper and lower side of the aileron

5.2 Aerodynamic curves and drag polars

In this section, it will be described the main results obtained from the wind tunnel tests campaign conducted on the T/A at wind tunnel facility of the NRC (National Research Council) of Ottawa (Canada). Firstly, the installation of the morphing wing prototype in the wind tunnel will be described and finally the main results outlined. The complete T/A is made of a two independent morphing concept:

- A morphing wing: the Canadian Team (ETS) is responsible of the control of the morphing skin. The wing upper skin thickness is modified by means of internal actuators that locally push upward the composite skin in order to generate a millimetre bump for flow control (delay transition from laminar to turbulent).
- A morphing aileron: the wing trailing edge is equipped with aileron. It is driven by an external actuation mechanism that allow its rotation around the main hinge line as a conventional architecture but furthermore a self-contained actuation system drive the camber morphing of the aileron. These two controls are independent and in particular, according to the test matrix, the aileron rigid rotation is set to zero during the tests. Only morphing is performed.

The assembly phases of the T/A inside the test chamber are below reported. In the following Figure 178 is depicted two photos of the CRIAQ morphing wing during the installation phase of the morphing aileron.

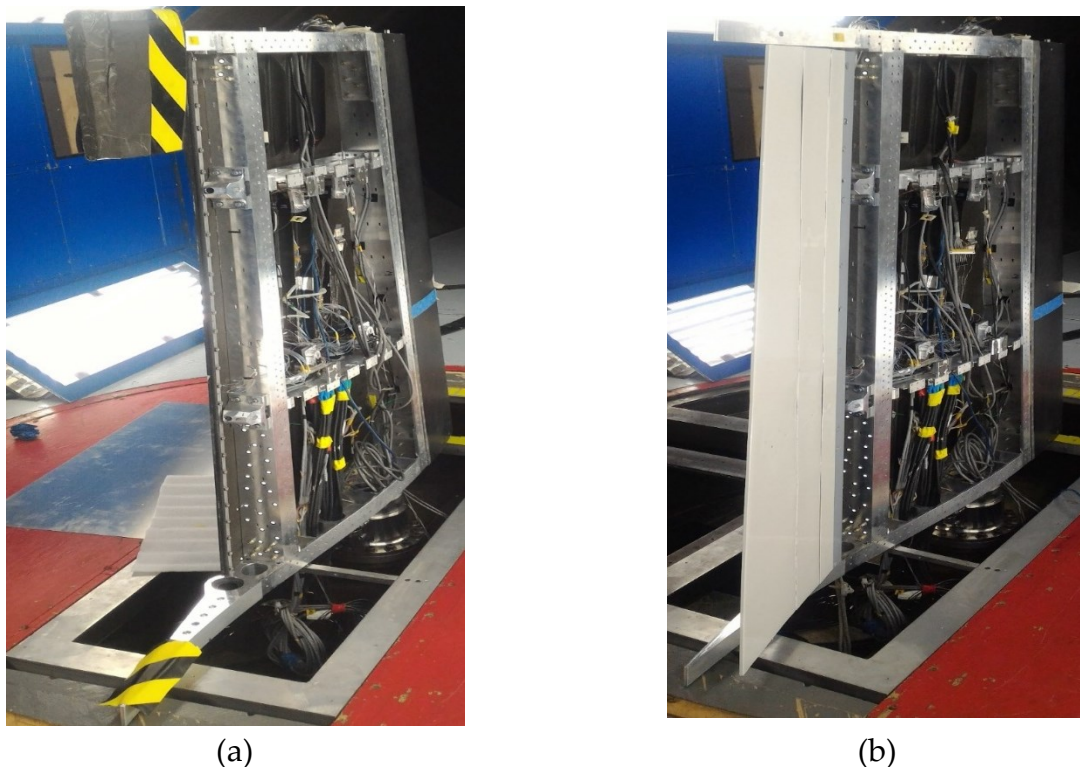
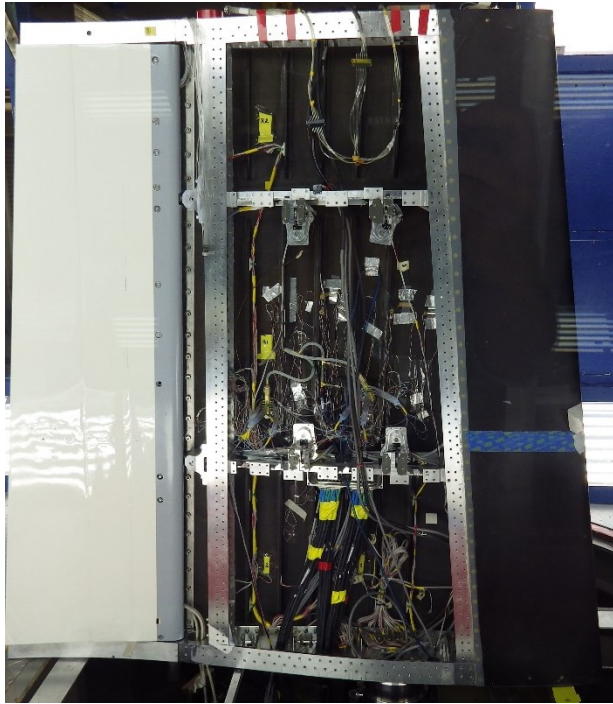
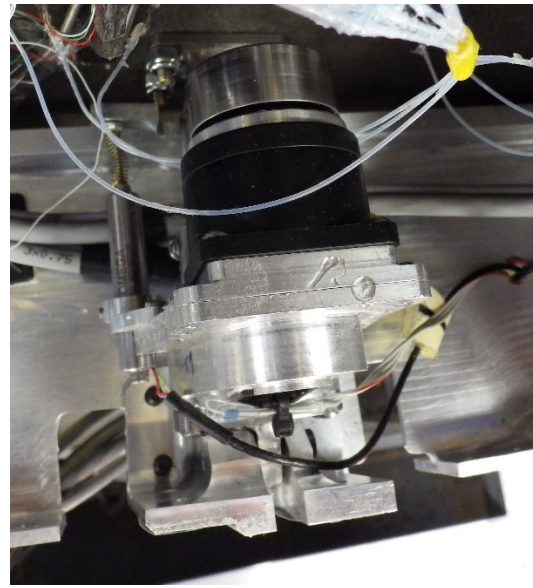


Figure 178 – Wing box prototype in the wind tunnel (a) and during aileron installation (b)

In Figure 179 is noticeable in withe, the morphing aileron and also the inner part of the wing (a) with a detail on one of the four actuators that drive the skin bump (b) [40]-[41].



(a)



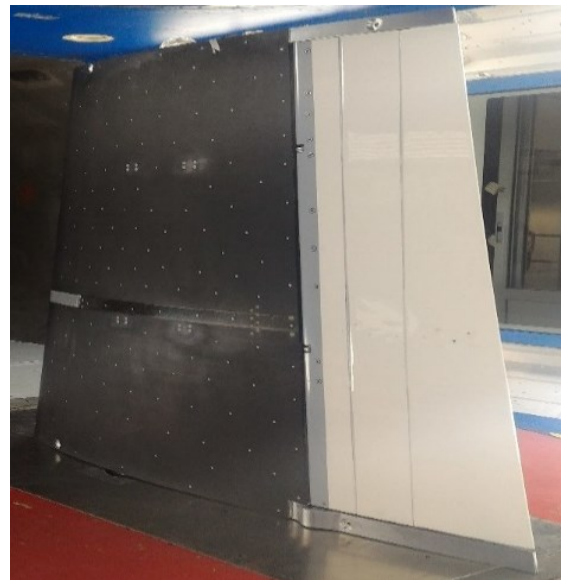
(b)

Figure 179 - Inner part of the wing (a) with detail on the actuator (b)

In Figure 180, other photos of the T/A are presented such as the subsequent Figure 181 to Figure 183.



(a)



(b)

Figure 180 – Morphing wing equipped with morphing aileron in a downward view (a) and upper view (b)

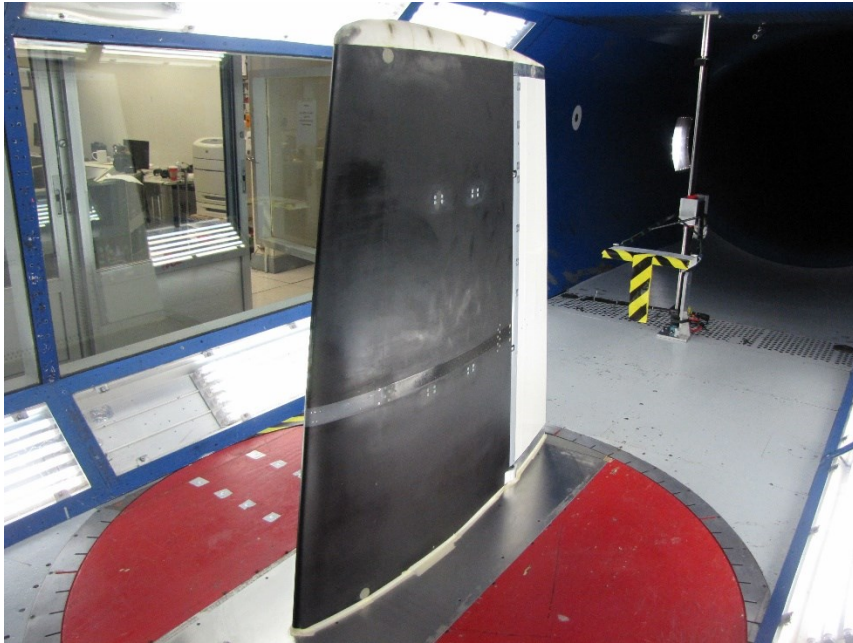


Figure 181 – Front view of the Morphing wing with wake-rake on the background

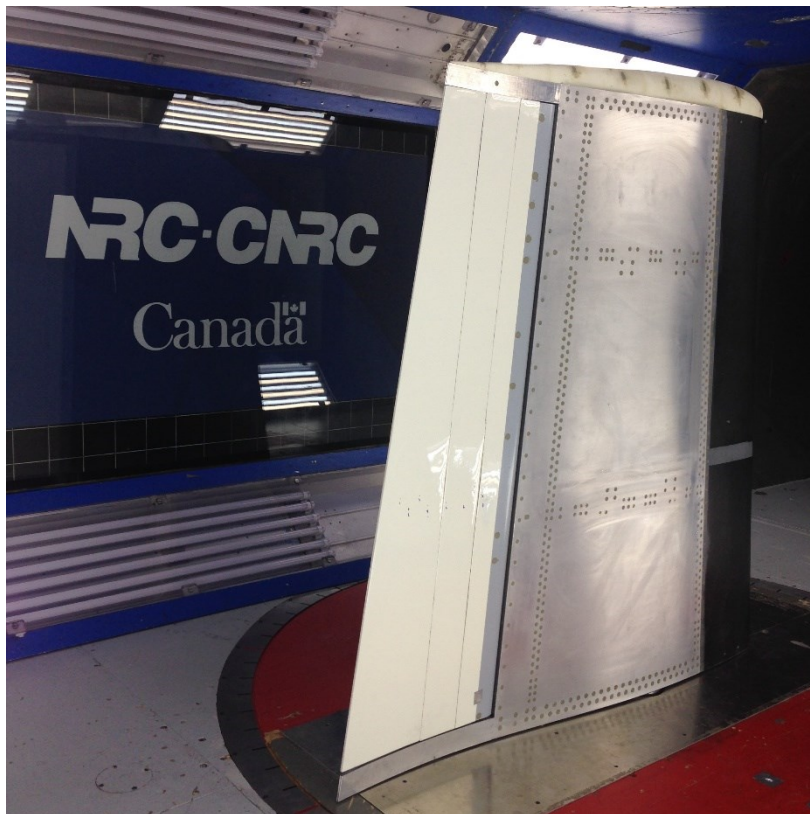


Figure 182 – Complete morphing wing in the wind tunnel at NRC (Ottawa)

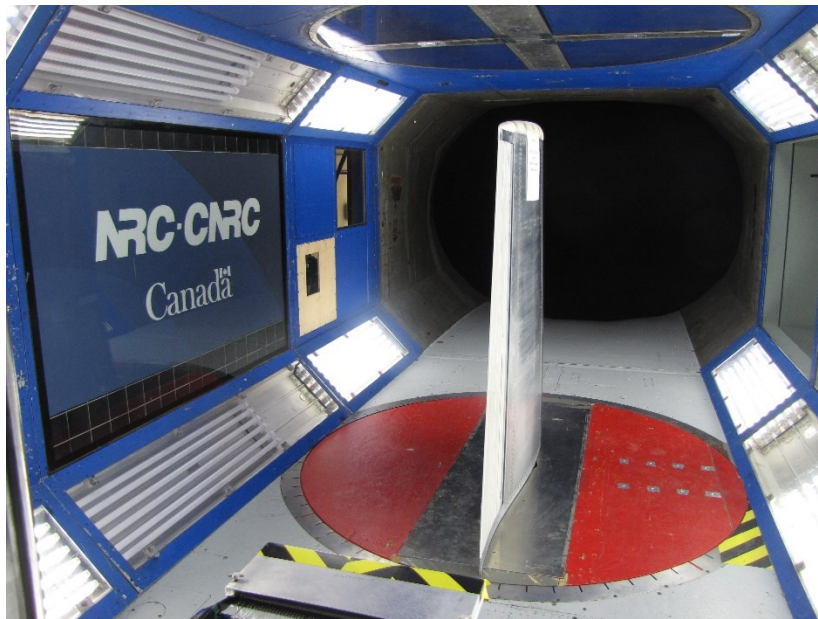


Figure 183 – Rear view of the morphing wing.

The next Figure 184 shows the aileron movement with detail on the root rib tip both in morphed down and morphed up.

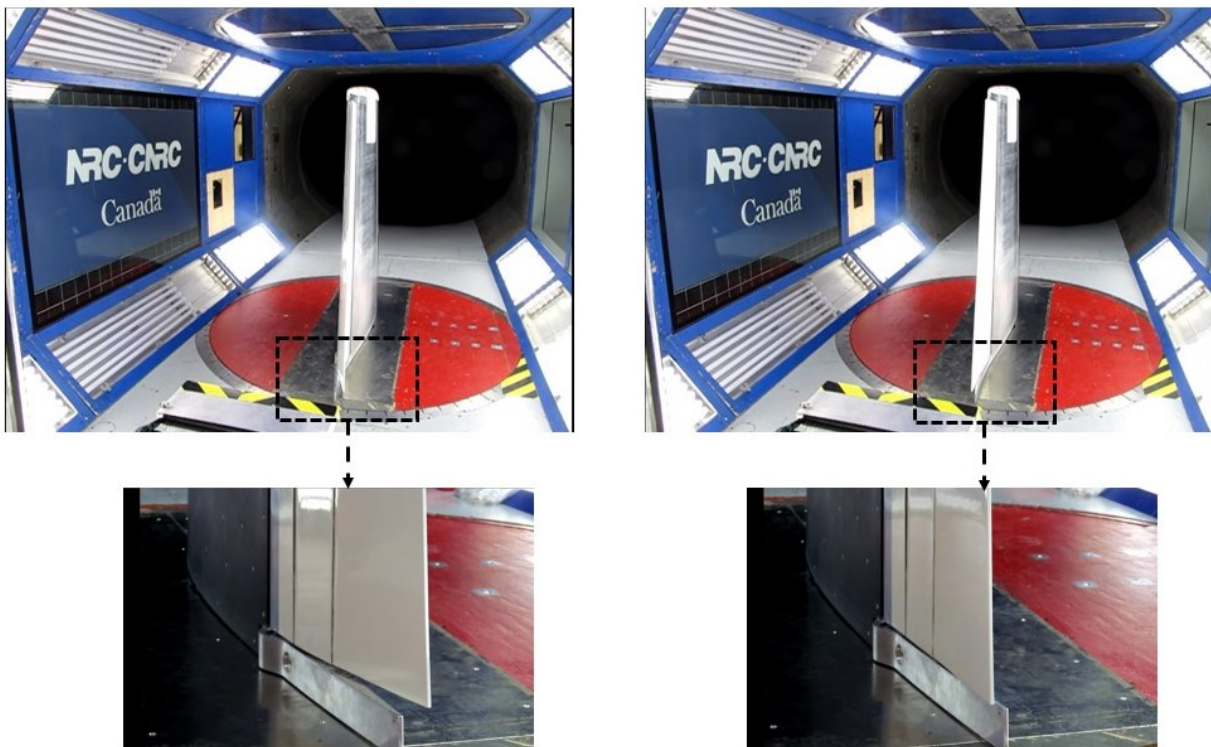


Figure 184 – Morphing aileron with detail on morphed up and down deflection

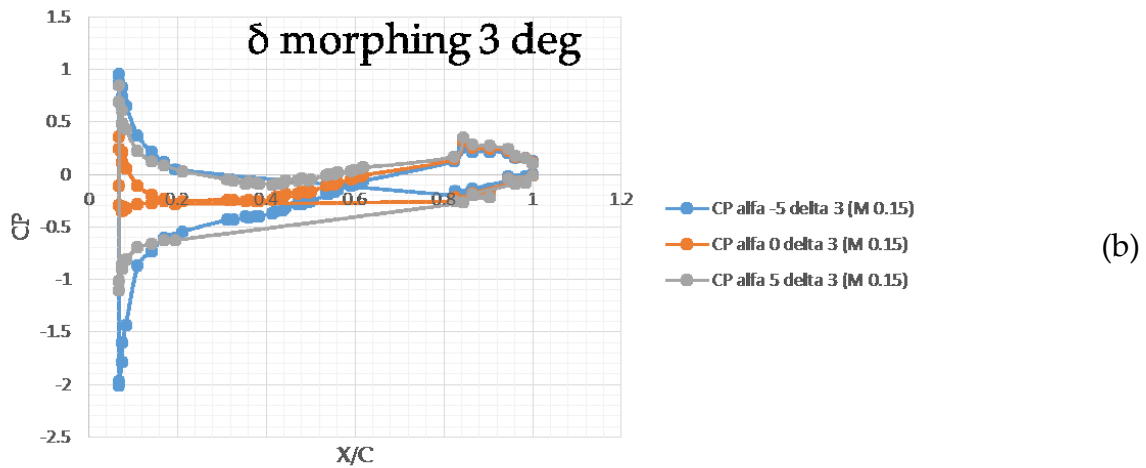
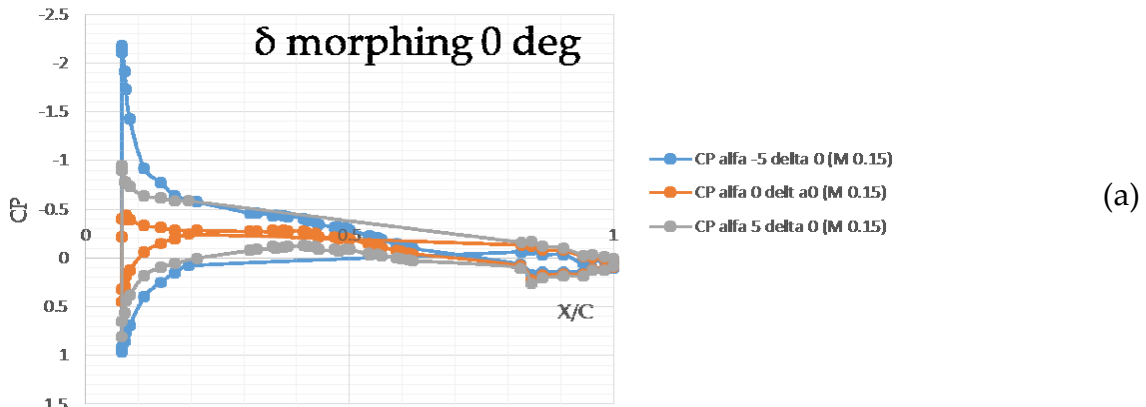
The wind tunnel campaign was conducted accordingly to the test matrix reported in the Table 22, mainly at two air speed respectively for Mach number equal to 0.15 and 0.20 where pressure distributions and balance forces were measured.

Case No	Mach	Expected AOA	δ morphing aileron
1	0.15	-3	-2
2	0.15	-2.5	-2
3	0.15	-2	-2
4	0.15	-1.5	-2
5	0.15	-1	-2
6	0.15	-0.5	-2
7	0.15	0	-2
8	0.15	0.5	-2
9	0.15	1	-2
10	0.15	1.5	-2
11	0.15	-0.5	0
12	0.15	-0.25	0
13	0.15	0	0
14	0.15	0.25	0
15	0.15	0.5	0
16	0.15	0.75	0
17	0.15	1	0
18	0.15	1.25	0
19	0.15	1.5	0
20	0.15	2	0
21	0.15	2.5	0
22	0.15	3	0
23	0.2	0	4
24	0.2	0.5	4
25	0.2	1	4
26	0.2	1.5	4
27	0.2	2	4
28	0.2	2.5	4
29	0.2	-1.4	3
30	0.2	-0.9	3
31	0.2	-0.5	3
32	0.2	0.6	2.5
33	0.2	1	2.5
34	0.2	1.6	2.5
35	0.15	-2.5	2

36	0.2	0	4
37	0.2	0.5	4
38	0.2	1	4
39	0.2	1.5	4
40	0.2	2	4
41	0.15	0	6
42	0.15	0	5
43	0.15	0	4
44	0.15	0	3
45	0.15	0	2
46	0.15	0	1
47	0.15	0	0
48	0.15	0	-1
49	0.15	0	-2

Table 22 – Wind tunnel test matrix

The pressure distributions on the morphing wing plus aileron have been reported Figure 185 at increasing morphed down deflections.



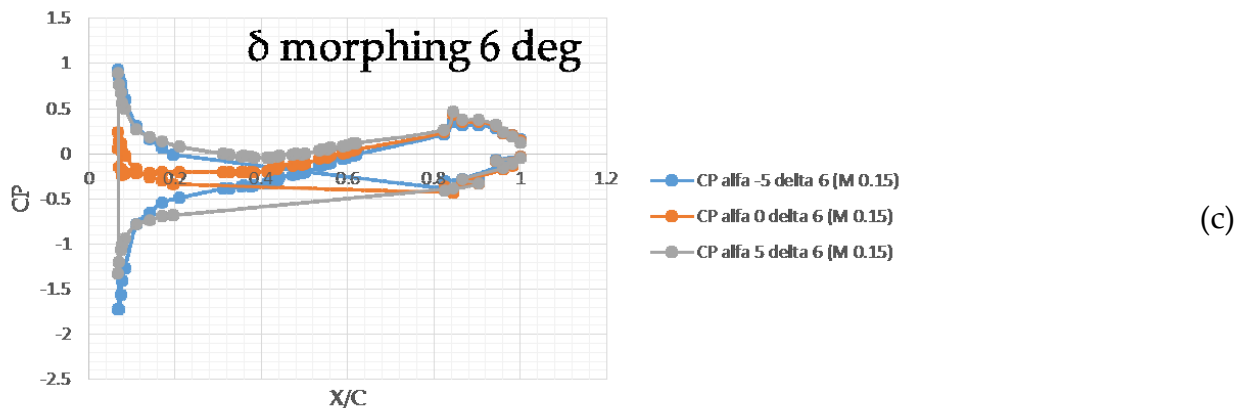


Figure 185 - Pressure distribution around the morphing wing at increasing AOA and aileron morphing angle (a), (b) and (c)

Also tests with smokers for streamline visualization have been carried out. The tests have been conducted at various aileron deflection and in dynamic regime with aileron morphing respectively at 0.5-1.5-3 Hz at low wind tunnel speed.

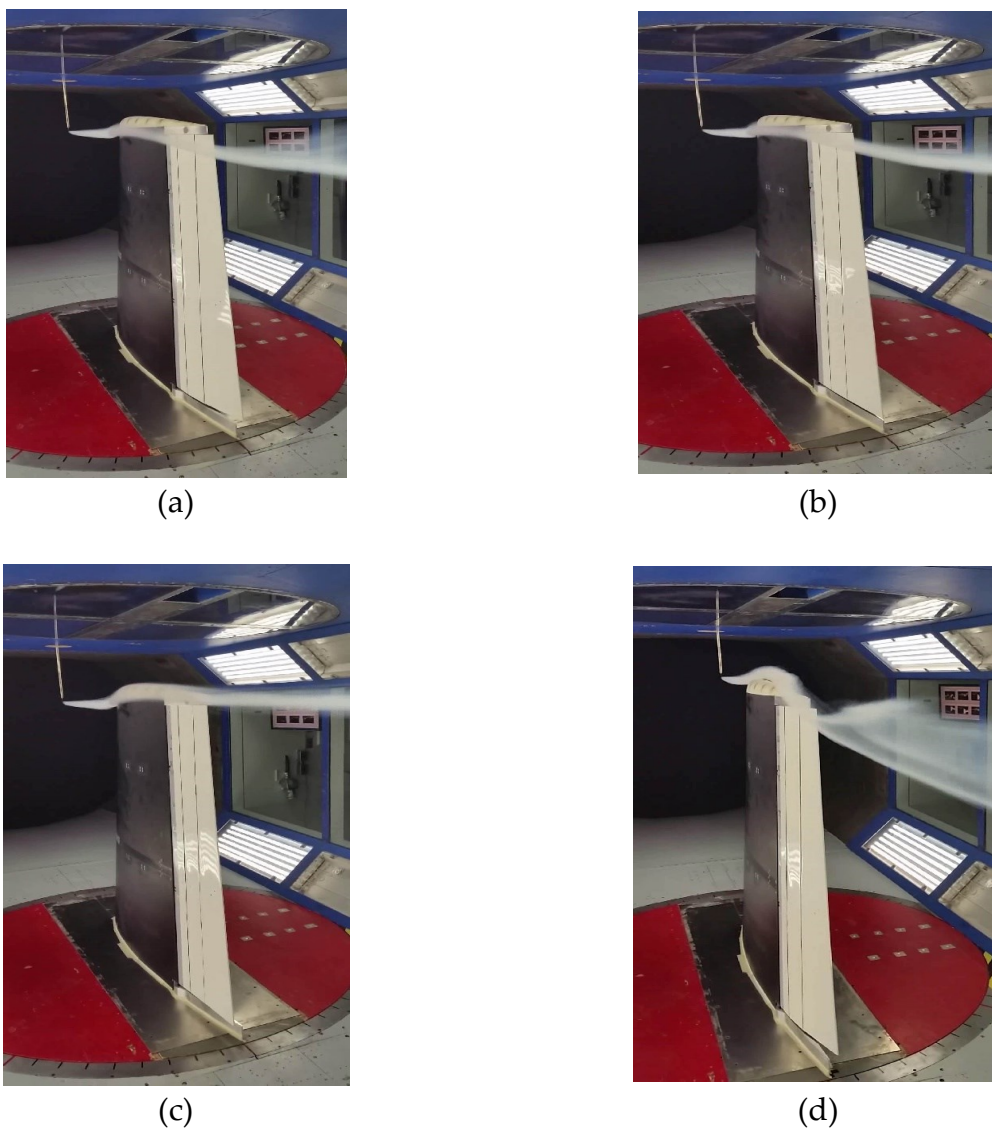


Figure 186 – Smoker tests with tip vortex in morphed down, baseline and morphed up

The preliminary results obtained during wind tunnel tests at Mach number equal to 0.15 are reported in the following aerodynamic curves for baseline configuration and respectively at morphed down (+3° and +6°):

- Lift versus angle of attack ($CL - \alpha$). Figure 187.
- Drag versus angle of attack ($CD - \alpha$). Figure 188.
- Drag polars ($CL - CD$). Figure 189.

The first one shows a typical linear trend. The curve slope (CL_α) remains unchanged and clearly by a morphing aileron deflection (from baseline to 6 deg), the camber increase (high α_{0L}) and the curve moves in parallel upwards. The blue curve is the baseline while orange is at 3° morphed down and the grey correspond to 6° morphed down.

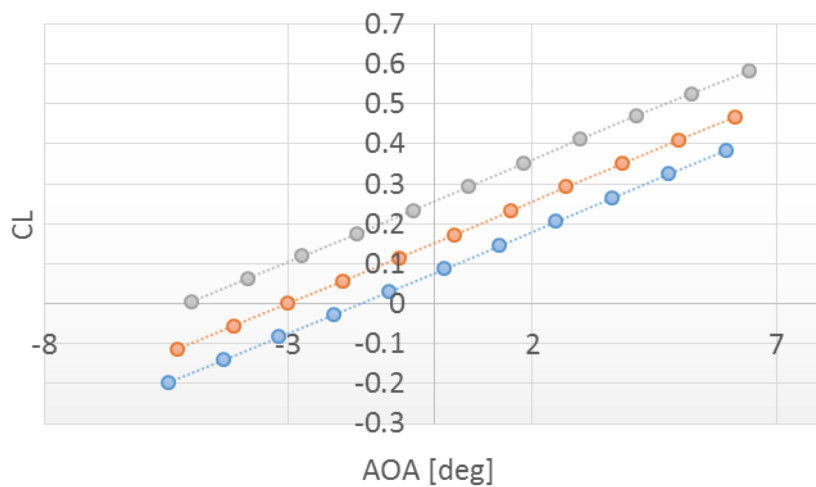


Figure 187 - Lift coefficient versus angle of attack curve

The $CD - \alpha$ curve trend is reported in Figure 188 for both un-morphed and morphed down. The tendency shows that the minimum drag coefficient shift on the left as the morphing deflection increase leading to high CD_0 .

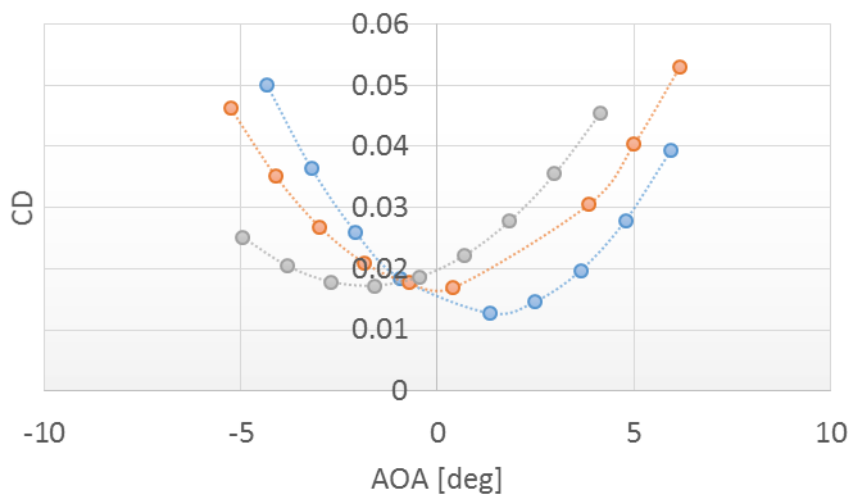


Figure 188 - Drag coefficient versus angle of attack curve

Finally, the drag polars are depicted in Figure 189. In this case, when a morphing deflection occur, the polar cross in correspondence of a pivot point for high CL while it moves on the right side of the Cartesian plane for low CL . This means that it is possible to identify an envelope curves which is the optimum one (dotted red line).

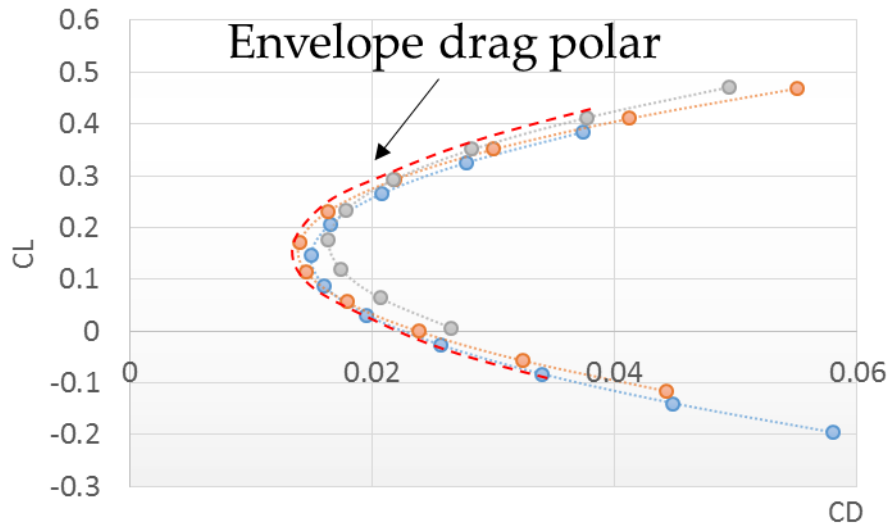


Figure 189 - Drag polars with the envelope curve

The herein presented aerodynamic curves represent a global trend and describe the behaviour of the morphing wing tested. It is noteworthy that, in order to effectively prove the benefit introduced by such technology, the impact of the adaptive aileron on a real aircraft must be assessed but the results show the great potential of the morphing aileron with the capability of adaptation to flight conditions, to enhance significantly the aerodynamic performance of an aircraft all along its mission.

6. Conclusions

A Self-contained morphing concept applied to a Safety Critical Hinged Control Surface was outlined in this thesis. In particular, an aileron was investigated as an extension of an adaptive trailing edge in order to improve of L/D ratio and at the same time to preserve the conventional aileron functionality. The resulting morphed geometry, called “morphing aileron” will assure an augmented functionality rather than traditional systems (rigid aileron). The device will be able to rigidly rotate around main hinge axis and in addition will enable camber morphing. This technology has not already extensively investigated in the literature because the aileron is a critical control surfaces whose failure is catastrophic for the aircraft. Moreover it is positioned in a very delicate zone from aeroelastic point of view with very reduced volume that allows a difficult and challenging integration of actuators and mechanism. The morphing aileron is an extension of the morphing trailing edge technology to the outboard wing region where small deflections could bring significant aerodynamic benefits. It has been designed for a symmetrical deflection during cruise in order to compensate A/C weight variation due to fuel burned. In such a manner, it is aimed to increase aerodynamic efficiency (reduce drag) in off design points. Other important research scenario opened by such morphing device go through load control and load alleviation. In detail, by deflecting a morphing aileron it is expected to redistribute the spanwise wing distribution in order to reduce wing root bending moment, on the other hand, by increasing actuator bandwidth it can be tailored to reduce peak stress from gust. Finally, the use of electromechanical actuator is coherent with a more electric approach aimed at substitute the conventional shafted actuation mechanism with a more distributed assessment made of more but lighter actuators.

The thesis begins with an introduction on the “biological inspiration” that driven aeronautical researcher and engineers worldwide in the field of morphing structures. It has been conducted an overview based on the main studies on the morphing structures, in particular focused on the most recent trailing edge technology with its problematic and design aspects. It has been described the main results obtained from the developed technologies of Clean Sky, Saristu and FlexSys. Subsequently, the attention was drawn to the real aircraft actuation system trend through years, following their evolution and showing that in recent time technology is approaching to an apparently more simple concept of a trailing edge. In fact, a morphing trailing/leading edge appears as a no gap, smooth and optimized control surface that can improve aircraft performance, but however the main technological challenge consist of how to move such device enabling large deformations and at the same time resist to heavy external loads. This well-known “morphing paradox” has been solved with both compliant and rigid body mechanism. Which is the ideal one is now already discussed because both methodologies exhibit pros

and cons. In the introduction is also described some of the main actuation systems for morphing devices based on SMA, PMA and kinematic mechanism.

The present thesis has been developed inside the framework of the CRIAQ MDO505 research project. It is a project composed of an international consortium of Canadian and Italian academies, research centre and leading industries with the aim to design and tests a prototype of a full scale wing tip equipped with two morphing devices for improve aircraft efficiency. The first device involve the bump of the upper wing box skin while the second one is the variable camber morphing aileron.

Subsequently all the design phases of the morphing aileron have been described. Starting from the aerodynamic shapes, the rib architecture with spanwise stiffening elements are presented. In order to deflect a “finger-like” rib architecture, a compact actuation system solution based on double-sided guides and a fork-shaped crank has been designed. Advanced finite element model in order to validate the structure at limit and ultimate loads have been carried out setting all the details necessary to produce a laboratory demonstrator. This one was assembled and tested, proving the effective functionality of the concept. Finally, wind tunnel tests assessing the aerodynamic trend of such innovative architectures have been reported. The idea herein described leads the way to further researches aimed at enhancing the TRL of the concept. To this aim, some remarks should be done on the most critical aspects of the current device. In particular, future steps may be:

- an embedded sensing network for enhanced control in order to assure the achievement of the target aero-shapes;
- actual shapes evaluation and comparison with expected aero-shapes;
- aerodynamic benefits comparison between rigid and morphing aileron;
- morphing Aileron-related (Wing and A/C) performance benefits estimations starting from the aerodynamic trend estimated with the experiment described in this work,
- enhanced Design with Topology optimization;
- segmented skin aerodynamics comparison with a tailored compliant skin technology;
- high speed simulations and tests.

References

- [1] John Valasek in *Morphing Aerospace vehicles and Structures*. A John Wiley & Sons, Ltd., Publication (2012)
- [2] W. Akl, S. Poh, A. Baz in *Wireless and distributed sensing of the shape of morphing structures*, Sensors and Actuators A: Physical - Journal – Elsevier, (2007)
- [3] <http://www.featheredphotography.com/blog/>
- [4] I. Dimino & AS02 Team in *Strutture Adattive*, presented at CIRA Symposium (2014)
- [5] I. Dimino, D. Flauto, G. Diodati, M. Schüller, A. Grati in *Adaptive Shape Control Architecture for Morphing Wings*. Proceedings of the 6th ECCOMAS Conference on Smart Structures and Materials. SMART2013, Torino, June 2013.
- [6] Bowman J, Weisshaar T and Sanders B 2002 in *Evaluating the impact of morphing technologies on aircraft performance*. In 43rd AIAA/ASME/ASCE/AHS/ASC structures, Structural Dynamics and Material Conference, number AIAA-2002-1631, Denver, CO, 22-25 April.
- [7] T.A. Weisshaar in *Morphing Aircraft Technology – New Shapes for Aircraft Design*. Meeting Proceedings RTO-MP-AVT-141, Overview 1. Neuilly-sur-Seine, France (2006).
- [8] H. Hilbig, H. Wagner in *Variable wing camber control for civil transport aircraft*, ICAS 84-5.2.1, pp. 107-112, Toulouse 1984.
- [9] H.P. Monner, D. Sachau, E. Breitbach in *Design Aspects of the Elastic Trailing Edge for an Adaptive Wing*, presented at RTO AVT Specialists' Meeting on "Structural Aspects of Flexible Aircraft Control", held in Ottawa, Canada, 18-20 October 1999, and published in RTO MP-36.
- [10] Bolonkin A., Gilyard GB., in *Estimated Benefits of Variable-Geometry Wing Camber Control for Transport Aircraft*, NASA Technical Report 1999
- [11] Szodruch J. in *The Influence of Camber variation on the Aerodynamics of Civil transport Aircraft*. Presented at AIAA 23rd Aerospace Sciences Meeting 1985 Reno, Nevada, US.
- [12] S. Kota, R. Osborn, G. Ervin, D. Maric, P. Flick, D. Paul in *Mission Adaptive Compliant Wing – Design, Fabrication and Flight Test*, Published as RTO-MP-AVT-168 (2006)
- [13] <http://ec.europa.eu>
- [14] www.cleansky.eu
- [15] Mingione, G., "Preliminary design of wing trailing edge morphing architectures," JTI-GRA deliverable no. GRA2.2.1-TN-CIRAPlus-TECH-210105A, (2001 research report).
- [16] R. Pecora, F. Amoroso, G. Amendola and A. Concilio in *Validation of a smart structural concept for wing-flap camber morphing*, Smart Structures and Systems, Vol. 14, No. 4 (2014) 659-678
- [17] www.saristu.eu/

- [18] Wölcken, P.C., Papadopoulos, M., *“Smart Intelligent Aircraft Structures (SARISTU)”*, Proceedings of the Final Project Conference, Springer 2015 ISBN 978-3-319-22413-8
- [19] Dimino, I., Flauto, D., Diodati, G., Concilio, A., Pecora, R., *“Actuation System Design for a Morphing Wing Trailing Edge,”* Recent Patents on Mechanical Engineering, Volume 7, pp 138-148, (2014).
- [20] US Patents: 5971328, 6491262, 7384016 B1
- [21] European Patents: 1047593, 1603798, DE 69934210T2
- [22] www.flxsys.com. Technology Fact Sheets
- [23] D. Reckzeh in *Flying Community Friendly – The Role of High Lift Aerodynamics*. Presented at KATnet II conference, Bremen, 2009
- [24] U. Dreßler, Start- und Landekonfigurationen, DaimlerChrysler Aerospace, März 1999
- [25] Rudolph, P., K., C., *“High-Lift System on Commercial subsonic Airlines,”* NASA Report 4746, September 1996
- [26] Strüber, H., *“The Aerodynamic Design of the A350 XWB-900 High Lift System,”* proceeding of ICAS 2014, St. Petersburg, Russia, 7-12 September 2014.
- [27] J.C.Derrien in *Electromechanical Actuator (EMA) Advanced Technologies for Flight Controls*, presented at 28th International Congress of the Aeronautical Sciences (ICAS 2012)
- [28] Concilio, A., *“SARISTU-booklet of technologies,”* (2014)
- [29] Kudva, J., N., Lockjer, A., J., Appa, K., *“Adaptive Aircraft Wing,”* AGARD SMP Lecture Series 205, Smart Structures and Materials: Implication for Military Aircraft of New Generation (1996).
- [30] Kudva, J., N., Jardine, P., Martin, C., Appa, K., *“Overview of the ARPA/WL “Smart Structures and Material development – Smart Wing Contract,”* SPIE 1996 vol. 2721.
- [31] Kudva, J., N., Carpenter, B., *“Smart Wing Program,”* DARPA Technology Interchange Meeting, June 2000.
- [32] Barbarino, S., Pecora, R., Lecce, L., Concilio, A., Ameduri, S., and De Rosa, L., *“Airfoil Structural Morphing based on S.M.A. Actuator series: Numerical and Experimental Studies,”* Journal of intelligent material system and structures. Vol 0, 2011
- [33] Wereley, N., M., Kothera, C., Bubert, E., Woods, B., Gentry, M., Vocke, R., *“Pneumatic Artificial Muscles for aerospace applications,”* 50th AIAA/ASME/ASCE/AHS/ASC Structures, Structural Dynamics, and Materials Conference, 4 - 7 May 2009, Palm Springs, California
- [34] Bowman, J., Sanders, B., Cannon, B., Kudva, J., N., and Joshi, S., Weisshaar, T., *“Development of Next Generation Morphing Aircraft Structures,”* 48th AIAA/ASME/ASCE/AHS/ASC Structures, Structural Dynamics and Material Conference, 23-26 April 2007, Honolulu, Hawaii.
- [35] Flanagan, J., S., Strutzenberg, R., C., Myers, R., B., and Rodrian, J., E., *“Development and Flight Testing of a Morphing Aircraft, the NextGen MFX-1,”* 48th

- AIAA/ASME/ASCE/AHS/ASC Structures, Structural Dynamics and Material Conference, 23-26 April 2007, Honolulu, Hawaii
- [36] Kudva, Martin, Scherer, Jardine, McGowan, Lake, Sendekji, Sanders in *Overview of the DARPA/AFRL/NASA Smart Wing Program*. SPIE Proceedings, Vol. 3674, 230 (1999)
- [37] Di Matteo, N., Guo, S., and Li, D., "Morphing Trailing Edge Flap for High Lift Wing," 52nd AIAA/ASME/ASCE/AHS/ASC Structures, Structural Dynamics and Material Conference, 4-7 April 2008, Denver, Colorado.
- [38] www.nasa.gov
- [39] Barbarino S., Bilgen O., Ajaj RM., Friswell MI. and Inman DJ., "A Review of Morphing Aircraft," *Journal of Intelligent Material System and Structures*, Vol. 22 June 2011
- [40] Grigorie, T., L., Botez, R., M., Popov, A., V., "Fuzzy Logic Control of a Smart Actuation System in a Morphing Wing," Chapter of the book "Fuzzy Controllers-Recent Advances in Theory and Applications" edited by Sohail Iqbal, Nora Boumella and Juan Carlos Figueroa Garcia, ISBN 978-953-51-0759-0, InTech, September 9, 2012
- [41] Kammegne, M., J., T., Botez, M., R., Mamou, M., Mebarki, Y., Koreanschi, A., Gabor, O., S., Grigorie, T., L., "Experimental wind tunnel testing of a new multidisciplinary morphing wing model" proceedings of the 18th international conference on mathematical methods, computational techniques and intelligent systems (MAMECTIS 2016)
- [42] Reuleaux, F., in *The Kinematics of Machinery: outlines of a Theory of Machines*. Translated and edited by Alex B.W. Kennedy, C.E. Macmillan and co., 1876.
- [43] E.F. Bruhn Analysis and design of flight vehicle structures, Tri State Offset Company, 1973
- [44] <http://www.ikont.eu>
- [45] Rea, F., in *Aeroelastic Stability Analysis of a Wind Tunnel Test Article equipped with a true scale Morphing Aileron*. Master Thesis at University of Naples Federico II (2014)
- [46] CRIAQ Technical Report CRQ-TD003-0-072015 – *Morphing Aileron Device: Flutter Clearance Demonstration* (2015)
- [47] E. G. Broadbent in *Flutter and response calculation in practice*. AGARD Manual on Aeroelasticity, Vol 3, NASA, Feb 1963, Chap.4
- [48] Dimino, I., Diodati, G., Concilio, A., Volovick, A., Zivan, L., in *Distributed Electromechanical Actuation System Design for a Morphing Trailing Edge Wing*, SPIE Smart Structures/NDE, Las Vegas, Nevada (USA) March 2016.
- [49] Dimino, I., Amendola, G., Pecora, R., Concilio, A., Chapter *Experimental Verifications* of the Book *Morphing Wing Technologies for Large Commercial Aircraft*, Editors: A. Concilio, I. Dimino, L. Lecce, R. Pecora

Acknowledgments

The author acknowledges ETS (L'École de Technologie Supérieure), NRC (Canadian National Research Council), Bombardier Aerospace, Thales Aerospace and Alenia Aermacchi for their technical support as partners of the CRIAQ MDO-505 project. Special acknowledgements go to Prof. Ruxandra Botez (ETS), which is the Coordinator of CRIAQ MDO-505 project, for having defined goals and purposes for the research of this work. The most heartfelt thanks goes to Professor Leonardo Lecce, for having maintained important collaboration contact which lead to this challenging activity that gives me the opportunity to grow professionally and also for his willingness and precious advices stimulating my passion for aeronautics. Warm thanks goes also to Professor Rosario Pecora and Professor Francesco Amoroso and to my CIRA tutor Eng. Ignazio Dimino for their guidance and constant support that become, during these three years, more than a collaboration grown on the basis of mutual esteem that has allowed me to work in a very exciting and excellent team. Furthermore I'd like to thanks the CIRA scpa institution (Italian Aerospace Research Centre), that constitute a reference point in the aeronautic scenario for young researcher in Italy and also worldwide, for its openness and availability to always invest and support researcher during their training period.